Atoms, photons, and Information

by

Andrew Silberfarb

B.S. California Institute of Technology, 1998

DISSERTATION

Submitted in Partial Fulfillment of the
Requirements for the Degree of

Doctor of Philosophy
Physics

The University of New Mexico

Albuquerque, New Mexico

March, 2006

Dedication

To my Grandmother, Besi Silberfarb, for her support, and constant encouragement.

, and to my parents for their understanding

Acknowledgments

I am deeply indebted to my advisor, Professor Ivan Deutsch, for his support, camaraderie, and good sense of humor. I thank Poul Jessen's entire group at the University of Arizona, and specifically Greg Smith, for his perseverance with a very difficult experiment. Finally I acknowledge Andrew Landahl for help with some semi-definite programming.

Atoms, photons, and Information

by

Andrew Silberfarb

ABSTRACT OF DISSERTATION

Submitted in Partial Fulfillment of the
Requirements for the Degree of

Doctor of Philosophy
Physics

The University of New Mexico

Albuquerque, New Mexico

March, 2006

Atoms, photons, and Information

by

Andrew Silberfarb

B.S. California Institute of Technology, 1998

PhD. Physics, University of New Mexico, 2006

Abstract

Lasers are an essential tool for the manipulation of atomic systems in modern physics labs. These lasers, however, do not only act as classical controls, but are full quantum objects in themselves. The interaction between a laser, or any state of the light field for that matter, and an atom will transfer information from the atom to the laser. This information transfer can act to decohere the state of the atom, or can require conditioning of the atomic state if the information is measured.

This dissertation explores the interaction of a laser with an ensemble of atoms. We examine the fundamental atom-field interaction which is responsible for transferring information from atom to laser. We derive the atomic dynamics generated by the lasers interaction with the atom and explore the consequences of these dynamics. Finally we explore the information carried away from the atom by the laser and discover how this information can be used to determine the initial state of an identically prepared ensemble of atoms.

The results of this dissertation span a broad range answering questions about the basic nature of the atom photon interaction, to an in depth examination of quantum

state reconstruction using continuous measurements as applied to atoms probed by a laser. The most fundamental result derived is that a laser control pulse decoheres an atomic system it interacts with at the same rate as spontaneous emission into the modes occupied by the laser pulse. Thus use of laser controls to manipulate atoms does not increase the rate of decoherence experienced by the atom beyond that already present in the uncoupled system. In a similar vein we prove that a single photon traveling wave pulse cannot ever excite an atom with unit probability due to decoherence, and calculate the maximum probability of excitation for the atomic system driven by such a pulse.

Entanglement can be used as a resource in many quantum information protocols, including quantum computation, quantum cryptography, and quantum teleportation. We quantify the entanglement between a laser and an atom in free space, finding that it is always small and can be predicted remarkably well using a closed system model. The results of this calculation act as a benchmark against which one can measure the entanglement generated in other procedures.

We demonstrate that control of the full spin state corresponding to a single hyperfine ground state manifold of an alkali atom can be achieved using magnetic fields and an off resonant ac-Stark shift. Such control requires that the hyperfine structure of the excited state is resolved, so that the light shift generates the required nonlinear spin moment. Control of a spin provides an essential tool for exploring both basic physics and for allowing implementations of various quantum protocols. We use the control to facilitate performance of quantum state tomography using a continuous laser probe. This requires detailed simulations of the atomic dynamics and the continuous measurement. The mathematics needed for such simulations are rederived in this dissertation, and the techniques used to perform the simulations as well as to perform the rest of the reconstruction procedure are presented. The first experimental example of continuous measurement quantum state reconstruction is

then presented.

Contents

List of Figures

List of Figures

Chapter 1

Introduction

Over the past twenty years the possibility of exploring deeply quantum regimes using tabletop experiments has become a reality. Over the last ten, sufficient control of such experiments has joined the distinct disciplines of quantum physics, information theory, and control theory into a unified whole. This dissertation explores the confluence of these fields by examining the interaction of the electromagnetic field with an atom using tools from all three. Specifically, we explore the how information is transported away from an atom by a traveling mode of the electromagnetic field (light), and how this information can subsequently be extracted and employed to estimate the initial atomic state.

This work ties in to a vast array of past and future research, both experimental and theoretical. The foundational work in quantum optics by Glauber, Cohen-Tanoudji and others [82, 83, 17] provides the basis for this dissertation. Quantum information theory provides many of the tools necessary to proceed with this work including the work on entanglement quantification [51], quantum state tomography [1] and quantum trajectories [13]. Finally control theory presents methods for solving difficult problems using techniques such as semi-definite programming [88], as well

as techniques useful in optimizing information extraction [40].

The basic system of an atom interacting with a light field is ubiquitous, appearing repeatedly in many modern experiments. Most directly related to this dissertation are the experiments on macroscopic entanglement between ensembles of atoms [38], and spin-squeezing using quantum measurement [44, 33] allowing for more accurate magentometry [34], or its generalization to pseudo-spin squeezing which can enhance the accuracy of atomic clocks [79]. Other systems whose analysis can benefit directly from a deeper understanding of atom-light interactions include cavity QED systems [8], optical latices [21], ion trap quantum computers [71], and quantum cryptography [67]. Additionally, much of the theory of continuous measurement tomography built up in Chap. 5 is generally applicable to any quantum system. It is likely that the techniques explored in these later chapters will find a use in some of the already mentioned systems, as well as in solid state systems using quantum dots [77] or superconductors with Josephson junctions [53]. Nanoscale devices, such as cantilevers can now me manufactured on a quantum scale [66, 60], creating another system in which the techniques discussed in this dissertation can be fruitfully applied.

1.1 Quantum measurement

Quantum measurement and specifically quantum continuous measurement forms the heart of this work. Quantum measurements allow us to extract information about a quantum system through its interactions with the outside world. A coherent theory of quantum measurement has been built up from the basics expounded by von Neuman and others [91] to today include a vast array of techniques for extracting information from a quantum system, and theoretical methods for describing them.

Strong projective measurements which completely collapse a quantum state are the most theoretically straightforward to discuss. Such measurements have formed

the basis for many of the experiments in 20th century physics. An example of such a measurement is the Stern-Gerlach measurement which projects the state of a quantum spin into one of its possible eigenstates. These measurements completely collapse the quantum state of the system resulting in an eigenstate of the measurement operator. Such back action of the measurements on the quantum state of the system is a ubiquitous feature of quantum measurement, separating it from its classical counterparts.

More recently, consideration has been given to weaker measurements that do not completely collapse the quantum states. These can be theoretically described through the formalism of positive operator valued measures (POVMs)[51]. These can be implemented by performing a strong measurement on a system coupled to the system of interest. Much theoretical work has been done on such measurements including possible implementation of such measurements [5], the uses of such measurements in quantum state estimation [18], and their role in solving problems on a quantum computer [6].

More commonly in a laboratory, one finds weak measurements in the form of continuous measurements rather than in the single shot POVM approach. Of course the two can be shown to be equivalent in an abstract sense. Consideration of weak continuous measurement has led to many interesting theoretical developments. Included among these are stochastic Schrödinger equations and stochastic master equations describing the dynamics of a continuously measured system[28] and quantum trajectories employing the techniques of continuous measurement to unravel the decoherence processes in a system in terms of possible measurements on the environment [13]. The theory of quantum trajectories has resulted in techniques for integrating quantum master equation in open systems with significantly reduced overhead, either using montecarlo methods, or other techniques one of which is discussed in Chap. 3. Experiments employing quantum continuous measurements now abound, ranging

from the continuous measurement of atomic ensembles [68], and cavity QED systems [92], to nanoscale cantilevers [60], and solid state devices using single electron transistors [46].

Consideration of continuous measurement has also brought discussion of quantum systems and classical systems closer together. Control theory has developed many tools to discuss the measurement of classical systems[40]. Specifically one can ask questions about measurability of a classical system in the presence of noise, and discuss optimal methods for extracting information through filtering. The powerful tool of filtering can be brought to a quantum setting by introducing quantum filters as done by Belavkin [7]. Quantum filtering can then be used to update the state of knowledge about a quantum system. One can then extend the powerful tools of classical control theory into the quantum regime [11]. The main distinction between quantum and classical measurement in this setting is seen to be a link between the noise terms in the filter and the measurements made. Recently an experiment using a quantum Kalman filter to estimate a magnetic fields using a quantum ensemble of atoms whose state becomes quantum correlated due to measurement backaction was performed [34]. The continuous measurement was essential to this procedure and we can look forward to many more such fusions of classical control and quantum systems in the future.

This dissertation considers the theoretical implications of using a laser probed to continuously measure an atomic ensemble in free space. This measurement results in decoherence and backaction. When the measurement strength is strong compared to the natural decoherence of the system, one can observe strong backaction producing spin squeezed states with variance smaller than any possible separable state [33, 44]. Alternatively one may produce entanglement between two macroscopic atomic ensembles [38] by performing measurements of lasers which have interacted with both systems; the backaction of these measurements resulting in quantum correlations be-

tween the ensembles. Here we consider the opposite extreme of measurements weak compared to the decoherence such that one cannot observe strong quantum correlations due to backaction. We examine the quantum effects of such measurements and how these measurements can be used to update knowledge about the system state.

1.2 Quantum control

Control of quantum systems is a burgeoning field, intimately connected to quantum computation and quantum metrology. Control comes in two main varieties. Open loop control explores the optimal way to achieve specific system goal, such as generating a specific state or performing a given measurement based upon prior knowledge of the system. Closed loop control considers the same problem except the prior information is augmented by information obtained from the system during the evolution process. This information would usually be obtained by a continuous measurement of the evolving system, though other possibilities are conceivable.

Control theory allows one to optimize over the available controls as a function of time to achieve some desired goal, expressed in the form of a cost function on the state of the system. For Hamiltonian control, one has a Hamiltonian dynamics parameterized by several functions of time

$$H(t) = \sum_i u_i(t) H_i. \tag{1.1}$$

For a specific set of controls and an initial condition $|\psi(0)\rangle$, one attempts to minimize the cost function $\mathcal{C}(u_i(t), \psi(t))$ which can generally depend upon the full state and control trajectories.

Control has been considered in many contexts. The entire field of quantum chemistry is an exercise in quantum control as one attempts to generate a specific

transformation, chemical reaction, by subjecting an atom or atoms to a time dependent laser pulse which acts as a catalyst for the reaction [57]. One wishes to find the control field that generates the maximum fidelity of the result with the desired state $|\phi\rangle$ giving the simple cost $C = \langle\phi|\psi(T)\rangle$. More generally, open loop unitary control attempts to design $u_i(t)$ such that a particular unitary evolution is achieved. This is a more difficult problem for the same size system, given that it is a more exact target, but it is essential for gate implementation in quantum computing protocols, particularly those involving qudits, i.e.. based upon physical systems with more than two levels.

The use of real time feedback control in quantum systems is currently being explored experimentally. Real time feedback to stabilize the state of a cavity QED system has been experimentally demonstrated in [92]. Real time feedback used for magnetometry has been exhibited in [34]. Furthermore there are several current proposals for using real time feedback to improve signal discrimination [31], to perform error correction [4], and to perform nondestructive measurement of Fock states of the electro magnetic field [32].

This dissertation makes heavy use of open loop control theory to discuss and analyze problems that arise in the context of atoms interacting with lasers. The quantum state estimation procedure presented in Chap. 5 cannot currently be run in real time but, with some modification, could conceivably allow real time state estimation. One could then consider employing a full state based feedback procedure to control, as well as measure, the individual atomic state of an ensemble member.

1.3 Quantum state reconstruction

As quantum mechanical systems proliferate in laboratory settings, finding new applications in information processing tasks such as cryptography and computation

[51], quantum state reconstruction becomes an essential tool. Full quantum state reconstruction allows one to make contact between the abstract theory of quantum mechanics dealing with wave functions and density operators, representing states of knowledge, and physical experimental results. The goal of quantum state reconstruction, also known as quantum state tomography, is to determine the initial state of a system from an set of measurement results.

The basic procedure for state reconstruction begins with an ensemble of quantum systems all prepared in the same initial state $\rho(0) = \rho_0$. A set of measurements is then performed on these states. Each measurement (labeled by i) can be represented by a set of Hermitian operators (POVM elements) $\{E_{ij}\}$ which sum to the identity $\sum_j E_{ij} = I \ \forall i$. The probabilities for each outcome are

$$p_{ij} = \mathrm{Tr}\left[E_{ij}\rho_0\right]. \tag{1.2}$$

Performing each of the possible measurements multiple times on identically prepared states one can calculate the frequencies associated with each measurement result f_{ij}. Assuming that the number of repetitions is large enough the frequencies should approximate the probabilities $f_{ij} \approx p_{ij}$. Then assuming that the map (Eq. 1.2) is invertible one can estimate the initial state.

Since state reconstruction is such a fundamental primitive it has a long history with much theoretical and experimental exploration. The original theory of quantum state reconstruction was worked out by Pauli in [54]. Subsequently theoretical work on state estimation has included finding sets of informationally complete observables whose frequencies uniquely determine a state [**?**], finding transformations useful for inverting measurement results in continuous variable systems [**?**], and explorations of the use of entanglement in quantum state tomography [**?**]. I have also done some work in this area on informationally completeness in pure state reconstruction which is not reported in this dissertation [**?**]. Quantum state tomography is intimately connected to quantum process tomography which has received much theoretical and

experimental attention recently [**?**].

Laboratory demonstrations of state reconstruction are numerous and span a broad range of physical systems. These include continuous variable systems such as reconstruction of light fields [26], as well as discrete systems such as reconstruction of molecules [25], ions [70], atoms [42], spins [16, 41], and entangled photon pairs [65].

Quantum state reconstruction is usually performed using strong projective measurements such that $E_{ij}E_{ik} = E_{ij}\delta_{jk}$. Such strong measurements destroy the fragile quantum systems on which they act. Additionally they often extract more information about the state of the system then is necessary. This thesis explores the theoretical possibilities for quantum state reconstruction based on weak continuous measurements in Chap. 5. These techniques were then exhibited in a laboratory setting by our collaborators at Tucson, the results of these experiments are presented at the end of Chap. 5.

1.4 Experiment

While the theory presented in this paper has connections to a vast array of experimental situations as discussed in the previous sections it is specifically based around an example system. This system is experimentally realized by our experimental collaborators in Poul Jessen's group from the Optical Sciences Center at the University of Arizona, Tucson. The system consists of an ensemble of cesium atoms probed by an off resonant laser. The details of this system become essential in the later parts of this dissertation, particularly in Chap. 4 where we match experimental data with simulations, and in Chap. 5 where we use detailed knowledge of system dynamics to reconstruct quantum states. A thorough description of the experimental system can be found in [63], or Greg Smith's thesis [2]. Here we summarize the salient points.

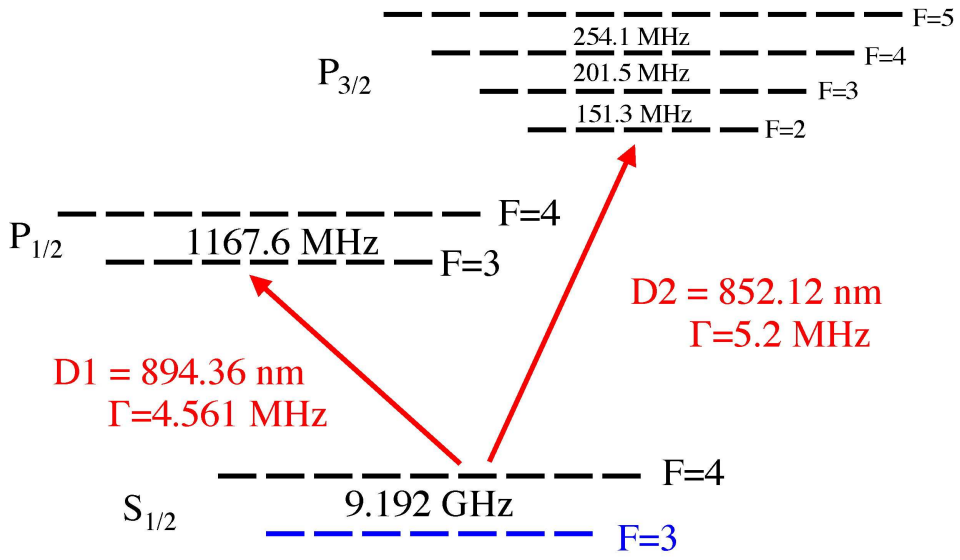

Figure 1.1: . Depicted is the level structure of ^{133}Cs including the ground state $S_{1/2}$ and excited state $P_{1/2,3/2}$ hyperfine splittings. Also noted are the laser frequencies and linewidths of the two possible $S \rightarrow P$ transitions. Most of the work in this thesis concentrates on the dynamics of a single ground state manifold corresponding to a single total spin, such as the $S_{1/2}$ manifold highlighted in blue with total angular momentum $F = 3$.

The heart of the experiment is an ensemble of cesium atoms which is trapped and cooled using a magneto-optic trap [**?**]. These ultracold ^{133}Cs atoms form a cloud of approximate density $10^{10} cm^{-3}$ and can be initially prepared using optical pumping [**?**] into one of several states. The level structure of the atoms is depicted in Fig. 1.1. The ground state has $S_{1/2}$ character, having zero orbital angular momentum, and $s = 1/2$ spin angular momentum to give total angular momentum of $J = 1/2$, as is true for all alkali atoms. The $S_{1/2}$ ground state is further split due to hyperfine interaction with the $I = 7/2$ nucleus, to give two ground state manifolds with total angular momentum $F = 3, 4$. In this dissertation we restrict consideration to the dynamics of a single ground state manifold having definite total angular momentum. Then the ensemble of atoms can be treated as an ensemble of spin F particles.

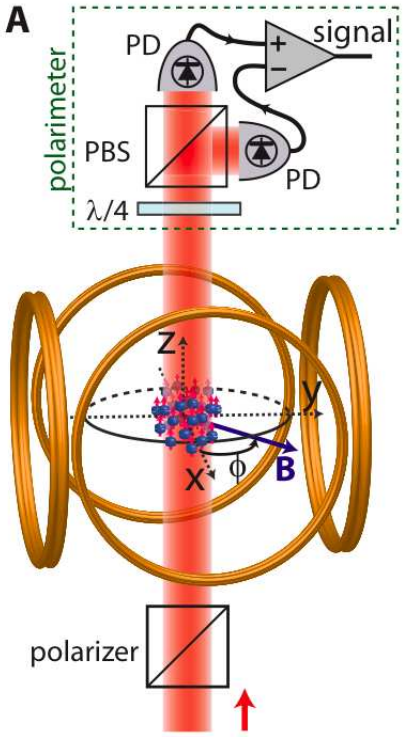

Figure 1.2: . Depicted is the cloud of ^{133}Cs atoms prepared in a magneto optical trap with density 10^{10}cm^{-3}, which is probed by an off resonant laser on an $S \rightarrow P$ transition. The laser is then analyzed by a polarimeter as depicted.[3]

The atoms in the ensemble are probed by a polarized laser, and can be subject to arbitrary magnetic fields as shown in Fig. 1.2. The probe laser can be tuned near to the $S_{1/2} \rightarrow P_{1/2}$ D1 transition or near to the $S_{1/2} \rightarrow P_{3/2}$ D2 transition. Both of these transitions are shown in Fig. 1.1 along with their associated widths and the hyperfine splitting of their respective excited states. The laser probe acts to induce nontrivial dynamics on the ground state manifold of interest through the ac-Stark shift. A detailed examination of the resulting atomic behavior is undertaken in Chap. 4.

In addition to driving dynamics of our ensemble of spins the laser acts to measure

the spins. Specifically after the polarized laser has passed through the sample its output polarization is measured as depicted in Fig. 1.2. This measurement provides information about some moments of the spin. The specific information that can be extracted is derived in Chap. 4, and Chap. 5 discusses how this information can be used to reconstruct the initial state of an identically prepared ensemble.

1.5 Related work

I have worked on several other projects related to the work presented in this dissertation that are not included in this manuscript.

Pseudopotentials can be used to replace true atomic interactions and produce the same long range behavior. The benefit of this replacement is that the pseudopotential has substantially fewer parameters than the original potenitial, and can be integrated much more easily due to its simple form. Rene Stock, Eric Bolda, and Ivan Deutsch and I worked upon correcting a long standing mistake in the original derivation of a delta function pseudopotential for higher partial wave scattering with the use of delta shells. More details of this work can be found in [**?**]. This work was extended by Iris Riechenbach, Ivan Deutsch Rene Stock and myself to examine how to use a delta shell pseudopotential to emulate the interaction two separated neutral atoms in an optical lattice. This work can be found in [**?**].

PSI complete POVM's are single measurements whose statistics can be used to completely characterize a pure quantum state. Steve Flamia, Carl Caves and I proved that for dimension d the minimal number of elements for such a POVM is $d-2$. For more details about this work please see [**?**].

Quantum control plays an important role in Chap. 5 of this thesis, allowing reconstruction of an initial quantum state. The same techniques can be applied to

create arbitrary initial states of the quantum system, and I am currently involved in a project with Seth Merkel, Souma Chaudhury, Greg Smith, Ivan Deutsch and Poul Jessen to realize just such quantum state control.

1.6 Layout of this dissertation

The degree to which this dissertation is tied to a particular experiment presents a challenge. Most of the work done can be explained in terms of the very specific details of the experiments performed at the university of Arizona, however, this removes much of its inherent generality, as well as burdening the basic concepts with unnecessary detail. Therefore considerations specific to the system at hand are put off until necessary or useful. Keeping this in mind the layout of the subsequent chapters is as follows.

Chap. 2 explores the amount of decoherence an atom experiences due to the presence of traveling wave probe field. This question was brought to light by several recent papers [**?**], whose authors disagreed on the answer. A brief discussion of this controversy along with the analytic analysis of the problem is presented. A simple two level approximation for the atomic system is used throughout.

Chap. 3 bounds the entanglement generated between a finite duration laser pulse and an atom in free space. The entanglement is always small as expected and in fact agrees unexpectedly well with a much simpler method of calculation. This agreement is explained in terms of differential coupling strengths. Again only a two level description of the atom is needed.

Chap. 4 presents a detailed examination of the coherent and incoherent dynamics of an alkali atom interacting with a laser probe. The probe is treated classically, while the full atomic hyperfine structure is accounted for. A review of standard

adiabatic elimination is presented, a tensor decomposition of the atomic dynamics is worked out, and a novel method for adiabatically eliminating a repumper is discussed. Throughout particular attention is paid to transfer of coherence during spontaneous emission. Finally simulations using the above derived dynamics are compared to Larmor precession data.

Chap. 5 considers an ensemble of atoms all prepared in the same initial state which interact with a laser probe. We derive a method to extract information about the initial state of the system from such a measurement. The techniques used can be applied quite generally, however, it is useful to consider a concrete system for clarity, so a fully general treatment is not given. We then present experimental data obtained by our collaborators at the University of Arizona exemplifying the use of these techniques.

The final Chap. 6 briefly summarizes the results from this dissertation. The possibilities for extension of this work are then discussed,

The appendices provide a hard copy record of the code used to perform calculations and simulations for this dissertation. Specifically Appendix A contains the code used for the entanglement calculations of Chap. 3 while appendix B contains the simulation and reconstruction code used in Chap. 4 and Chap. 5. Appendix C presents a general derivation of the tensor decomposition of the atom field interaction for alkali atoms, which has been graciously provided by Prof. Ivan Deutsch.

Chapter 2

Atomic decoherence due to light

Current research to create quantum information processors has forced a reexamination of the underlying description of these devices. In order for us to gain information about quantum systems they must be measured. In the standard picture strong projective measurements perform this task; in laboratories it is more common to have a continuous probe which interacts with the system of interest and is then detected as a macroscopic signal. Examples include the probing of a quantum dot with a single electron transistor (SET) [22] and the measurement of the position of a micromechanical cantilever by monitoring the modulation of a reflected laser beam [47]. The formalism of quantum mechanics provides a number of different approaches for analyzing such situations. Scattering theory employs Green's function input-output relations to describe the evolution of the probe asymptotically, both before and after its interaction with the system under examination. Alternatively, the theory of quantum trajectories [13] provides a dynamical description of the quantum system being measured, conditioned on the continuous information being collected via the probe. As laboratory developments give us access to the control and manipulation of quantum systems these descriptions become ever more relevant. The quantum trajectory approach has the advantage of directly tying the dynamics of the system's evolution

to the measurement record. The ability to do this is essential when implementing adaptive measurement and control strategies employing feedback [93, 23, 92, 50, 75].

The key parameter we use to characterize the dynamics of a continuously observed system is the measurement strength(κ). It determines the rate at which information is coupled from the system to the probe. If the probe is discarded then this is the rate at which the system loses information or decoheres. If the probe is measured κ sets the scale at which effects such as quantum back-action become significant. For example, Bhattacharya et al. [9] have shown that for sufficiently macroscopic systems there is a window of values for κ such that continuous observation can localize the probability distribution to a quantum trajectory that faithfully tracks the classically predicted trajectory, with minimal quantum noise. Another example is the continuous measurement of ensembles of atoms, controlled through their collective interaction with a common probe, to produce nonclassical spin squeezed states [44, 38]. These effects depend crucially on κ and its relation to the other rates governing the system dynamics.

The standard paradigm for continuous measurement is cavity QED. The dynamics of a cavity mode of the electromagnetic field are monitored by a partially transmitting mirror [45, 73]. Input-output scattering theory, suited specifically to the language of optical elements [27], is used to connect the intracavity dynamics with those of the traveling signal. In order to translate the typically discrete information of the individually transmitted photons into continuous information one considers a homodyne or heterodyne measurement, in which the signal is mixed with a macroscopic local oscillator. The result is a stochastic Schrödinger equation which describes both the localization of the quantum state conditioned on the measurement and also the effect of quantum "back-action noise" [28].

This dissertation considers light fields outside of a cavity, which presents several complications beyond those encountered in the cavity QED setting. There is no

inherent method to select out privileged modes of the electromagnetic field which preferentially interact with the atom. Additionally there is no predefined mode volume of the interacting modes, which volume is necessary to calculate the interaction strength. One way to get around this problem was demonstrated when Milburn *et al.* [47] modeled continuous observation of a moving cantilever monitored by the modulation of a reflected laser beam. They considered the cantilever to be a mirror, which, partnered with an imagined partially transmitting surface, formed a leaky optical cavity. Under the assumption that the transmission rate of light through the fictitious mirror is much faster than the characteristic rate at which the cantilever moves, the cavity could be adiabatically eliminated from the dynamics. This led to a stochastic Schrödinger equation for the continuously observed cantilever alone. The unphysical quantization volume, however, still appeared implicitly in this equation which should not have happened.

In the following we formulate the problem of continuous measurement by a traveling wave probe. We derive a master equation describing the situation in which the system is monitored by the probe, but the measurement result is not recorded. This allows us to to identify the important characteristic scales of the problem without reference to a particular measurement scheme. We begin in Sec. 2.1 by establishing the necessary formalism for treating propagating fields in quantum optics, in contrast to the more familiar closed cavity problems. We apply this formalism in Sec. 2.2 to a two-level atom interacting with a resonant laser field. When the field is treated classically this leads to Rabi flopping, but when treated quantum mechanically the laser not only manipulates the atom but also acts to continuously measure it. The amount and nature of the decoherence induced by this measurement has been the subject of much recent controversy [**?**]. We determine the rate at which the measurement back-action leads to decoherence in the atomic system, and discuss the resolution of some apparent paradoxes. We then contrast these results to the atomic evolution when coupled to a resonant electromagnetic pulse with a fixed photon number n.

In particular, we explore the circumstances under which we can recover the usual Jaynes-Cummings solution for a two-level atom coupled to a single mode [62] and show how the behavior for a single photon diverges from this solution. In Sec. 2.3 we consider continuous measurement of an atomic spin through the Faraday rotation of an off-resonant laser field. This process has been used to generate spin-squeezed states in atomic ensembles [44, 38, 33], and plays an important role in the later chapters of this dissertation. We conclude and summarize our results in Sec. 2.4.

2.1 Quantum description of propagating fields

Classically, when considering quasimonochromatic propagating fields, it is natural to model the evolution of the system as a function of the propagation direction, z. The field at z can then be decomposed into a complete set of orthonormal temporal modes which act locally. One might be tempted to describe the quantum fields in an analogous manner by quantizing the temporal modes which interact with the fixed atom at time t as, $[a(t), a^\dagger(t')] = \delta(t - t')$. The field operator could then be decomposed into a complete set of orthonormal mode functions, $\phi_i(t)$, so that $a(t) = \sum_i \phi_i(t)\, c_i$, with $[c_i, c_j^\dagger] = \delta_{ij}$. Boundary conditions at some initial plane could then used to restrict the mode content, possibly to a single temporal mode.

This approach was taken by van Enk and Kimble [86] and also by Gea-Banacloche [29] who considered an analogous problem to the one we address here . They studied how errors were generated in quantum logic operations due to the fact that control pulses are not truly classical and can become entangled with the atoms with which they are interacting. Their analysis led to an effective single temporal mode theory. Though some of their conclusions are correct, one must take great care to understand the regimes under which this formalism is applicable. Consider, for example, a single photon pulse interacting with a localized two-level atom. Let us suppose that

the duration of the pulse is short compared to the natural lifetime of the atom in its excited state but sufficiently long to be considered quasimonochromatic and on resonance. Defining creation and annihilation operators for the single temporal mode associated with this pulse, the Hamiltonian, in the rotating wave approximation, appears to have the familiar Jaynes-Cummings form,

$$H = \hbar g \left(a\sigma_+ + a^\dagger \sigma_- \right), \tag{2.1}$$

where $\sigma_\pm$ are the usual raising and lowering operators associated with the two-state atom. Given the atom initially in its ground state, the solution leads to quantum Rabi oscillations,

$$|\psi(t)\rangle = \cos(gt)\ |g\rangle\,|1\rangle - i\sin(gt)\ |e\rangle\,|0\rangle\,. \tag{2.2}$$

This falsely predicts the possibility of a single photon 2π-pulse in free space, whereby the photon is perfectly absorbed and then reemitted into the original mode. In reality once the atom has absorbed the photon it will reemit into a mode consistent with its radiation pattern, not into the initial packet mode. That is, the single photon will be scattered. This emission must also obey causality; no information about the emitted photon can register on a distant detector at a space-like separated point. In the solution above, however, the atom both absorbs from and emits into a spatially delocalized photon mode in free space, violating causality.

The problems with causality arise from the faulty quantization procedure outlined above. Quantum fields must be defined over all space at an initial time (more generally on an initial space-like surface). Unitarity then ensures that *equal-time*, not *equal-space*, commutation relations are preserved. Nonequal-time commutation relations cannot generally satisfy the canonical commutation relations, being inconsistent with Poincaré invariance [10]. The exception is for free fields, or fields that behave like them (e.g. fields traveling through matter whose response is approximately linear).

We review here a formalism appropriate for treating the quantum optics of paraxial propagating fields [20]. Consider a quasimonochromatic paraxial beam with frequency ω_0 and wave number k_0. We write the positive frequency component,

$$E^{(+)}(\mathbf{x},t) = \mathcal{E}(z,t)\,\phi_T(x,y)e^{i(k_0 z-\omega_0 t)}, \tag{2.3}$$

where $\exp[i(k_0 z-\omega_0 t)]$ is the "carrier wave", $\phi_T(x,y)$ is the "transverse mode" (e.g. Gaussian), and $\mathcal{E}(z,t)$ is the slowly varying envelope, meaning its spatio-temporal variation is much slower than the carrier wavelength/frequency. We have ignored both diffraction and the vector nature of the field. It is easy to show that the free space wave equation becomes,

$$\left(\frac{\partial}{\partial t}+c\frac{\partial}{\partial z}\right)\mathcal{E}(z,t)=0 \tag{2.4}$$

for the envelope, whose solution is $\mathcal{E}(z,t)=\mathcal{E}(z-ct,0)$, i.e. propagation of the pulse envelope. We quantize by replacing the field envelope with a scaled operator,

$$\mathcal{E}(z,t) \Rightarrow \sqrt{2\pi\hbar\omega_0}\,\Psi(z,t), \tag{2.5}$$

which satisfies the canonical equal-time commutation relation [20],

$$\left[\Psi(z,t),\Psi^\dagger(z',t)\right]=\delta(z-z'). \tag{2.6}$$

This commutator is equivalent to that of a nonrelativistic massive Bose gas in one dimension. Here the carrier wave plays the role of the rest mass and the slowly varying envelope plays the role of small fluctuations around the mass shell. The free field Hamiltonian (removing the carrier wave energy) takes the form,

$$H_F = c\int dz\,\Psi^\dagger(z)\left(-i\hbar\frac{\partial}{\partial z}\right)\Psi(z), \tag{2.7}$$

whose Heisenberg equation of motion gives the wave equation above. This Hamiltonian is nothing but the second quantized version of the energy of a photon $E=cp$.

Consider an atom interacting with the field. In the electric-dipole and rotating wave approximation the interaction Hamiltonian is,

$$H_{AF} = \int d^3x \ |\Phi(\mathbf{x})|^2 \, d \left(E^{(+)}(\mathbf{x})\sigma_+ + E^{(-)}(\mathbf{x})\sigma_- \right), \tag{2.8}$$

where d is the dipole matrix element and $\Phi(\mathbf{x})$ is the atom's center of mass wave function. We take the atom to be trapped, having center of mass wave function $\Phi(\mathbf{x}) = f_T(x,y)\, f_L(z)$ [1]. Then the interaction Hamiltonian becomes,

$$\begin{aligned} H_{AF} &= d\sqrt{\frac{2\pi\hbar\omega_0}{A}} \int dz \ |f_L(z)|^2 \left(\Psi(z)\sigma_+ + \Psi^\dagger(z)\sigma_- \right) \\ \text{where } &\int dxdy \, |f_T(x,y)|^2 \, \phi_T(x,y) \equiv \frac{1}{\sqrt{A}}, \end{aligned} \tag{2.9}$$

A being the effective area of the mode interacting with the atom. Let us go to the interaction picture by including the free evolution of the atom and field in the interaction Hamiltonian. Assuming the carrier wave is on resonance,

$$H_{AF}(t) = d\sqrt{\frac{2\pi\hbar\omega_0}{A}} \int dz \ |f_L(z)|^2 \left(\Psi(z-ct)\sigma_+ + \Psi^\dagger(z-ct)\sigma_- \right).$$

Finally, given a set of orthonormal functions (" longitudinal modes") $\{\phi_i(z)\}$, chosen to be real without loss of generality,

$$\Psi(z) = \sum_i \phi_i(z) a_i, \tag{2.10}$$

$$H_{AF}(t) = d\sqrt{\frac{2\pi\hbar\omega_0}{A}} \sum_i \int dz \ |f_L(z)|^2 \, \phi_i(z-ct) \left(a_i\sigma_+ + a_i^\dagger\sigma_- \right). \tag{2.11}$$

The Hamiltonian in Eq. (2.11) describes the interaction of each longitudinal mode as it propagates past the atom(Fig. 2.1). Assuming this time scale is much shorter than any other dynamical scale in the problem, it is appropriate to make the Markov approximation as was done in the introductory derivation of spontaneous emission.

[1] In general, the atom volume of interest is its "coherence volume". For simplicity, we treat here the case of a pure atomic wave packet, with no loss of generality.

This coarse grains over any memory in the reservoir. To this end, we break up the z-axis into slices of size Δz, each the extent of the atom wave packet (e.g. the rms of the probability density). The Markov approximation will hold if the transit time of the field across the atomic packet, $\Delta t = \Delta z/c$, is much smaller than any time scale over which the atom changes. This is certainly an excellent approximation. Since we will not consider dynamics on a time scale smaller than Δt, we can approximate the set of atomic wavepackets, centered at each coarse grained slice, as a complete orthonormal set. That is, each slice is an approximate delta function. Then normalization of both the atomic wave packet and mode functions combine to give

$$\int dz\ |f_L(z)|^2\, \phi_i(z - ct) = \frac{1}{\sqrt{\Delta z}} \Theta_i(t) \tag{2.12a}$$

$$\Theta_i(t) = \begin{cases} 1, & (i-1)\Delta t < t \leq i\Delta t \\ 0, & \text{otherwise} \end{cases} \tag{2.12b}$$

Under this approximation the Hamiltonian takes the form,

$$H_{AF}(t) = \hbar g \sum_i \Theta_i(t) \left(a_i \sigma_+ + a_i^\dagger \sigma_- \right) \tag{2.13}$$

$$\text{where } \hbar g = dE_{\text{vac}} = d\sqrt{\frac{2\pi\hbar\omega_0}{Ac\Delta t}}$$

This result has a clear interpretation. The traveling wave configuration is effectively multimode, with each member of the set being a traveling packet "mode-matched" to the atom. The coupling constant g depends on this mode volume. This picture is equivalent to a model of decoherence discussed by Brun [12] in which a "flying qubit" passes over a "system qubit", the former acting as an irreversible reservoir (through its continuous spatial degrees of freedom) to carry information away from the system, thereby leading to decoherence. In our problem a given harmonic oscillator (mode of the electromagnetic field) flies over the qubit, becomes entangled with it, and then flies away. This too leads to decoherence, as we describe in the next section.

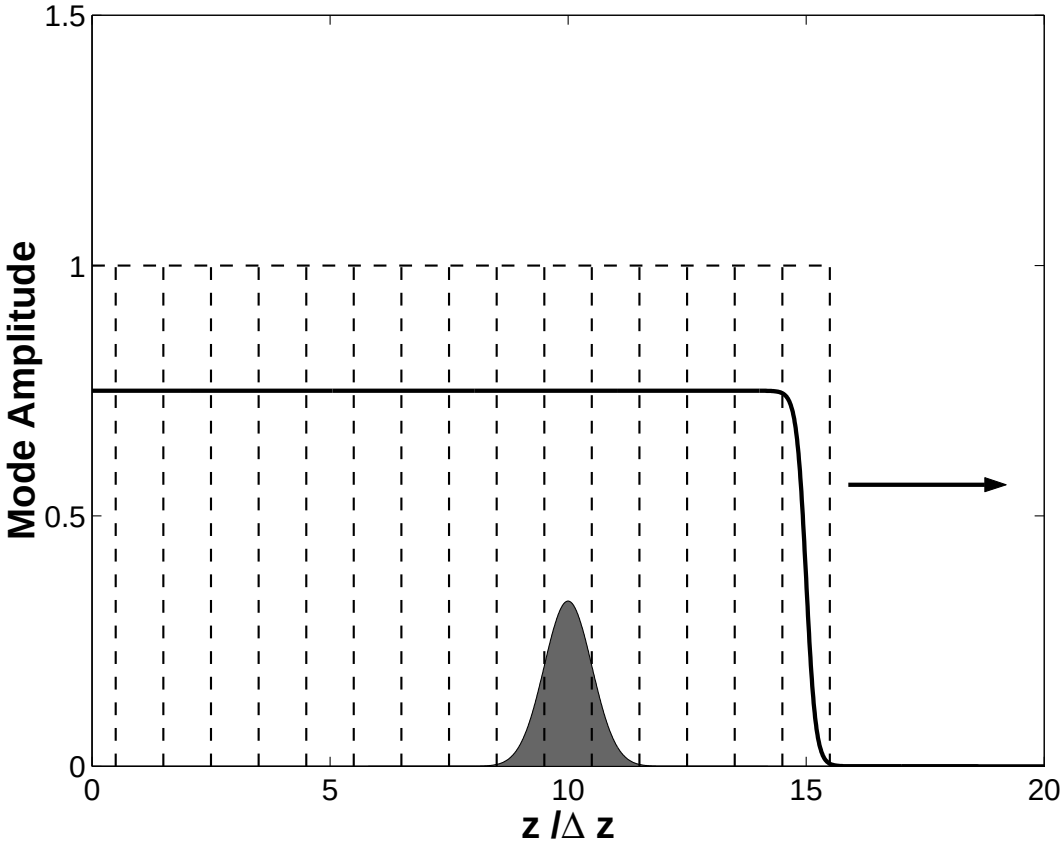

Figure 2.1: An initial traveling wave pulse (solid line) is broken up into many smaller modes $\{\phi_i(z)\}$ (dashed line). The wave packet of the interacting atom (gray) has the same width as the mode functions (Δz).

2.2 The Rabi interaction for traveling waves

2.2.1 Interaction with a laser beam

We consider first the case of a resonant laser beam interacting with a trapped two-level atom. The state of the field is described by a tensor product of identical coherent states for each traveling mode packet,

$$|\psi\rangle_{\text{beam}} = \bigotimes_i |\alpha\rangle_i \,, \tag{2.14}$$

where the amplitude is given by the mean number of photons in time slice Δt, $|\alpha|^2 = P\Delta t/(\hbar\omega_0)$, with P the power of the laser beam. More precisely, the state of the beam is a statistical mixture of states of the form above, averaged over the common, but unknown, phase of the complex amplitude α, as described by van Enk and Fuchs [85]. The actual value of the phase plays no role in the analysis to follow, so we choose it to be fixed with no loss of generality. In order to distinguish coherent effects from decoherence we transform by a unitary displacement of the field states to the vacuum, using the so call Mollow transformation [**?**],

$$|\Psi\rangle \Rightarrow D^{-1}(\{\alpha\})\,|\Psi\rangle \,, \quad A \Rightarrow D^{-1}(\{\alpha\})\,A\,D(\{\alpha\}) \,. \tag{2.15}$$

In this picture,

$$\begin{aligned} H_{AF}(t) &= \hbar g\alpha\,(\sigma_+ + \sigma_-) + \hbar g \sum_i \Theta_i(t) \left(a_i\sigma_+ + a_i^\dagger\sigma_-\right) \\ &= H_{\text{coh}} + H_{\text{AV}}. \end{aligned} \tag{2.16}$$

The coherent term is classical Rabi flopping at a frequency $\Omega = 2g\alpha = d\sqrt{8\pi I/\hbar^2 c}$, with I the beam intensity (cgs units, as used throughout). The second term is the atom-vacuum coupling for the traveling wave modes only (i.e. the paraxial modes of the beam) [37].

We can now proceed with the standard Markov analysis to derive the Master equation. The initial atom-vacuum state is uncorrelated. After a time Δt, one of the modes becomes entangled with the atom through the atom-vacuum coupling. The Linblad ("jump") operator, L, is defined by [12],

$$\langle 1|\, U_{\rm AV}(\Delta t)\,|0\rangle = \frac{-i}{\hbar}\Delta t\,\langle 1|\, H_{\rm AV}\,|0\rangle = L\sqrt{\Delta t}. \tag{2.17}$$

Plugging in the Hamiltonian from Eq. (2.16), we arrive at,

$$\begin{aligned} L &= g\sqrt{\Delta t}\,\sigma_- = d\sqrt{\tfrac{2\pi\hbar\omega_0}{Ac}}\,\sigma_- \equiv \sqrt{\kappa}\,\sigma_- \\ \text{where } \kappa &= d^2\left(\tfrac{2\pi k_0}{\hbar A}\right) = \Gamma\left(\tfrac{3\pi}{2k_0^2 A}\right) \equiv \Gamma\left(\tfrac{\sigma_{\rm eff}}{A}\right), \end{aligned} \tag{2.18}$$

is the measurement strength, Γ the spontaneous emission rate and $\sigma_{\rm eff}$ the effective cross section for scattering out of the paraxial modes. By determining these jump operators, we compactly derive the master equation, equivalent to that obtained using a the usual system-reservoir approach after tracing over the unmeasured bath [62, 28, 56],

$$\begin{aligned} \frac{d\rho}{dt} &= \frac{-i}{\hbar}\left[H_{\rm coh},\rho\right] - \frac{1}{2}\left\{L^\dagger L,\rho\right\} + L\rho L^\dagger \\ &= \frac{-i}{\hbar}\left[H_{\rm coh},\rho\right] - \frac{\kappa}{2}\left\{\sigma_+\sigma_-,\rho\right\} + \kappa\,\sigma_-\rho\sigma_+. \end{aligned} \tag{2.19}$$

This equation has a familiar and appealing form. It is none other than the master equation for a decaying laser-driven atom [62], but with $\Gamma \to \kappa$. The decay rate is due to the entanglement between the atom and the laser modes. Note, κ is independent of Δt, which acts as a fictitious quantization volume and so must be absent from any physical quantities such as the measurement strength.

The measurement strength is also independent of the laser power $|\alpha|^2$. In particular we may turn off the laser ($\alpha \to 0$), and the measurement strength will remain the same. The ratio $\kappa/\Gamma = \sigma_{\rm eff}/A$ may thus be interpreted as the fraction of spontaneous emission into the paraxial modes. In support of this interpretation note that the mode area A can never be made smaller than the diffraction limit $A \sim 1/k_0^2$, so

at most $\kappa \sim \Gamma$. Moreover, once the beam becomes focused to such a small spot size, one can no longer neglect the vector nature of the atom field coupling which further decreases the measurement strength [87].

From Eq. (2.18) we can determine how continuous measurement by the laser beam acts to decohere the atom. For a paraxial beam we require that $\sigma_{\text{eff}}/A \gg 1$, so that diffraction effects are minor. Then decay due to entanglement with the laser modes is small compared to decay due to spontaneous emission into 4π steradians. In agreement with the conclusions of [86, 29], errors in coherent control pulses due to the quantum nature of the interaction can be neglected if spontaneous emission is also negligible during the duration of the interaction.

2.2.2 Ruminations on laser decoherence

The decoherence engendered by a laser can be attributed to the fraction of the vacuum modes it occupies in the unitarily displaced frame. In the original frame the nonzero amplitude in the laser modes drives the system to undergo nontrivial evolution and interferes with the scattered radiation, enhancing or diminishing the scattering in specific directions. This interference can alter the character of the spontaneous emission observed in the displaced frame transforming it into some combination of spontaneous and stimulated emission in the original frame. So while it is correct to note that laser induced decoherence is equivalent to spontaneous emission (in the transformed frame), it is not completely accurate to state that laser induced decoherence is solely spontaneous emission.

Another interesting point was raised in a papers by M. Ozawa and J. Gea-Banachloche [**?**]. Any control field acting upon a system under a conservation law must induce decoherence. In the case of a laser interacting with a two level atom the rotating wave approximation assures that the total number of excitations is con-

served,

$$\frac{1}{2}\sigma_z + \sum_i a_{\rm i}^\dagger a_{\rm i} = 0 \tag{2.20}$$

where the sum is over all field modes which can exchange excitations with the system. Starting with the atom in a pure eigenstate of σ_z, e.g. $|0\rangle$, no pure atomic state which is not an eigentstate of σ_z, e.g. $(|0\rangle + |1\rangle)/\sqrt{2}$, may be produced. Production of such states necessarily entails entanglement with with the control field. This observation is beautifully explained by the recent work on reference frames [**?**]. One can derive a rigorous bound on the probability of error for a Hadamard gate in terms of the variance of the number operator $\sigma(n)^2$ in the initial field state to be [**?**]

$$P_{\rm error} \geq \frac{1}{4}\frac{1}{1+4\sigma(n)^2}. \tag{2.21}$$

For large n in a coherent state this becomes as $P_{\rm error} \geq 1/(16|\alpha|^2)$. Our estimate of the error induced by the paraxial modes for a laser implemented Hadamard gate is

$$P_{\rm error} = \kappa t_{\rm Hadamard} = \frac{\pi^2}{16|\alpha|^2} \geq \frac{1}{16|\alpha|^2}. \tag{2.22}$$

Thus scattering into the laser modes accounts for the decoherence required by energy conservation.

2.2.3 Interaction with a single photon

In Sec. 2.1 we showed how a quantization procedure in terms of nonequal-time commutators can lead to a false prediction of single photon coherent Rabi flopping in free space. In this subsection we use our formalism to show how a quasimonochromatic and paraxial propagating single photon wave packet drives a two-level atom.

We take the initial state of the system to be a single photon wave packet with the atom in its ground state,

$$|\Psi(0)\rangle = a^\dagger[f]\,|{\rm vac}\rangle \otimes |g\rangle_{\rm A}\,. \tag{2.23}$$

The operator $a^\dagger[f] = \int dz \Psi^\dagger(z) f(z)$ creates a delocalized single photon state with slowly varying pulse envelope $f(z)$ [19]. For simplicity we use a square pulse of duration $\tau = N\Delta t$. In this case we can expand $f(z)$ in a symmetric sum of coarse-grained modes each having length $\Delta z = \Delta t/c$,

$$a^\dagger[f] = \frac{1}{\sqrt{N}} \sum_{i=0}^{N-1} a_i^\dagger. \tag{2.24}$$

The state will evolve according to the Hamiltonian in Eq. (5.35) which commutes with the total number of excitations in the system. Neglecting, for now, the possibility of spontaneous emission into other transverse field modes, the total number of excitations will be preserved. The state at all times must then have the form

$$|\psi(t)\rangle = \left(\sum_j A_j(t) a_j^\dagger + A_e(t)\sigma_+ \right) |\text{vac}, g\rangle \,. \tag{2.25}$$

Consider the evolution of the system over the short interval $(t_k, t_k + \Delta t]$, where $t_k = k\Delta t, 0 \leq k \leq N-1$. We can define a map for the state between two successive time steps,

$$|\psi(t_k)\rangle = e^{-iH_k \Delta t/\hbar} |\psi(t_{k-1})\rangle \,, \tag{2.26}$$

where $H_k = \hbar g \left(a_k \sigma_+ + a_k^\dagger \sigma_- \right)$. Using ansatz (Eq. 2.25) we are led to the recursion relations,

$$A_{j\neq k}(t_k) = A_j(t_{k-1}), \tag{2.27a}$$

$$A_k(t_k) = A_k(t_{k-1})c - iA_e(t_{k-1})s, \tag{2.27b}$$

$$A_e(t_k) = A_e(t_{k-1})c - iA_k(t_{k-1})s. \tag{2.27c}$$

Here $s \equiv \sin\sqrt{\kappa\Delta t}$ and $c \equiv \cos\sqrt{\kappa\Delta t}$. The measurement strength $\kappa = g\sqrt{\Delta t}$ is the same as in Eq. (2.18).

These coupled algebraic equations can be solved for the amplitudes. Repeated application of the Eq. (2.27a) at all times $t_k < t_j$, shows that $A_k(t_{k-1}) = A_k(0) =$

$N^{-1/2}$. Inserting this result into Eq. (2.27c),

$$A_e(t_k) = A_e(t_{k-1})c - \frac{is}{\sqrt{N}}. \tag{2.28}$$

This equation admits a simple series solution,

$$A_e(t_k) = -\frac{is}{\sqrt{N}}\frac{1-c^k}{1-c}. \tag{2.29}$$

Assuming $\sqrt{N} \gg 1$, i.e. the envelope $f(z)$ is much broader than the coarse graining, we may take the limit of $A_e(t)$ as $N \to \infty$ holding $\tau = N\Delta t$. This yields,

$$A_e(t) \approx -\frac{2i}{\sqrt{\kappa\tau}}\left[1 - e^{-\kappa t/2}\right]. \tag{2.30}$$

The solution given in Eq. (2.30) is based on the fundamental assumption that the evolution of the state is unitary, i.e. we consider a closed quantum system consisting of the atom and paraxial field modes. In the continuum limit, this yields an effective decay due to emission into the included paraxial modes at rate κ, but it excludes decay into all others modes which, taken together, give a total spontaneous emission rate Γ. Since we showed in Sec. 2.2.1 that $\kappa \ll \Gamma$, this solution is not self-consistent. To rectify this, during the time interval Δt we must allow for a small probability of spontaneous emission, P_{spont}, into non-paraxial modes. By not including these modes in our system, the state ket $|\psi\rangle$ evolves according to an effective non-Hermitian Hamiltonian [28] with decaying norm, $\langle\Psi|\Psi\rangle = 1 - P_{\text{spont}}$. Eq. (2.27c) then reads,

$$A_e(t_k) = A_e(t_{k-1})ce^{-\gamma\Delta t/2} - iA_k(t_{k-1})s, \tag{2.31}$$

where γ is the spontaneous emission into all non-paraxial modes. Employing the initial condition and taking the limit $\Delta t \to 0, N\Delta t = \tau$ yields,

$$\frac{d}{dt}A_e(t) = -\frac{1}{2}(\gamma+\kappa)A_e(t) - i\sqrt{\frac{\kappa}{\tau}}. \tag{2.32}$$

Solving this equation with $\gamma = 0$, using the initial condition $A_e(0) = 0$, will give the same result as in Eq. (2.30).

Before considering the solution to this differential equation, consider the slightly altered situation in which the field starts in the vacuum state, and the atom in the excited state. In this case it is easy to see that the second term on the right side of Eq. (2.32) will vanish. Then the equation becomes,

$$\frac{d}{dt}A_e(t) = -\frac{1}{2}(\gamma + \kappa)A_e(t), \tag{2.33}$$

with the initial condition $A_e(0) = 1$. This must give the standard exponential decay due to spontaneous emission in the vacuum

$$A_e(t) = e^{-\frac{1}{2}\Gamma t}. \tag{2.34}$$

This allows us to equate $\Gamma = \gamma + \kappa$, where κ is again seen to be the spontaneous emission rate due to the contribution of the modes in the paraxial beam.

The general solution to Eq. (2.32) is,

$$A_e(t) = -\frac{2i}{\Gamma}\sqrt{\frac{\kappa}{\tau}}\left(1 - e^{-\Gamma t/2}\right), \tag{2.35}$$

holding for times $0 \leq t \leq \tau$. The probability of the atom being in the excited state is then,

$$P_e(t) = 4\frac{\kappa}{\Gamma^2\tau}\left(1 - e^{-\Gamma t/2}\right)^2, \tag{2.36}$$

during the same interval. This is a monotonically increasing function of t, and so achieves its maximum at the upper limit $t = \tau$, after which the excitation probability can only decay(Fig. 2.2). Then the maximum probability for any τ can be found by solving,

$$\frac{d}{d\tau}P_e(\tau) = 0 \rightarrow \Gamma\tau \approx 2.5. \tag{2.37}$$

At this point the probability is $P_e \approx .8\kappa/\Gamma$, which is necessarily less than 1 given that $\kappa/\Gamma < 1$ as previously discussed. Thus, in the paraxial approximation, no single photon pulse can be constructed that excites an atom with certainty.

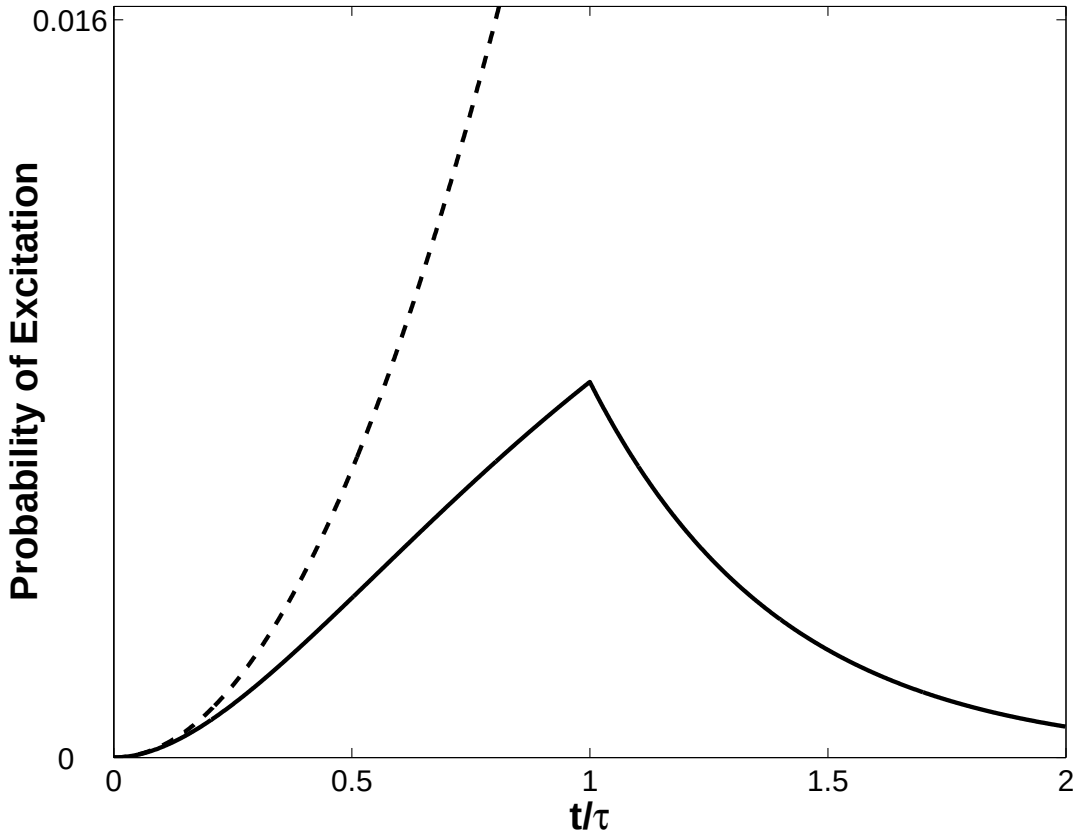

Figure 2.2: The probability for a single photon in free space to excite a two-level atom (solid line) differs significantly from the standard Rabi flopping solution, in which an atom is coupled to a photon in a single-mode cavity (dashed line). The parameters used here are $\Gamma\tau = 2.5$, and $\kappa/\Gamma = 1/50$ (see text).

This result is, of course, not surprising. Symmetry ensures that the only single photon pulse capable of exciting an atom with unit probability is the time reversal of a spontaneously emitted packet [15]. Such a pulse represents the vector spherical harmonic associated with the atomic radiation pattern (assuming emission on a transition with well defined angular momentum), a field not captured in the scalar paraxial approximation. Moreover, even including the vector nature of the field beyond paraxial will not be sufficient to yield high excitation probability. The field

must be well "mode matched" to the the atom's radiation pattern to give strong coupling between the atom and a single photon in free space [87].

2.2.4 Interaction with a large n-Photon Fock Pulse

In the last subsection we showed that in free space the coupling of a single photon to an atom will not lead to coherent Rabi oscillations. In contrast, for an n-photon Fock state with a large n, we expect the system to be dominated by stimulated emission. A rigorous treatment of this problem using the Bethe-Ansatz was given by V. I. Rupasov and V. I. Yudson [59]. We show here how this phenomenon is recovered simply in the present formalism.

In general, an arbitrary division may be envisioned in Hilbert space that separates system from reservoir. In Sec. 2.1 the system was chosen to be the paraxial field modes plus the atom. Alternatively we may take the system to consist of the atom interacting with the single pulse mode defined by creation operator $a^\dagger[f]$ in Eq. (2.24), with all other modes making up the environment. Such a choice can always be made, and cannot change the physics. We may then choose to ignore all environmental modes if $\Gamma\tau \ll 1$, with the caveat that any effects that occur in the system must be have scales much larger than $\Gamma\tau$ in order to be considered valid.

Consider a pulse of length τ such that $\Gamma\tau \ll 1$. Further, take the state of the system to only have excitations in this pulse mode such that,

$$|\psi(0)\rangle = \frac{1}{\sqrt{n!}} \left(a^\dagger[f]\right)^n \otimes |0, g\rangle = |n, g\rangle \,. \tag{2.38}$$

The rest of the modes are in the vacuum state and are treated as an environment. Ignoring terms of order $\Gamma\tau$ the system evolves under the single mode Hamiltonian

$$H = \hbar g_{\text{eff}} \left(a[f]\sigma_+ + a^\dagger[f]\sigma_-\right), \tag{2.39}$$

This is none other that the Jaynes-Cummings Hamiltonian restricted to an initial manifold with n excitations and having effective coupling constant

$$\hbar g_{\text{eff}} = d\sqrt{2\pi\hbar\omega_0/V_{\text{pulse}}}, \tag{2.40}$$

where $V_{\text{pulse}} = Ac\tau$ is the pulse volume. The system undergoes the familiar coherent Rabi flopping within the two dimensional manifold, as in Eq. (2.2),

$$|\psi(t)\rangle = \cos(g_{\text{eff}}\sqrt{n}t)\ |g\rangle\,|n\rangle - i\sin(g_{\text{eff}}\sqrt{n}t)\ |e\rangle\,|n-1\rangle\,. \tag{2.41}$$

This solution applies to the single photon case as well. The probability amplitude from Eq. (2.35) limits to,

$$A_e(t) \to -ig_{\text{eff}}t\,(1 + O(\Gamma t))\,, \tag{2.42}$$

which is the correct limit of sinusoidal Rabi oscillation. However during the pulse duration not even a single oscillation can occur since $g_{\text{eff}} = \sqrt{\kappa/\tau} \ll 1/\tau$. Thus, for true oscillations to occur, one must have

$$g_{\text{eff}}\sqrt{n} \gtrapprox \frac{1}{\tau} \quad \text{or} \quad n\Gamma\tau \gtrapprox \frac{A}{\sigma_{\text{eff}}}. \tag{2.43}$$

The last inequality can be interpreted as saying that the mean number of photons emitted via stimulated emission into the pulse must dominate over spontaneous emission, even when the spontaneous photons are paraxial. When these conditions hold we may consistently ignore all initially unoccupied modes and recover dynamics in agreement with the usual Jaynes-Cummings Hamiltonian. The multimode description of the field becomes superfluous.

Finally, what is the measurement strength associated with probing an atom using a large photon number Fock state pulse? Unlike the coherent state case, the field does not factorize into uncorrelated temporal slices. In fact, when viewed in terms of the coarse grained modes, the Fock pulse in highly *entangled*. Detection of photons at the

leading edge of the pulse will introduce new fluctuations in the trailing edge, which has yet to interact with the atom. This implies that the usual Markov approximations do not hold. The Fock pulse is most naturally treated as part of the "system" rather than an "environment" which continuously carries information away from the atom.

2.3 QND Measurement via Faraday Polarization Spectroscopy

The resonant interaction considered up to this point, though fundamental in nature, has little practical application to the problem of continuous measurement in free space since the measurement strength is always bounded from above by the spontaneous emission rate. We thus turn our attention to an off-resonant interaction which is considered in much more detail later in this dissertation, Chap. 4. In particular, we consider the problem of measuring a spin component of an atomic ground state through the Faraday effect wherein the linear polarization of a probe laser rotates by an amount proportional to the magnetization of the sample. This interaction implements quantum nondemolition measurement (QND) of the atomic spin, measuring this variable without perturbing its value [43, 64]. Such an interaction has been applied to ensembles of atoms to produce spin squeezed states [44, 33] and to demonstrate entanglement between two spatially separated ensembles [38].

The physical interaction is given by the induced dipole Hamiltonian

$$H_{\text{int}} = -\mathbf{E}^{(+)} \cdot \overleftrightarrow{\alpha} \cdot \mathbf{E}^{(-)}, \tag{2.44}$$

where $\overleftrightarrow{\alpha}$ is the atomic polarizability tensor and $\mathbf{E}$ is the complex electric field amplitude. Expressing this equation in terms of irreducible tensor components, the interaction can be decomposed into an effective scalar, vector, and symmetric rank-2 contribution. This decomposition as well as a much more thorough examination of

this Hamiltonian can be found in Chap. 4. We consider here the case of alkali atoms probed on the so-called D2 line $S_{1/2} \rightarrow P_{3/2}$, for which the ground state atomic polarizability operator is [21]

$$\overleftrightarrow{\alpha} = \alpha_{\text{lin}} \left(1 + \frac{1}{2} \left(\mathbf{e}_+ \mathbf{e}_+^* - \mathbf{e}_- \mathbf{e}_-^* \right) \sigma_z \right). \tag{2.45}$$

Here $\mathbf{e}_\pm$ are the right and left helicity vectors relative to the quantization axis along the probe propagation direction, $\sigma_z = |\uparrow\rangle\langle\uparrow| - |\downarrow\rangle\langle\downarrow|$ is the Pauli spin operator for the ground state electron, and α_{lin} is the atomic polarizability for fields with linear polarization. The first term gives rise to an effect that depends solely on the field intensity, and is not relevant to our current considerations as we consider the intensity of the lasers to be fixed. The term proportional to σ_z depends on the field ellipticity. Clearly the irreducible rank-2 component vanishes here, as it cannot be supported within a two level ground state [35, 21][2].

Under the paraxial approximation we take the field to be approximately a plane wave with two polarization vectors. The quantum field associated with the complex amplitude is

$$\mathbf{E}^{(+)} = \sqrt{\frac{2\pi\hbar\omega}{V}} \left(a_- \mathbf{e}_- + a_+ \mathbf{e}_+ \right) e^{ikz}, \tag{2.46}$$

where V is the effective quantization volume for the propagating mode. Substituting this into Eq. (2.44), the quantum Hamiltonian becomes,

$$H_{\text{int}} = -\frac{2\pi\alpha_{\text{lin}}}{V}\hbar\omega \left[(N_+ + N_-) + \frac{1}{2} (N_+ - N_-) \sigma_z \right], \tag{2.47}$$

where $N_\pm$ is the number operator for photons in the positive or negative helicity states. The scalar term gives rise to an overall phase shift (index of refraction) and thus can be absorbed into the free field Hamiltonian. The vector term gives rise to

[2]This result generalizes under the assumption that the probe detuning is large compared to the hyperfine splitting in the $P_{3/2}$ manifold. We can use the Lande projection theorem to make the substitution $\hat{\sigma}_z \Rightarrow \hat{\Sigma}_z \equiv \hat{F}_z/F$ where F is the total ground-state angular momentum including nuclear spin.

the Faraday effect. Recognizing $J_z = (N_+ - N_-)/2$ as the total field helicity, the effective interaction Hamiltonian takes the QND form,

$$H_{\text{int}} = -\frac{2\pi\alpha_{\text{lin}}}{V}\hbar\omega J_z\sigma_z. \tag{2.48}$$

Under this Hamiltonian the photon spin becomes correlated with the atom's magnetic moment and thus the laser polarization may act as a meter for the atomic spin. Since σ_z also commutes with the system-meter Hamiltonian it is clearly a QND variable [62].

Our Hamiltonian still contains the undefined quantization volume V. To rectify this we follow the formalism introduced in Sec. 2.1. Introducing propagating modes of duration Δt so that $V \to Ac\Delta t$ the Hamiltonian becomes,

$$H_{\text{int}} = -\sum_i 2\frac{\hbar\chi}{\Delta t}\Theta_i(t)J_z\sigma_z, \tag{2.49}$$

where $\chi = \pi\alpha_{\text{lin}}\omega/(cA) \approx (\sigma_0/A)[\Gamma/(-2\Delta)]$. Here Δ is the (far)detuning from the atomic resonance with linewidth Γ, and σ_0 is the on resonance absorption cross-section for linear polarization.

With the Hamiltonian so defined, the evolution of the system may be calculated. The system shall consist of an atom interacting with a laser beam that is linearly polarized in the x-direction. The initial state of the laser is then,

$$|\Phi\rangle_{\text{probe}} = \otimes_i \frac{1}{\sqrt{2}}\left(|\alpha\rangle_{ix}|0\rangle_{iy}\right), \tag{2.50}$$

where x and y label the two orthogonal linear polarization modes. As in Sec. 2.2.1 $|\alpha|^2 = P\Delta t/\hbar\omega_0$, with P the power in the beam. Given this initial state for the field, we may define the marginal density operator for the atom alone by tracing over the field at time t. Since the Hamiltonian (Eq. 2.44) only couples the atom to the k'th field mode in time interval $(t_k, t_k + \Delta t]$, the reduced atomic state evolves during this interval as,

$$\rho(t_k + \Delta t) = \text{Tr}_k\left[U_i|\alpha\rangle_{ix}\langle\alpha|_{ix} \otimes |0\rangle_{iy}\langle 0|_{iy} \otimes \rho(t_k)U_i^\dagger\right]. \tag{2.51}$$

In the interaction picture the unitary evolution becomes,

$$\begin{aligned} U_i \left|\alpha\right\rangle_{ix} \left|0\right\rangle_{iy} &= e^{-i\chi\sigma_z(N_{+i}-N_{-i})} \left|\alpha\right\rangle_{ix} \left|0\right\rangle_{iy}, \\ &= \left|\alpha\cos(\chi\sigma_z)\right\rangle_{xi} \left|-\alpha\sin(\chi\sigma_z)\right\rangle_{yi}. \end{aligned} \tag{2.52}$$

This expression should be interpreted in the context of a matrix element, given that atomic operators appear in the labels for the field kets. Clearly, the field and atomic states will generally become entangled by the interaction.

The map in Eq. (2.51) constitutes a continuous measurement on the field. To see this explicitly, we must expand in powers of Δt, and since $|\alpha|^2 \propto \Delta t$, this is equivalent to an expansion of the state kets in Eq. (2.52) in powers of α. In the Fock (photon number) basis we have,

$$U_i \left|\alpha\right\rangle_{ix} \left|0\right\rangle_{iy} \approx \left(1 - \frac{|\alpha|^2}{2}\right) \left[\left|0\right\rangle_{xi} \left|0\right\rangle_{yi} + \alpha\cos(\chi\sigma_z) \left|1\right\rangle_{xi} \left|0\right\rangle_{yi} - \alpha\sin(\chi\sigma_z) \left|0\right\rangle_{xi} \left|1\right\rangle_{yi}\right] \tag{2.53}$$

Substituting this back into Eq. (2.51) one finds,

$$\begin{aligned} \rho(t_k + \Delta t) = \rho(t_k) + |\alpha|^2 \left[-\rho(t_k)\right. \\ \left. + \sin(\chi\sigma_z)\rho(t_k)\sin(\chi\sigma_z) + \cos(\chi\sigma_z)\rho(t_k)\cos(\chi\sigma_z)\right]. \end{aligned} \tag{2.54}$$

This form may be further simplified since $\chi \ll 1$ for a single atom probed by a far off resonance laser. Taking the limit, $\Delta t \to 0$, and keeping terms to second order in χ gives the master equation,

$$\begin{aligned} \frac{d\rho}{dt} &= \frac{P\chi^2}{\hbar\omega_0} \left[\sigma_z\rho\sigma_z - \frac{1}{2}\{\sigma_z^2, \rho\}\right] \\ &= -\frac{\kappa}{2}\left[\sigma_z, \left[\sigma_z, \rho\right]\right], \end{aligned} \tag{2.55}$$

where the measurement strength can be easily identified from the familiar Linblad form of the mater equation [28] as,

$$\kappa = \frac{P\chi^2}{\hbar\omega_0}, \tag{2.56}$$

Note that the steady state solutions to Eq. (2.55) are the Dicke states, so this technique provides a QND measurement of spin. This expression was also derived by Thomsen and Wiseman in the context of control of atom-laser coherence [81].

The physics of the continuous measurement under consideration here differs substantially from that of the resonant Jaynes-Cummings interaction studied in Sec. 2.2. Here the measurement strength depends upon the power in the beam, whereas the previous result had no such dependence. For the resonant case, κ could be explained as arising from those spontaneous photons emitted into paraxial modes. In contrast, the dependence of the QND measurement on the laser power indicates that the measurement strength is due to the coherent redistribution of photons between the polarization modes in a manner depending on the atomic state.

2.4 Summary and Discussion

Continuous quantum measurement, once studied only in gedanken experiments, can now be realized in laboratory applications [45, 74]. Such applications utilize the ability to continuously gather information from a probe coupled to a quantum system. The system state then evolves under a stochastic master equation, characterized by the measurement strength. In this chapter we examined how one may derive the measurement strength for paraxial laser probes in free space by considering two examples. We considered first the fundamental system of an atom coupled to a laser beam. Classically the atom-laser interaction leads to Rabi flopping which is often used to manipulate coherent superpositions of atomic states. In particular laser control pulses can be used to implement quantum logic gates [69]. Quantum mechanically continuous measurement of the atom by the quantum laser pulse can lead to entanglement between the system and the probe. In the next chapter (Chap. 3) we bound the generated entanglement and explore its properties further. Such

entanglement generally induces errors in the system state, this is not a concern for laser controlled atoms in free space as the measurement strength is bounded above by the total spontaneous emission rate and can thus be neglected for short interaction times. In fact, the measurement rate may be attributed to spontaneous emission into the paraxial modes, which will always be small compared to emission into 4π steradians with the appropriate vector field. We also studied the distinction between continuous observation by a coherent beam and by a pulse with well defined photon number. In the latter case correlations between the quantum fluctuations at different points in the pulse disallow a clean separation between system and probe. Instead, the entire atom-field system will coherently Rabi flop if the number of photons is sufficiently large. For a single photon, however, we showed that Rabi flopping cannot occur in free space. Such a result is essential lest a distant detector be able to instantly sense the presence of the atom. This highlights the need to treat the propagation of quantum fluctuations in a traveling wave geometry with great care to avoid contradictions with causality.

Faraday rotation of an off resonant polarized beam offers another method of continuous measurement, which method will be put to use in Chap. 5. In this chapter we derived the measurement strength associated with this QND measurement of the atomic spin, and found it to be proportional to laser intensity. This is a direct result of the measurement redistributing photons between pairs of occupied modes, in contrast to the resonant Rabi interaction where measurement results from spontaneous emission. Since the measurement strength is proportional to the laser intensity it can be made much larger than the spontaneous emission rate. Of course spontaneous emission is not the only source of noise. In order to see the effects of quantum back-action the quantum "projection" noise [80] must be large compared all other noise sources, such as those due to photo-detection. This implies that an experiment in which the back-action is important must enhance the coupling constant without increasing the shot-noise, possibly through the use of an optical cavity or by

maintaining a large ensemble of atoms collectively coupled to the probe. The latter approach has led to the observation of spin squeezing [44, 33] and ensemble entanglement [38]. In the weak measurement regime this interaction allows for reconstruction of the quantum state as shown in Chap. 5.

Chapter 3

Atomic entanglement with light

The last chapter delved into the question of how entanglement between an atom and a traveling wave probe, or more specifically the paraxial modes of the EM field that constitute the traveling wave, can lead to decoherence of the atomic system. Though this decoherence was shown to be a negligible source of error in quantum operations, the question of how much entanglement exists between these paraxial modes and the laser is still of interest. This entanglement might prove useful as a resource in some quantum communication or quantum computation scheme[51]. Moreover, by determining how much entanglement one can generate in free space, we obtain a benchmark for comparison with other entanglement generation schemes. For example, the entanglement generated in a cavity QED geometry [39] could be compared to the entanglement that would be generated in the absence of the resonator.

Quantifying the entanglement generated between an atom and a laser in free space is complicated by the multimode nature of the field in a traveling wave geometry. Sec. 2.1 demonstrated that the hilbert space describing the laser modes is the tensor product of many independent paraxial modes. Additionally, the laser and atom do not form a closed system, as the other vacuum modes of the field interact with

the atom. Since spontaneous emission into these unoccupied modes dominates over quantum features within the laser modes, it is generally inconsistent to neglect their effects when calculating atom-laser entanglement.

To analyze this problem, we use the formalism developed in in the previous chapter. In Sec. 3.1, the pertinent equations of the formalism introduced in Sec. 2.1 are summarized and specialized to the particular problem at hand. We then examine the entanglement generated between the laser pulse mode and the atom in Sec. 3.2. This result is compared to similar results obtained using a closed-system single mode picture. We follow this with a calculation of an upper bound on the total entanglement generated between the atom and all modes propagating with the laser beam. A brief summary of results is presented in Sec. 3.4.

3.1 Paraxial formalism

Labeling the paraxial modes by the index i the Hamiltonian for the paraxial field and atom in the interaction picture and under the rotating wave approximation is,

$$H_{\mathrm{AF}}(t) = \hbar g \sum_i \Theta_i(t) \left(a_i \sigma_+ + a_i^\dagger \sigma_- \right) \tag{3.1}$$
$$\text{where } \hbar g = dE_{\mathrm{vac}} = d\sqrt{\frac{2\pi\hbar\omega_0}{A\Delta z}}.$$

$\Theta_i(t)$ are window functions selecting out the mode currently interacting with the atom just as before.

The nonparaxial modes which constitute the rest of the field are treated as a zero temperature reservoir into which the atom can decay. The only difference from standard spontaneous emission will be that the rate of decay is slightly reduced by

the removal of the paraxial modes.

$$\Gamma' = \Gamma\left(1 - \frac{\Omega_p}{4\pi}\right) \approx \Gamma - \kappa, \tag{3.2}$$

with Ω_p the solid angle subtended by the paraxial beam. Including the nonparaxial modes, the full master equation for the atom-paraxial field system becomes

$$\frac{d\rho}{dt} = \frac{-i}{\hbar}\left[H_{\mathrm{AF}}, \rho\right] - \frac{\Gamma'}{2}\left\{\sigma_+\sigma_-, \rho\right\} + \Gamma'\,\sigma_-\rho\sigma_+. \tag{3.3}$$

Specializing to the case at hand the paraxial modes are taken to be in an initial coherent state, corresponding to the quantum state of a laser beam. Again performing the Mollow transformation from Sec. 2.2.1 results in a unitarily equivalent dynamic, with Hamiltonian

$$\frac{d\rho}{dt} = \frac{-i}{\hbar}\left[H_{\mathrm{coh}} + H_{\mathrm{AF}}, \rho\right] - \frac{\Gamma'}{2}\left\{\sigma_+\sigma_-, \rho\right\} + \Gamma'\,\sigma_-\rho\sigma_+, \tag{3.4}$$

where H_{coh} is the coherent semi-classical Rabi-flopping Hamiltonian

$$H_{\mathrm{coh}} = \hbar g\alpha\left(\sigma_+ + \sigma_-\right), \tag{3.5}$$

and H_{AF} is still given by Eq. (3.1), but now acts in the transformed frame. Since these equations are equivalent to the initial dynamics under local unitary operations the entanglement will be unchanged. Eq. (3.4) thus serves as the basic dynamical description for our entanglement calculations.

3.2 Quantifying Entanglement

In the previous section part of the EM field, corresponding to the nonparaxial modes, was traced out to recover the master equation (Eq. 3.4). The remaining paraxial subsystem is spans a large dimensional Hilbert space, composed of a tensor product of Fock spaces for each coarse-grained wavepacket in the pulse. Such a large Hilbert

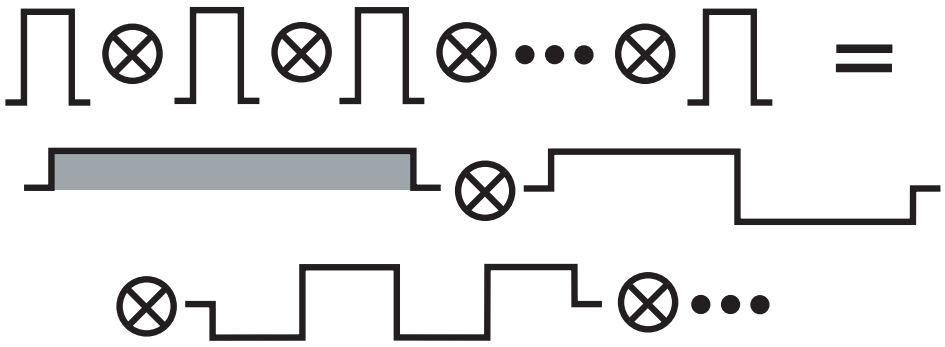

Figure 3.1: Two different modal decompositions of the paraxial field. The top line represents the local coarse-grained decomposition. The second two lines depict the Fourier decomposition, which consists of many delocalized longitudinal modes. Only the symmetric mode (laser mode) is initially excited, starting in a coherent state, and is shown here shaded. The other nonsymmetric modes (two of which are depicted) are initially in the vacuum state.

space has many subsystem decompositions, any one of which could be of interest when calculating entanglement (Fig. 3.1). In this section we consider two possible decompositions: (i) entanglement between the atom and the mode defined by the laser pulse, (ii) entanglement between the atom and the entire paraxial subsystem. The former is natural to consider when treating the laser pulse as a single mode, analogous to a Jaynes-Cummings cavity QED geometry [39]. The latter is of interest when relating the atom-laser entanglement to the measurement strength of the laser and to the error in quantum logic induced by a control pulse. The second decomposition admits an upper bound on the atom-laser entanglement which places limits on its possible use as a resource for quantum information processing.

To quantify entanglement, we use a monotone known as the "tangle" which can be related to the square of the more familiar concurrence and also to the entanglement of formation [94, 52]. For overall pure states where at least one of the systems has only two levels (is a qubit) the tangle is equal to the normalized linear entropy (or

purity) of the marginal state of either subsystem [78],

$$T\left(|\psi\rangle\langle\psi|\right) = 2\left(1 - \mathrm{Tr}_A\left[\mathrm{Tr}_B\left[|\psi\rangle\langle\psi|\right]^2\right]\right). \tag{3.6}$$

This formula can be generalized to mixed states by taking the convex roof [84]

$$T(\rho) = \min_{|\psi_i\rangle, p_i} \sum_i p_i T\left(|\psi_i\rangle\langle\psi_i|\right) \qquad \rho = \sum_i p_i |\psi_i\rangle\langle\psi_i|. \tag{3.7}$$

We choose to use the tangle instead of the full Von Neumman entropy due to its ease of calculation.

3.3 Symmetric mode entanglement

3.3.1 Calculation

We consider first the tangle between the atom an the symmetric paraxial mode (Fig. 3.1), defined by the annihilation operator,

$$a_+ = \frac{1}{\sqrt{N}} \sum_{i=1}^{N} a_i. \tag{3.8}$$

This mode defines a laser pulse of duration τ. In calculating the tangle in this decomposition all of the other field modes, nonparaxial and nonsymmetric paraxial modes, act as a reservoir which, when traced over, lead to a mixed-state description of our bipartite system. We assume $\kappa\tau \ll 1$, implying that the probability for the atom to emit a photon into one of the paraxial modes is very small. In the Mollow picture (used throughout) the Hilbert space of the quantum field may thus be truncated, allowing at most one excitation in the paraxial subsystem. Note that the atom is still allowed to spontaneously emit an arbitrary number of photons into the nonparaxial field modes. Under these assumptions the atom and the symmetric field mode both behave as two-level systems, coupled together in an overall mixed state. The tangle

for such two-level systems can be calculated using Wootters' general formula for two qubits [94].

We begin by calculating the atom-symmetric mode density matrix from Eq. (3.4) for $\kappa\tau \ll 1$. In principle, one could solve for the state of the entire atomic-paraxial system, and then trace out the nonsymmetric modes. However, even limiting all paraxial modes to at most one total excitation there are still $N+1$ possible field states, N being the number of coarse-grained modes. A more sensible approach is to keep only the "dynamic symmetric mode" at any instant (as defined below), tracing out any non-symmetric modes along the way.

Consider first a single time step $\Delta t = \Delta z/c$, with Δz the coarse-graining length. At the start of this interval the system Hilbert space has dimension $2 \otimes 2$. The system consists of the two-level atom and a quantized symmetric mode of the field composed *only* of those coarse-grained modes which have already passed the atom, and restricted to one possible excitation. Assuming $n < N$ modes have passed, the annihilation operator for this symmetric field mode will be

$$a_{+,\mathrm{n}} = \frac{1}{\sqrt{n}} \sum_{i=1}^{n} a_i. \tag{3.9}$$

After evolution over a time interval Δt, we choose a new subsystem division so that we again have a $2 \otimes 2$ system. The second subsystem will now correspond to the symmetric mode over the $n+1$ coarse-grained modes that have now passed the atom. The procedure may then be repeated to build up the full evolution, and the tangle can be calculated at each step.

The procedure for evolving the state from time t to $t + \Delta t$ is as follows. Suppose that $n < N$ time intervals have passed. The density operator ρ_n will be spanned by the basis states

$$|e\rangle\,|0\rangle_{+,n} \quad |g\rangle\,|0\rangle_{+,n} \quad |e\rangle\,|1\rangle_{+,n} \quad |g\rangle\,|1\rangle_{+,n}\,. \tag{3.10}$$

During the next interval a new coarse-grained mode impinges upon the atom. This mode starts in the vacuum (in the Mollow picture) so the new state for this composite system is

$$\rho = \rho_n \otimes |0\rangle_{n+1} \langle 0| \,. \tag{3.11}$$

Through the next time interval this state evolves under a combination of the Jaynes-Cummings Hamiltonian which couples the atom to the quantized mode, a semi-classical coherent atom-laser interaction, and spontaneous emission into the non-paraxial modes. We model this by a short time integration of the master equation, Eq. (3.4). During this time the density matrix must be expanded to include the newly interacting mode. The basis states include the previous set, Eq. (3.10), tensored with $|0\rangle_{n+1}$ for the newly added mode, plus the two new states

$$|e\rangle |0\rangle_{+,n} |1\rangle_{n+1} \quad |g\rangle |0\rangle_{+,n} |1\rangle_{n+1} \,. \tag{3.12}$$

States of the form $|1\rangle_{+,n} |1\rangle_{n+1}$ are higher order terms that are ignored under the assumption that $\kappa\tau \ll 1$. This gives a total of six basis states for the density operator. After performing the evolution over this time interval we trace out the nonsymmetric modes of the extended paraxial subsytem. To do this, we perform a unitary transformation on the field operators to create a new tensor product decomposition. Instead of the decomposition described in Eq. (3.10), and Eq. (3.12) consisting of the n^{th} symmetric mode $\otimes$ the $(n+1)^{\text{th}}$ coarse-grained mode, we choose symmetric and antisymmetric modes described by the annihilation operators

$$a_{\pm,n+1} = \sqrt{\frac{n}{n+1}} a_{+,n} \pm \frac{1}{\sqrt{n}} a_{n+1}. \tag{3.13}$$

The transformation which achieves this is

$$U = \begin{pmatrix} 1 & 0 & 0 \\ 0 & \sqrt{\frac{n}{n+1}} & \sqrt{\frac{1}{n+1}} \\ 0 & -\sqrt{\frac{1}{n+1}} & \sqrt{\frac{n}{n+1}} \end{pmatrix}. \tag{3.14}$$

Finally ρ_{n+1} can be obtained by tracing out the antisymmetric field mode.

The mixed state entanglement between the atom and the symmetric field mode can be calculated using Wootters formula for the tangle [94] directly from this density matrix. The results will depend on several physical parameters: the area of the beam, the intensity of the laser $|\alpha|^2$, and the duration of the pulse. Additionally, the numerical accuracy will depend upon the length of the time step used in the calculations, or equivalently the number of time steps N. To maintain the paraxial approximation, we choose the area of the beam to be $\bar{A} = A/\sigma_{\text{eff}} = 1000$. This corresponds roughly to the quadrupole transition $S_{1/2}$ to $D_{5/2}$ in $^{40}Ca^{+}$ considered by van Enk and Kimble [86], for which a laser focused to a spot size of 100 μm^2 corresponds to $\bar{A} \approx 1600$. The calculation for other parameter sets is straightforward. For simplicity we consider only $\pi/2$ pulses, such that $g\alpha\tau = \pi/2$. With the relations $\kappa = \Gamma/\bar{A}$ and $g = \sqrt{\kappa/\Delta t} = \sqrt{\kappa N/\tau}$, assuming a fixed N, we have a direct relationship between α and τ. We choose as our free parameter the emission probability, $\Gamma\tau$, which sets the degree of entanglement between the atom and laser.

A plot of the tangle versus $\Gamma\tau$ is given in Fig. 3.2. Each point in the plot corresponds to the total tangle measured just after the $\pi/2$ pulse has completely passed the atom. For very short pulses, the growth in the tangle is linear with $\Gamma\tau$ for all initial conditions, leading to a unit slope on the log-log plot. However the constant of proportionality is different. This difference can be attributed to the probability of the atom being in the excited state during the pulse interval – the more excitation the higher the rate of growth. With a greater probability of spontaneous emission, the behavior deviates strongly from this linear trend, peaking roughly where the pulse length and decoherence time are comparable. After this time the entanglement drops precipitously, and for at least one initial condition, the atom and symmetric field mode become separable. The maximum emission parameter shown in the plot is $\Gamma\tau = \sqrt{\bar{A}} = \sqrt{1000}$, which corresponds to $\kappa\tau = 1/\sqrt{\bar{A}} = 1/\sqrt{1000}$; for a larger

emission probability, our truncation of the field Hilbert space to one excitation breaks down.

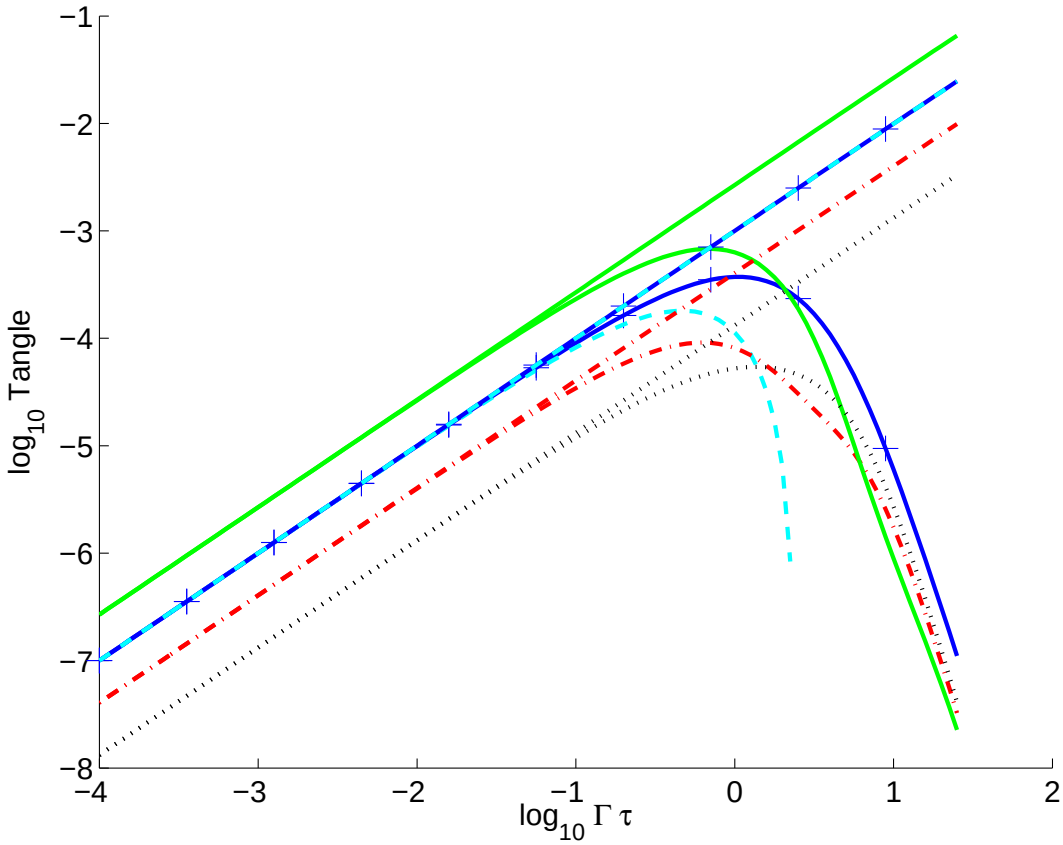

Figure 3.2: The entanglement (tangle) generated between a two-level atom and a quantized $\pi/2$ laser-pulse versus the decoherence ($\Gamma\tau$) on a log-log plot. The pulse consists of $N = 10^4$ coarse-grained modes and a normalized beam area $\bar{A} = 10^3$. Including spontaneous emission out of the beam, the tangle grows as a simple power law for $\Gamma\tau \ll 1$, then drops exponentially fast for large decoherence. Shown for comparison are the results of the tangle calculated using a closed system Jaynes-Cummings dynamic that exhibit power law behavior for all times on this plot, but agree very well with the full calculation when the probability of spontaneous emission is small. Six different initial atomic conditions are shown: $|e\rangle$ (blue, solid cross), $|g\rangle$ (green, dashed), $|e\rangle + i\,|g\rangle$ (cyan, solid), $|e\rangle - i\,|g\rangle$ (black, dotted), $|e\rangle \pm |g\rangle$ (red, dash-dot). These last two initial condition show exactly the same tangle for all times (see text).

3.3.2 Approximations

The calculation in Sec. 3.3.1 yields the entanglement between the atom and the laser mode as it propagates past the atom. It is a complex procedure because we have explicitly separated the two sources of decoherence: spontaneous emission into the nonparaxial modes and spontaneous emission into the paraxial but nonsymmetric modes. We did this because spontaneous emission into the symmetric-paraxial mode is the source of the entanglement and we must be careful not neglect this important effect. Nonetheless, emission into the nonsymmetric-paraxial modes is a small fraction of the total loss since $\kappa \ll \Gamma'$. We can consistently maintain the coherent coupling between the atom and the symmetric mode while neglecting emission into the nonsymmetric mode since it acts only as a small source a decoherence, a process dominated by off-axis emission. We thus lump all sources of decoherence together, with total rate $\Gamma = \kappa + \Gamma'$. In this case the Master equation becomes,

$$\frac{d\rho}{dt} = \frac{-i}{\hbar}[H', \rho] + \frac{\Gamma}{2}\left(2\sigma_-\rho\sigma_+ - \sigma_+\sigma_-\rho - \rho\sigma_-\sigma_+\right), \tag{3.15}$$

where $H' = -\hbar\Omega(\sigma_+ + \sigma_-)/2 - \hbar g(a\sigma_+ + a^\dagger\sigma_-)$ is the driven Jaynes-Cummings Hamiltonian. This equation describes a cavity QED dynamic plus decay into a reservoir [39]. When the evolution of the tangle is calculated using this equation of motion, the results are in complete agreement with those obtained in Sec. 3.3.1 to within numerical accuracy.

A more radical simplification is to ignore the decoherence term in Eq. (3.15) altogether when the interaction time is small compared to the atomic lifetime. The remaining dynamics represents a closed system, with the atom and the symmetric mode evolving unitarily.

$$\frac{\partial\rho}{\partial t} = \frac{-i}{\hbar}[H', \rho] \tag{3.16}$$

For this evolution, the initial bipartite pure state remains pure and the entanglement can be calculated in a straightforward manner. Such an approximation is routinely

made for atoms in cavities in the strong coupling regime, where $g \gg \Gamma$ [39]. In free space we can express g in terms of κ; the strong coupling approximation requires $\kappa \gg \Gamma^2\tau$, or equivalently $\Gamma\tau\bar{A} \ll 1$. The beam area may be chosen arbitrarily large, however, so that this inequality need not hold. One is not in the strong coupling regime in free space and so agreement between the entanglement calculated using closed and open system models should not be expected apriori. This has been the source of some recent controversy [37, 89, 30].

To compare the numerical results obtained using Eq. (3.4) with those obtained using the closed system evolution Eq. (3.16) we first calculate the tangle analytically using the closed system dynamics. Again the tangle is used as a measure of en [86], for direct comparison with our results, we use the tangle given in Eq. (3.6). A simple calculation yields,

$$T = \kappa\tau \frac{\left(2\left\langle\sigma_y\right\rangle + \pi\right)^2 + \left\langle\sigma_x\right\rangle^2\left(4-\pi^2\right)}{\pi^2} + O\left((\kappa\tau)^2\right), \tag{3.17}$$

where the Pauli matrices describe the two-level atom in the usual way. Expectation values in this equation are to be taken using the initial state of the atom. The results of this approximation are shown in Fig. 3.2. For the parameters where all approximations are valid, we see a simple linear growth of the entanglement with emission probability. Though slightly larger, the entanglement calculated via the closed system dynamics is in very good agreement, $O(\Gamma\tau)$, with our numerical results for the full atom-symmetric field mode tangle when $\Gamma\tau \ll 1$, as seen in Fig. 3.2. This agreement holds even when the system is not in the strong coupling regime, $\bar{A}\Gamma\tau > 1$.

To understand why the entanglement calculated using closed and open system dynamics agree so well even when the strong coupling assumption is violated, consider the processes which lead to the loss of entanglement. The inherent dynamics of the atom-laser mode system can be represented by a bipartite system, with subsystems A, B, coupled to a reservoir of other electromagnetic modes, R, as depicted in Fig. 3.3. System A is coupled to system B with strength κ, while it is coupled to the

reservoir R with strength Γ. System B is not coupled directly to the reservoir, coupling only indirectly through system A. The total system consisting of both subsystems A, B will start in some pure state. From the perspective of quantum trajectories [13], there are two possible ways in which the reservoir R can reduce the entanglement generated by the dynamics between A and B. In the first method the nonunitary but deterministic no-jump evolution of system A leads to a reduction of this entanglement with probability $1 - e^{-\Gamma\tau}$. The total loss of entanglement is thus proportional to $\Gamma\tau T$ for $\Gamma\tau \ll 1$, where T is the tangle generated in the closed system dynamics between A and B. Since entanglement will be generated in the closed system at a rate proportional to the coupling κ, the total loss of entanglement is of order $O(\Gamma\tau\kappa\tau)$. Alternatively, a nondeterministic jump in a quantum trajectory can reduce entanglement if it leads to a particular statistical mixture of states as described below. The probability of this particular type of correlated quantum jump is, however, limited by the smaller decoherence rate of the two subsystems A, B. In this case system B can only decay through system A in the interval τ at a rate proportional to $\Gamma\tau\kappa$. The amount of entanglement that can be destroyed through this process will then be of order $O(\Gamma\tau\kappa\tau)$. Thus both deterministic decay and quantum jumps lead to entanglement loss of order $\Gamma\tau\kappa\tau$. This is sufficiently small to ensure that the closed system dynamics generates the same entanglement as the open system dynamics when $\Gamma\tau \ll 1$ and $\kappa\tau \ll 1$, independent of the relation between them, i.e. even when the strong coupling approximation breaks down.

The above explanation can be made rigorous for the atom-symmetric field mode system. Assume that $\Gamma\tau \ll 1$ and $\kappa\tau \ll 1$, though $\bar{A}\Gamma\tau$ may be large. For $\Gamma\tau \ll 1$ the state of the system after the pulse has passed may be represented by a density operator of the form

$$\rho = (1 - \epsilon) |\psi\rangle \langle\psi| + \epsilon\rho_{\text{jump}}. \tag{3.18}$$

Here $|\psi\rangle$ is the state evolved under the closed system unitary dynamics, while ρ_{jump}

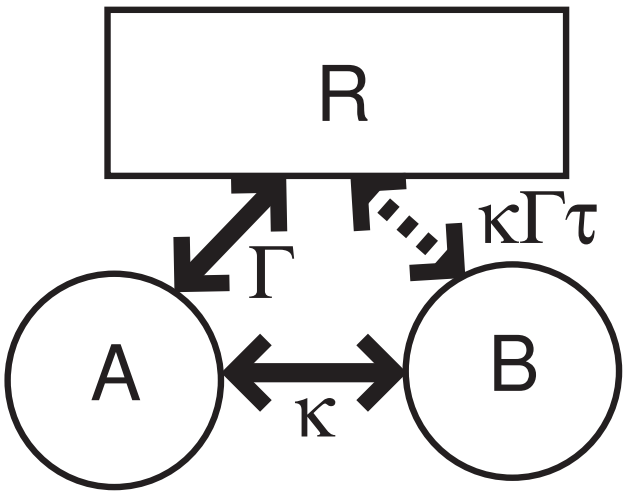

Figure 3.3: The decoherence channels for the atom-laser mode interaction are shown, with each block representing a subsystem of the entire Hilbert space. Subsystem A (the atom) is connected directly to reservoir R (all vacuum modes) with coupling rate Γ (the spontaneous emission rate). System B (the laser mode) is connected to the reservoir R only indirectly through system A. Since B couples to A at rate κ (the measurement strength), it is indirectly coupled to R at rate $\Gamma\kappa\tau$, where τ is the duration of the interaction.

represents the state conditioned on a jump having occurred during the interaction time. The probability for a jump is denoted ϵ and will be proportional to $\Gamma\tau$. These assumptions alone are insufficient to ensure that entanglement is preserved. As an example, consider the entangled state $|\psi\rangle = (1 - \xi/2)\,|g1\rangle + \sqrt{\xi}\,|e0\rangle$. This state has tangle $T \approx 4\xi$ for $\xi \ll 1$. Note that the state $|\psi\rangle$ is equivalent under local unitaries to any other state with the same entanglement. Choose,

$$\rho_{\text{jump}} = 1/2\,|e1\rangle\langle e1| + 1/2\,|g0\rangle\langle g0|\,, \tag{3.19}$$

then the statistical mixture ρ given in Eq. (3.18) is separable for $\sqrt{\xi} \leq \epsilon$, as can be seen by its positive partial transpose [55, 36]. For our particular case of an atom in free space $\sqrt{\xi} \leq g\tau$, since entanglement is generated by the atom-field coupling. So for this choice of ρ_{jump}, the system can be made separable when $g < \Gamma$, or equivalently

$\bar{A}\Gamma\tau > 1$.

Since our calculations shows that the open system maintains the same entanglement as the closed system, even when $\bar{A}\Gamma\tau > 1$, the dynamics must be restricted such that these special statistical mixtures are rare. To see this, note that the post-jump state we considered above must be generated by a highly correlated jump process. The probability of such a process is very low. Indeed, to good approximation, we expect ρ_{jump} to be of the form

$$\rho_{\text{jump}} = \rho_{\text{atom}} \otimes |\text{vac}\rangle \langle\text{vac}| \tag{3.20}$$

where ρ_{atom} is some arbitrary (possibly mixed) state of the atomic subsystem. This ignores the process of spontaneous emission into a nonparaxial mode followed by subsequent excitation of a paraxial mode. This higher order process may be safely ignored when we are considering entanglement of order $\kappa\tau$, and $\sqrt{\kappa\tau} \gg \kappa\tau\Gamma\tau$, which is satisfied when $\Gamma\tau \ll 1$. Inserting Eq. (3.20) into Eq. (3.18) the tangle may then be calculated using Wootters' formula, assuming that $|\psi\rangle$ is an arbitrary state that can be generated using the closed system dynamic. To lowest order, $O(\kappa\tau\Gamma\tau)$, this agrees with the tangle obtained using closed system dynamics.

3.3.3 Bounding the Total Entanglement

We now consider the entanglement that is generated between the atom and all paraxial modes. This is the physically relevant quantity that determines the error rate in atom-laser control, modulo spontaneous emission into the nonparaxial modes. In addition, it gives a measure of the dynamically generated entanglement resource that is accessible in principle. A calculation of this total entanglement is significantly more complex than the calculation performed in Sec. 3.3.1 as the Hilbert space associated with all coarse-grained paraxial modes is much larger than that of the single symmetric mode. Even if we assume $\kappa\tau \ll 1$, and thereby restrict paraxial field modes

to a single excitation as in Sec. 3.3.1, the remaining Hilbert space has dimension $2 \otimes (N+1)$. A calculable measure of entanglement for a mixed state of a $2 \otimes N$ system for $N > 2$ is not known except for some special cases which do not apply here [58, 90]. We thus resort to calculating a bound for the total entanglement, using the tangle as our measure.

The general difficulty with calculating the entanglement of a mixed state arises because the ensemble decomposition of a density operator into a statistical mixture of pure states $\rho = \sum_i p_i |\psi_i\rangle \langle\psi_i|$ is not unique. Averages of a pure state entanglement monotone for different ensemble decompositions do not usually lead to the same result and one must thus perform a difficult minimization search to find the actual entanglement. Since the tangle is a convex function, however, any ensemble decomposition provides an upper bound according to,

$$T(\rho) \leq \sum_i p_i T\left(|\psi_i\rangle \langle\psi_i|\right) \quad \forall\{\psi_i, p_i : \rho = \sum_i p_i |\psi_i\rangle \langle\psi_i|\} \tag{3.21}$$

Given a known ensemble decomposition, we can calculate the right hand side by averaging the tangle for the given bipartite pure states, over the appropriate probability distribution, using Eq. (3.6).

A natural ensemble decomposition is obtained by integrating the master equation of the atom-paraxial system using the quantum trajectory method [13]. A stochastic Schrödinger equation describes the evolution of an open quantum system with nonunitary evolution due to its coupling to the environment, and conditioned on a fictitious measurement performed on the environment with unit efficiency. For each measurement record $M(t)$ there is a corresponding pure state trajectory $|\psi_M(t)\rangle$. Averaging over the all possible measurement records results in a mixed state description, with density operator given by the convex combination

$$\rho(t) = \sum_M p_M(t) |\psi_M(t)\rangle \langle\psi_M(t)| . \tag{3.22}$$

From this construction one may immediately write down an upper bound on the tangle using Eq. (3.21).

Brute force calculation of all the required trajectories is straight forward but prohibitive. If we choose the fictitious measurement to be photodetection, a measurement record will consist a sequence of bits denoting count/no-count decisions in each interval $(t, t + \Delta t)$ (ignoring the possibility of two or more photodetections as it is of order δt^2). Assuming there are $N = 1000$ such intervals then there are 2^{1000} trajectories. Our calculation is made tractable, however, by noting that only the modes after the most recent jump in any trajectory will contribute to the tangle; the state of any field modes which passed the atom prior to the last jump will not be entangled with the atom since the post-jump state is separable (the atom in the ground state and the field in a coherent state). The evolution after a jump has occurred will be independent of when the jump occurred as the system is Markov, and all of the quantized paraxial modes prior to interaction with the atom are in the same coherent state. It is thus sufficient to calculate two no-jump trajectories – the initial trajectory $|\psi_A(i)\rangle$ and the post-jump trajectory $|\psi_B(i)\rangle$. Both represent deterministic evolution according to a nonHermitian Hamiltonian, including the coupling of the system to the nonparaxial modes assuming *no quantum jumps* into the nonparaxial modes. They differ only in their initial conditions: $|\psi_A(i)\rangle$ is the evolution given the initial state of the atom at $t = 0$ and $|\psi_B(i)\rangle$ is the evolution starting with the atom in the ground state right after a jump. An upper bound on the tangle then follows from Eq. (3.21),

$$T(\rho) \leq \sum_{1=1}^{N} P_{LJ}(i) T_{PJ}(N - i) + P_{NJ} T_{NJ}, \tag{3.23}$$

where $P_{LJ}(i)$ and P_{NJ} are respectively the probability that the last jump occurred during the time interval i and the probability that no jump occurred during the entire evolution. The tangle associated with no jumps during any interval follows from Eq. (3.6), $T_{NJ} = T\left(|\psi_A(N)\rangle\right)$, whereas the post-jump tangle is given by $T_{PJ}(N - i) =$

$T\left(|\psi_B(N-i)\rangle\right)$.

The relevant probabilities that appear in Eq. (3.23) may also be calculated using the fiducial trajectories. In particular under nonunitary evolution without normalization, the probability that no jump occurs in a given trajectory up to time t is $\|\tilde{\psi}(t)\|^2$. Thus, the probability that no jump occurs during any of the N intervals is $P_{NJ} = \|\tilde{\psi}_A(N)\|^2$. The probability that the last jump occurred in interval i is given by,

$$P_{\mathrm{LJ}}(i) = P_{NJ}(N|i)P_J(i), \tag{3.24}$$

where $P_{NJ}(N|i) = \|\tilde{\psi}_B(N-i)\|^2$ is the conditional probability that no jumps occur between the interval i and N given that a jump occurred in interval i. The total probability that a jump occurred at time step i, $P_J(i)$, will satisfy the following equations:

$$P_J(i) = P_A(i) + \sum_j P_J(i|j)P_A(j), \tag{3.25a}$$

$$P_J(i|j) = P_B(i-j) + \sum_{k>j} P_J(i|k)P_B(k-j). \tag{3.25b}$$

The first equation expresses the total probability for a jump in interval i as the sum of the probability that the system had its first jump in interval i, $P_A(i)$, plus the probability that it first jumped in interval $j < i$ then some time later jumped in interval i. $P_J(i|j)$ is thus the conditional probability for a jump at i given a previous jump occurred in interval j. Eq. (3.25b) provides a recursive relation for $P_J(i|j)$ in terms of, $P_B(i-j)$, the probability for a jump to occur $i-j$ intervals after a previous jump occurred, with no intervening jumps. The probability $P_A(i)$ can be easily calculated from the fiducial trajectory $|\psi_A(i)\rangle$ and similarly $P_B(i-j)$ can be calculated from $|\psi_B(i-j)\rangle$ [13]. Since $P_J(i|j)$ is only a function of $i-j$, as follows from the Markov property, the recursion relation (Eq. 3.25b) can be solved independently. We find a suitable solution by truncating the recursion at n steps

corresponding to at most $n+1$ jumps into the nonparaxial modes. Solving for $P_{LJ}(i)$, using this truncated solution, we can then obtain an upper bound on the tangle according to Eq. (3.23).

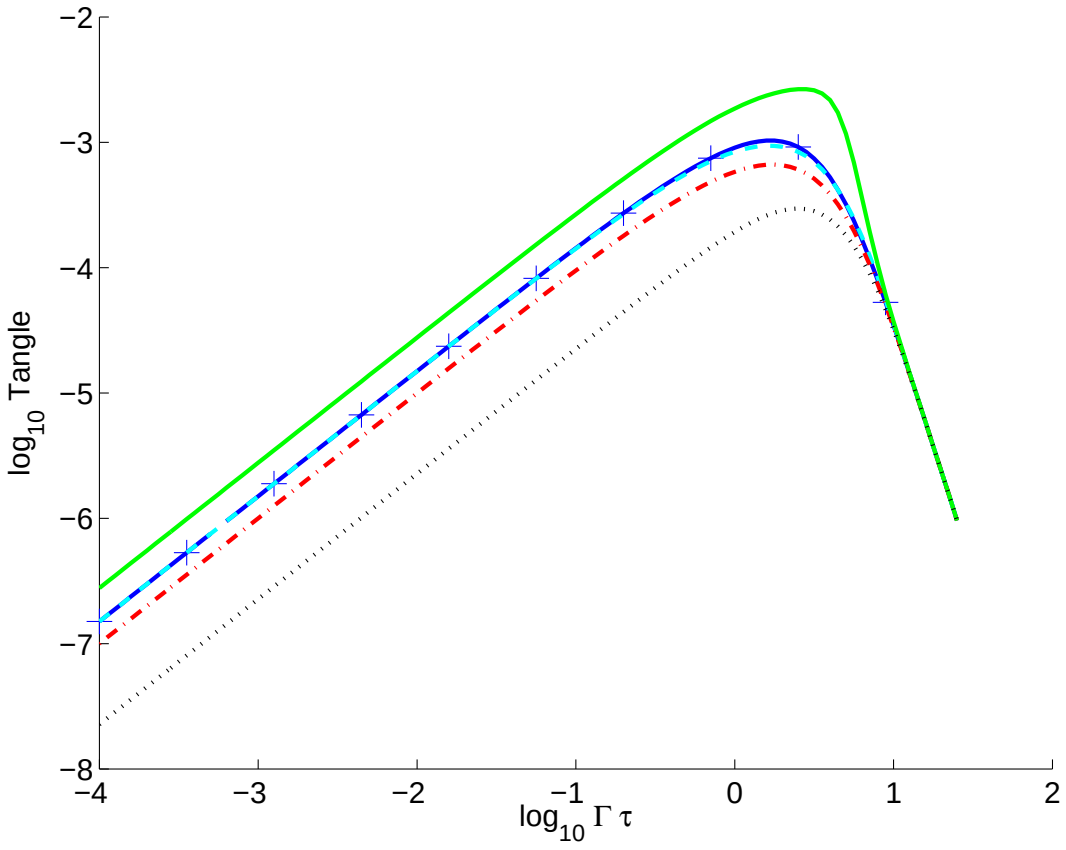

Figure 3.4: An upper bound on the the entanglement (tangle) generated between the atom and all coarse-grained paraxial field modes is plotted versus the total decoherence ($\Gamma\tau$) in a log-log plot. The different curves represent different atomic initial conditions with parameters given in Fig. 3.2

The code for performing these calculations is given in Appendix A. The resulting upper bound on the tangle is plotted in Fig. 3.4 as a function of time. For short times, linear behavior is exhibited, as in the previous calculations for the symmetric tangle. Note, however, that the rate of entanglement generation is always greater

than the symmetric calculation. For short pulse durations $\Gamma\tau \leq 10^{-2}$ there is only a 5% difference in rates for the initial condition $|g\rangle + i\,|e\rangle$, the state that is most excited during the interval. Of course the previous calculation places a lower bound on the full entanglement of all the paraxial modes, as it is the exact amount of entanglement between the atom and a subset of these modes (specifically the one symmetric mode). All of the plotted upper bounds turn over at roughly the same point, slightly past where the pulse duration equals the decoherence time, and then converge on a single limit for large decoherence probability. This behavior is to be expected as for long times all information about the initial state will be lost to the environment.

3.4 Summary

Entanglement is generated between a laser beam and an atom in free space due to the atom's spontaneous emission of photons into the paraxial modes, superimposed on the laser's coherent field amplitude. Through the use of judicious approximations, we were able to quantify this entanglement, a fundamentally hard problem for a large dimensional open quantum system. In particular we calculated the entanglement between the atom and the field mode defined by the laser pulse. Of particular interest is how our measure of entanglement is reproduced under further simplifying assumptions. We considered two models: a lumped decoherence model and a closed-system model. In the former all sources of decoherence, paraxial and nonparaxial, are lumped into a single decoherence term. This is in excellent agreement with the full calculation when the paraxial approximation holds, $\bar{A} \gg 1$. This is as expected, since the vast majority of the decoherence is due to the nonparaxial modes. More surprisingly, a closed system model which treats the quantized atom laser-pulse dynamics via a single mode Jaynes-Cummings Hamiltonian is in excellent

agreement when $\Gamma\tau \ll 1$, even when the strong coupling assumption was violated. This result was surprising since the naive picture would argue that, in the absence of the strong atom-mode coupling, $\bar{A}\Gamma\tau > 1$, spontaneous emission into other modes should destroy entanglement. We have shown, however, that the particular form of the coupling between the vacuum modes and the atom-laser system in fact preserves the entanglement. Thus, there is no contradiction between the observation that all quantum effects in the atom-laser interaction are due to spontaneous emission [37] and the fact that atom-laser entanglement can be accurately modeled using a single mode Jaynes-Cummings dynamic [86, 29] when $\Gamma\tau \ll 1$. Such agreement is ensured by the fact that spontaneous emission is the *only* decoherence mechanism.

Finally, we placed an upper bound on the total entanglement that is generated between the atom and the full set of paraxial field modes. We used the quantum trajectory method to calculate a dynamical unravelling of the master equation, which provides a natural ensemble decomposition of the bipartite density matrix. Averaging the pure state tangle over this ensemble leads to an easily calculated upper bound. It remains to be seen how tight this bound is. Nonetheless, it provides a useful benchmark on the total entanglement resource that is available for quantum information processing applications.

Chapter 4

Dynamics of an alkali atom

In the last two chapters we have explicitly considered very simple atomic systems. Either having only two total levels, as in Chap. 3, or having a single doubly degenerate ground state, Sec. 2.3. In either case the meaningful dynamics took place within a two level submanifold of the entire atomic system. The dynamics associated with such a two level system are severely restricted. In fact simple rotations are sufficient to describe any unitary dynamic on the system. To expand beyond such a limited system we now consider the dynamics of a single hyperfine ground state of an alkali atom with arbitrary total angular momentum.

An alkali atom with nonzero nuclear angular momentum $I \neq 0$ has at least one hyperfine ground state manifold with total angular momentum $F > 1/2$ containing $2F + 1 > 2$ magnetic sublevels. These extra levels will allow us to explore the full tensor nature of the light shift operator

$$H = -\frac{1}{4}\mathbf{E}^* \cdot \overleftrightarrow{\alpha} \cdot \mathbf{E}. \tag{4.1}$$

The richer structure allows us to ask questions about quantum control in a nontrivial setting [**?**]. These include questions about how to perform optimal quantum state preparation [**?**] and how to implement full unitary control, exploring algorithms and

techniques that could be applied to a vast array of systems [**?**]. Questions of quantum chaos, and classical correspondence can initially be addressed when the number of levels is on the order of 10. This level is achieved in some atomic systems, such as in the $F = 4$ ground state of ^{133}Cs with 9 total levels. The additional structure also allows for some other interesting interactions, such as microwave and radio frequency controls. Such extended control possibilities, though not discussed in this dissertation, provide possible avenues for extending the work discussed in Chap. 5.

In addition to their rich ground state structure alkali atoms have two other important benefits. Atomic spins in electronic ground states are robust, coherent, and controllable, allowing for ready experimental exploitation. There is a bountiful literature on the trapping and cooling of neutral alkali atoms [**?**], the optical pumping of such atoms [**?**], and the manipulation of their internal state [**?**]. Such a well studied system presents the possibility for theoretical constructions to be brought into a laboratory and experimentally tested against a real world system. Complementing this property is the ability to observe the atomic dynamics through off resonant atomic spectroscopy. The ability to perform spectroscopy on the atoms allows direct comparison of experiment to theory, as is done in Sec. 4.5. It also makes possible the tomographic procedure discussed in Chap. 5. In addition to its relevance to this dissertation the ability of spectroscopy to perform real time observation of atomic spins is currently being pursued in numerous laboratories based on polarization spectroscopy of a laser probe [**?**]. The long history of magneto-optical coherent spectroscopy studied in, for example, optical pumping[**?**], the Faraday effect[**?**], and coherent population trapping[**?**] provides a solid foundation upon which a modern laboratory of quantum measurement can be built. Proof of principle experiments have already been demonstrated, such as continuous observation of nonlinear spin dynamics[**?**], production of spin-squeezed states[**?**], and the generation of macroscopically separated atomic spin ensembles[**?**]. The real time nature of the spectroscopic probe also opens up the possibility of real time feedback, examples of which have

been realized in some recent experiments [**?**].

The nominal experimental setup we consider here consists of a large number of ultracold alkali atoms coupled to the same laser probe, as described in the introduction Sec. 1.4. Such a system can generally support quantum states which are entangled across the whole ensemble, and manipulation of such states is being actively pursued by many groups [**?**]. In this chapter the main concern, however, is the evolution and measurement of the state of individual atoms interacting with the laser probe. The ensemble of atoms then allows us to extract information about the atomic state of the evolving identically prepared atoms without perturbing the evolution of any individual atom. We thus assume that we are operating in the weak measurement regime where shot noise of the probe dominates the projection noise due to the ensemble measurement, allowing us to neglect backaction. In the strong measurement regime where projection noise dominates shot noise one expects spin squeezing to occur, as is seen in some recent experiments [**?**].

This chapter is organized as follows. Sec. 4.1 reviews the process of adiabatic elimination which reduces the dynamics to the ground state manifold. The results of this section form the basis for the simulation code which is exhibited in Appendix B and used extensively in Sec. 4.5 and Chap. 5. Sec. 4.2 is a digression on the transfer of coherences during the process of adiabatic elimination, which determines whether superpositions are preserved by a specific decay channel. Sec. 4.2.1 gives a nontrivial example of how one appropriately treats the transfer of coherences when eliminating a ground state manifold. Sec. 4.3 discusses a tensor decomposition of the Hamiltonian which proves useful for examining the dynamics and measurement of the atomic system. Sec. 4.4 explores the possibility for control of alkali atoms by leveraging off of his tensor decomposition. Sec. 4.5 presents a comparison of simulated dynamics with experimental results. Sec. 4.6 summarizes the pertinent results.

4.1 Adiabatic elimination

In this chapter we consider the dynamics and measurement associated with a laser probe interacting with a single atomic transition of an alkali atom, e.g. the D2, $S_{1/2}$ ground state manifold to a $P_{3/2}$ excited state manifold (e). We further restrict the probe to interact with only one ground state hyperfine level, denoted g, with total angular momentum F_g. The probe is, however, permitted to excite the atom to any of the possible hyperfine states within the excited manifold e. Extension to more levels is straightforward but cumbersome.

We use projectors onto the excited states P_{eF}, and ground state P_g, as well as $P_e = \sum_F P_{eF}$, the projector onto the full excited state manifold. Detunings are measured from the grounds state $\Delta_{eF} = E_{eF} - E_g$. Finally sub-blocks of the density matrix are denoted,

$$\rho_{a,b} = P_a \rho P_b. \tag{4.2}$$

with $a, b \in g, eF$.

As before the basic laser-atom interaction we consider is the electric dipole interaction,

$$H_{\text{int}} = -\mathbf{d} \cdot \mathbf{E}. \tag{4.3}$$

Making the rotating wave and Markov approximations, we recover the standard master equation in the rotating frame

$$\frac{d}{dt}\rho = \frac{i}{\hbar}\left[H_{\text{atom}} + H_{\text{int}}, \rho\right] + \mathcal{L}_{\text{spont}}\left(\rho\right). \tag{4.4}$$

The unperturbed atomic Hamiltonian is

$$H_{\text{atom}} = \sum_F \Delta_{eF} P_{eF}. \tag{4.5}$$

The interaction Hamiltonian in terms of the dipole operator $\mathbf{d}_{ge} = \mathbf{d}_{eg}^{\dagger} = P_g \mathbf{d} P_e$, is,

$$H_{\text{int}} = \frac{1}{2}\left[\mathbf{E}_L \cdot \mathbf{d}_{ge} + \mathbf{E}_L^* \cdot \mathbf{d}_{eg}\right]. \tag{4.6}$$

with the electric field as the real part of$\mathbf{E}_L e^{-i\omega_L t}$. $\mathcal{L}_{\text{spont}}$ is the set of Linblad terms corresponding to spontaneous emission. In terms of the jump operators

$$D_q = \epsilon_q \cdot \mathbf{d}_{ge}, \tag{4.7}$$

we have

$$\mathcal{L}_{\text{spont}}(\rho) = \sum_q \left[D_q \rho D_q^{\dagger} - \frac{1}{2}\left\{ D_q^{\dagger} D_q, \rho \right\} \right]. \tag{4.8}$$

To eliminate the excited states we follow the adiabatic elimination procedures described in [**?**]. Begin with master equation (Eq. 4.4), and assume that the ground state $\rho_{g,g}$ changes slowly compared to both the excited state $\rho_{e,e}$, and the ground excited coherences $\rho_{e,g}$. Coarse graining over the fast time scale we seek to solve for $\rho_{e,e}, \rho_{e,g}$ in terms of $\rho_{g,g}$. The evolution of excited to ground coherences is

$$\frac{d}{dt}\rho_{e,g} = -\sum_F \left(\frac{\Gamma}{2} - i\Delta_{eF} \right) \rho_{eF,g} + \frac{i}{2\hbar} \mathbf{E}_L^* \cdot \left(\mathbf{d}_{eg}\rho_{g,g} - \rho_{e,e}\mathbf{d}_{eg} \right). \tag{4.9}$$

Upon coarse graining over time scales $\Delta t \gg 1/\Gamma$ we can ignore the term $\dot{\rho}_{e,g}$ as $\frac{\Gamma}{2}\rho_{e,g}$ will dominate. Additionally $\rho_{e,e}$ can be safely ignored as the population in the excited state will be small. Solving for $\rho_{e,g}$.

$$\rho_{eF,g} = \frac{-i}{\frac{\Gamma}{2} - i\Delta_{eF}} \frac{1}{2\hbar} P_{eF} (\mathbf{E}_L^* \cdot \mathbf{d}_{eg}) \rho_{g,g} P_g. \tag{4.10}$$

Substitute this back into the ground state evolution. The reduced evolution is

$$\frac{d}{dt}\rho_{gg} = \frac{i}{4\hbar} \sum_{ij} E_{Li}^* E_{Lj} \left[\alpha_{ij}\rho_{gg} - \rho_{gg}\alpha_{ji}^{\dagger} \right] + \sum_q D_q \rho_{ee} D_q^{\dagger}. \tag{4.11}$$

with the complex polarizability tensor operator $\overleftrightarrow{\alpha}$ defined as

$$\alpha_{ij} = \sum_F \frac{\mathbf{e}_i \cdot \mathbf{d}_{ge} P_F \mathbf{e}_j \cdot \mathbf{d}_{eg}}{\Delta_F + i\frac{\Gamma}{2}}. \tag{4.12}$$

Note that the last term in Eq. (4.11) only depends on ρ_{ee} as one would expect since only the excited state can decay. One then solves for ρ_{ee} in terms of ρ_{gg}, to get,

$$\rho_{e,e} = \frac{1}{2\hbar}\sum_{F,F'}\frac{1}{\Gamma - i(\Delta_F - \Delta_F)}\times \left(\frac{1}{\Gamma/2 + i(\Delta_F)} + \frac{1}{\Gamma/2 - i(\Delta'_F)}\right) P_F \mathbf{E}^*_L \cdot \mathbf{d}_{eg}\rho_{g,g}\mathbf{d}_{ge}\cdot\mathbf{E}_L P_{F'}. \quad (4.13)$$

Substituting this in to Eq. (4.11) then provides an evolution equation which acts solely upon the ground state.

4.2 Transfer of coherences

This section considers the general question of transfer of coherences in dissipative systems. A transfer of coherences can occur when there is a coherent superposition of at least two decaying magnetic sublevels, $|\psi\rangle = a|1\rangle + b|2\rangle$. This state can decay to give $|\psi\rangle' = a|1'\rangle + b|2'\rangle$, maintaining the initial superposition during the decay process. In this example we would say that the coherences were transfered. The transfer of coherences can be destroyed if the environment extracts information about the initial system state. For example if the environment provides a record of whether the system decayed from state 1 or state 2 then the post decay state will be $\rho = |a|^2|1\rangle\langle 1| + |b|^2|2\rangle\langle 2|$.

The question of which coherences are transfered and which are not is an interesting question of basic physics. In particular questions about coherence transfer arise naturally when one asks the difference between elastic and inelastic scattering in a quantum setting. The classical concept of elastic scattering corresponds to coherences between excited states with differing total angular momentum being transfered during the scattering process, which only occurs for far off resonant excitations. Additionally the more coherences that are transfered the more slowly the

atom will decohere due to its slower rate of information transfer to the environment. Thus keeping careful track of the transfer of coherences is necessary in any application that wishes to exploit atomic coherence or extract information from an atomic sample, such as we consider in Chap. 5.

We consider two possible mechanisms that result in coherences not transferring, intrinsically incoherent processes and temporally incoherent processes. An intrinsically incoherent process exists when detection of the environment at a single instant of time is sufficient to determine which channel the system decayed through. For example processes which are distinguished by the polarization of the emitted light $q = -1, 0, 1$. Temporal incoherence occurs when one considers detecting the environment over some finite interval Δt. By detecting the energy emitted during the decoherence process one can distinguish several incoherent channels to an accuracy $\Delta E \approx \hbar/\Delta t$. Intrinsically incoherent processes are easy to identify and account for using standard techniques [**?**]. Complications arise when one attempts to identify and account for temporally incoherent processes, because the system dynamics alter the temporal coherence properties as the Hamiltonian interactions induce energy level shifts. We now consider how one should account for the effect of these level shifts on the decay terms.

We begin by rederiving the master equation for a simple atomic system labeling the magnetic sublevels of the ground state by$m$. We assume a Hamiltonian diagonal in the z basis such that each value of m is associated with an energy E_m. Again, in the dipole and rotating wave approximations we have

$$H_{\rm int}^{(I)} = i\hbar \sum_{\mathbf{k},\lambda,m,q} e^{-i(\omega_k - \omega_A + \delta\omega_m)t} g_k a_{\mathbf{k},\lambda} D_{m,q}^{\dagger} \epsilon_{\mathbf{k},\lambda} \cdot \mathbf{e}_q^* + \text{h.c.}. \tag{4.14}$$

Here g_k is the free space coupling, $\hbar\omega_A$ and $\hbar\delta\omega_m$ the excited state energy splitting and ground state energy splittings from the reference ground state level, $\hbar\omega_k$ the field frequency, $a_{\mathbf{k},\lambda}$ the field annihilation operator for a specific wave vector and polarization and $D_{m,q}$ the projection of the dipole operator connecting excited state

$|e, m+q\rangle$ with ground state $|g, m\rangle$. Also we have $\mathbf{e}_q$ and $\epsilon_{\mathbf{k},\lambda}$ as the unit vectors for the dipole with definite angular momentum, and for the polarizations of the electric field respectively. Now we may expand the time evolution of the density operator ρ using the above Hamiltonian recovering a standard Linblad master equation

$$\frac{d}{dt}\rho = -\sum_{m,q,m',q'} \Gamma_{m,q,m',q'} \left[\frac{1}{2}\left\{D^\dagger_{m,q} D_{m',q'}, \rho\right\} - D_{m',q'}\rho D^\dagger_{m,q}\right] \tag{4.15}$$

in which $D_{m,q}$ are now the Linblad jump operators associated with decay into the ground state m with angular momentum loss q. The decay rates $\Gamma_{m,q,m',q'}$ are given by

$$\Gamma_{m,q,m',q'} = \sum_{\mathbf{k}} \frac{1}{\Delta t} f_m(\omega_k) f^*_{m'}(\omega_k) |g_k|^2 \sum_\lambda \mathbf{e}_q \cdot \epsilon^*_{\mathbf{k},\lambda} \epsilon_{\mathbf{k},\lambda} \cdot \mathbf{e}_{q'}, \tag{4.16}$$

with

$$f_m(\omega) = \int_t^{t+\Delta t} dt'\, e^{-i(\omega-\omega_A+\delta\omega_m)t'}. \tag{4.17}$$

The above assumes a coarse graining time Δt. Using the Markov approximation and performing all of the requisite integrals we can reduce the expression for the coherences to

$$\Gamma_{m,q,m',q'} \approx \delta_{qq'}\Gamma e^{-i(\delta\omega_m - \delta\omega_{m'})t} \tag{4.18}$$

with Γ the standard excited state linewidth. This expression valid under the Markov approximation, when particular $\Delta t \ll 1/\Gamma, 1/\omega_A$. We also require the ground state splitting to be small compared to the energy gap from the excited state $\delta\omega_m \ll \omega_A$ which assumption almost always holds in current experiments. Note that the intrinsically incoherent processes due to are decohered by the delta function $\delta_{q,q'}$ as expected.

The dependence of the decay rates $\Gamma_{m,q,m',q'}$ on the energy splitting in the ground state accounts for the temporal incoherence. There is a smooth transition from

complete coherence over short times to complete incoherence for long integration. We see this by noting that when $\delta\omega_m \Delta t << 1 \ \forall m$ we recover

$$D_q \equiv \sum_m D_{q,m} \tag{4.19}$$

and the transfer of coherences is preserved. The alternate extreme has $\delta\omega_m \Delta t >> 1 \ \forall m$ giving

$$\Gamma_{m,q',m,q} = \delta_{q,q'}\delta_{m,m'}. \tag{4.20}$$

This causes all decay processes terminating in distinct m states to be temporally incoherent.

Starting with Eq. (4.18) one may transform back to the Schrödinger picture. The jump operators transform as

$$D_{m,q} \rightarrow D_{m,q} e^{i(\omega - \delta\omega_m)t}. \tag{4.21}$$

This transformation exactly cancels the phases in Eq. (4.18) when inserted into Eq. (4.15). Thus the full master equation in the Schrödinger picture becomes

$$\dot{\rho} = \frac{-i}{\hbar}[H_A, \rho] - \frac{\Gamma}{2}\sum_q \left[\left\{D_q^\dagger D_q, \rho\right\} - 2D_q \rho D_q^\dagger\right]. \tag{4.22}$$

When this equation is integrated it will naturally account for any necessary temporal incoherence.

Thus inclusion of the full Hamiltonian dynamics treats the transfer of coherences appropriately. An interesting question is whether one can partially remove the systems dynamics of an eliminated level by including decoherence terms to account for the loss of coherences, which we explore in Sec. 4.2.1.

4.2.1 Ground state elimination

We now consider how to treat population which has decayed out of the system, into a nonprobed ground state hyperfine level. The most obvious method is to treat this

term as loss. Since the atoms in the nonprobed levels do not further affect the system dynamics or measurement they can be ignored. To account for this mathematically one just leaves these terms out of the master equation, leading to a decrease in the trace of the density operator. This is what was done in Sec. 4.1. This procedure is used to model an experiment in Sec. 4.5 with good results.

Alternatively one can consider pumping any stray excitations in the nonprobed ground state back into the system on a fast timescale. While this procedure is not used in the sequel it provides an interesting example of an alternative dynamic. In this procedure a repumper strongly couples the nonprobed states to some excited state, inducing a fast decay of the errant excitation. Such fast decay should allow for these states to be adiabatically eliminated just as the excited states were in Sec. 4.1.

We wish to find a superoperator [**?**] $\mathcal{R}$ which maps excitations from the eliminated states back to the manifold of interest. Then any terms in the master equation which result in decay into the eliminated states can be encapsulated by $\mathcal{R}$ which transfers the excitations back to the single remaining hyperfine level in a way consistent with the repumper dynamics. We assume a trace preserving $\mathcal{R}$, such that $\mathrm{Tr}\left[\mathcal{R}(A)\right] = \mathrm{Tr}\left[A\right] \forall A$, corresponding to the assumption that no excitations are lost during the repumping process.

Labeling the unprobed ground state g' we can write the full master equation for the ground state of interest as,

$$\frac{d}{dt}\rho_{g,g} = \frac{i}{\hbar}\left[H_{\mathrm{LS}}, \rho_{gg}\right] - \mathcal{D}(\rho_{g,g}) + \mathcal{F}_g(\rho_{gg}) + \mathcal{R}\left(\mathcal{F}_{g'}(\rho_{gg})\right). \tag{4.23}$$

where $\mathcal{D}$ accounts for the decay out of the state g, while $\mathcal{F}_a$ denotes the feeding terms that replace the decayed excitations into level a. In the simple example described in the introduction $\mathcal{D}(\rho) = \frac{\Gamma}{2}\left\{\sigma_+\sigma_-, \rho\right\}$, while $\mathcal{F}_g(\rho) = \Gamma\sigma_-\rho\sigma_+$. Note that the trace preserving property of decay implies that $\mathrm{Tr}\left[\mathcal{D}(\rho)\right] = \mathrm{Tr}\left[[\mathcal{F}_g + \mathcal{F}_{g'}](\rho)\right]$.

To find a form for the repumping superoperator $\mathcal{R}$ for this example we must consider the basic physical processes leading to the excitation and decay. To begin imagine that all population in the state g' is instantaneously pumped into the excited state. Subsequent to the excitation the spontaneous emission will decay the atom back to the ground state. The total process consisting of excitation from the ground state g' and decays into some ground state a will be denoted by the superoperator $\mathcal{J}_a$. An equation for the repumping superoperator $\mathcal{R}$ then has the following form

$$\mathcal{R}(\rho) = \mathcal{J}_g(\rho) + \mathcal{R}\left(\mathcal{J}_{g'}(\rho)\right). \tag{4.24}$$

In words the repumping process consists of exciting the system and letting it decay, if that decay returns the system to g halt, otherwise repump until it lands in manifold g. Eq. (4.24) can be formally solved with

$$\mathcal{R}(\rho) = \mathcal{D}_0[\left([\mathcal{I} - \mathcal{J}_{g'}]^{-1}(\rho)\right). \tag{4.25}$$

Here $\mathcal{I}$ is the superoperator identity. Since superoperators are all linear operations both addition and inversion are simple matrix manipulations. The repumper maps excitations from the state g' to the state g as promised, and is trace preserving, assuming that the basic processes $\mathcal{J}_a$ are.

The above procedure assumes an instantaneous repumping process which is unphysical. The effect of allowing the repumper to act over a finite time is to introduce temporal incoherence. To account for this we introduce a superoperator $\mathcal{C}$, which acts to appropriately decohere the system after each jump in the repumping process. Eq. (4.24) becomes

$$\mathcal{R}(\rho) = \mathcal{J}_g\mathcal{C}(\rho) + \mathcal{R}\left(\mathcal{J}_{g'}\mathcal{C}(\rho)\right). \tag{4.26}$$

which has solution

$$\mathcal{R}(\rho) = \mathcal{J}_g\left(\mathcal{C}\left[\mathcal{I} - \mathcal{J}_{g'} * \mathcal{C}\right]^{-1}(\rho)\right)\right). \tag{4.27}$$

To find $\mathcal{C}$ we consider a physical repumping process that excites the state $|g, m\rangle$ to some specific excited state $|e, m\rangle$. The excitation is driven by a standard Rabi Hamiltonian with rabi frequency Ω_m, which depends on the atomic state through the appropriate Clebsch-Gordan coefficient. Note that the choice of quantization axis specifies the basis in which the repumper acts. The evolution of the state under the Rabi Hamiltonian is given by

$$|\psi_m(t)\rangle = \exp\left[\begin{pmatrix} 0 & -i\Omega_m \\ -i\Omega_m & 0 \end{pmatrix} t\right] |F_1, m\rangle \,. \tag{4.28}$$

To account for the jumps we make use of an unravelling of the master equation [**?**] in which the Linblad operators correspond to jumps at a specific time. In this unravelling the action of the nonunitary nojump evolution operator on the two dimensional subspace spanned by these states is

$$|\psi_m(t)\rangle = \exp\left[\begin{pmatrix} -\Gamma/2 & -i\Omega_m \\ -i\Omega_m & 0 \end{pmatrix} t\right] |F_1, m\rangle \tag{4.29}$$

The state dependent probability that a jump occurs at time t is then

$$p_m(t) = \Gamma dt |\langle F', m+q|\psi_m(t)\rangle|^2, \tag{4.30}$$

while the jump operators for this unravelling are

$$J_m(t) = \sqrt{\Gamma dt}\,\langle F', m+q|\psi_m(t)\rangle\, P_m \sim \sqrt{p_m(t)} P_m. \tag{4.31}$$

Note that these operators are diagonal in the m basis. Hence their only effect is to decohere the different m's according to when a jump occurred. $\mathcal{C}$ may now be written as

$$\mathcal{C}(\rho) = \sum_{m,m'} \int dt\ J_m(t) \rho J_{m'}(t). \tag{4.32}$$

Jumps that occur at the same time will retain coherences between the m's while jumps at different times result in a loss of the coherences. The integral will generally

run over the coarse graining time. Assuming that the repumping process occurs quickly we can extend the integral without changing the result to get

$$\mathcal{C}(\rho) = \sum_{m,m'} A_{m,m'} P_m \rho P_{m'}. \tag{4.33}$$

with

$$\begin{aligned} A_{m,m'} &= \Gamma \int_0^\infty dt \, \langle F', m+q|\psi_m(t)\rangle \, \langle \psi_{m'}(t)|F', m+q\rangle \,, \\ &= \frac{\Omega_m \Omega_{m'} \Gamma^2}{(\Omega_m^2 - \Omega_{m'}^2)^2 + \frac{\Gamma^2}{2}(\Omega_m^2 + \Omega_{m'}^2)}. \end{aligned} \tag{4.34}$$

Note that $A_{m,m} = 1$ and $A_{m,m'} \leq 1$ as expected. Inserting these amplitudes into Eq. (4.33) provides an explicit formula for $\mathcal{C}$ which is then inserted into (Eq. 4.27) to obtain $\mathcal{R}$.

4.3 Tensor Interaction

In the low saturation limit we have found the atom field interaction to takes the form

$$H_{\text{int}} = -\frac{1}{4} \mathbf{E}^* \cdot \overleftrightarrow{\alpha} \cdot \mathbf{E}. \tag{4.35}$$

The key physical properties of this interaction are seen by decomposing the polarizability tensor into irreducible tensor components,

$$H_{\text{int}} = -\frac{1}{4} \left[\alpha^{(0)} |\mathbf{E}|^2 + \overleftrightarrow{\alpha}^{(1)} \cdot (\mathbf{E}^* \times \mathbf{E}) + \alpha_{ij}^{(2)} \left(E_i^* E_j - \frac{1}{3} |\mathbf{E}|^2 \delta_{ij} \right) \right], \tag{4.36}$$

where the superscripts denote the irreducible rank. Dynamics generated by this interaction act to affect the field through the polarization-dependent index of refraction and to affect the state of the atoms through the polarization-dependent light-shift, discussed below. Under our assumption that only a single transition is probed by a monochromatic laser we take $\mathbf{E} = E_0 \epsilon$ turned near an optical resonance $nS_{1/2} \rightarrow nP_{J'}$ with $J' \in 1/2, 3/2$, i.e. a D1 or D2 transition. As derived in

Appendix C, the atom-field interaction Hamiltonian acting on a given ground-state hyperfine manifold with total angular momentum F for light detuned near from an given excited state manifold with total angular momentum F' is

$$H_{J'F'F} = V_{F'F}\left[C^{(0)}_{J'F'F}\left|\epsilon\right|^2 + C^{(1)}_{J'F'F}\frac{\epsilon^*\times\epsilon}{i}\cdot\mathbf{F} + C^{(2)}_{J'F'F}\left(\left|\epsilon\cdot\mathbf{F}\right|^2 - \frac{1}{3}\mathbf{F}^2\left|\epsilon\right|^2\right)\right]P_F \tag{4.37}$$

where $\left|A\right|^2 \equiv \frac{1}{2}\left[A^\dagger A + AA^\dagger\right]$. The overall scale,

$$V_{F'F} = \frac{\left|\langle P\|\,\mathbf{d}\,\|S\rangle\right|^2 E_0^2}{4\hbar\Delta_{F'F}} = \frac{\hbar\Gamma}{8}\frac{I}{I_{\rm sat}}\frac{1}{\bar{\Delta}_{F'F}}, \tag{4.38}$$

is the ac Stark shift associated with a field of intensity I acting on a transition with unit oscillator strength and saturation intensity $I_{\rm sat}$ detuned by $\bar{\Delta}_{F'F} = \Delta_{F'F}/\Gamma$. The tensor contributions are expressed in the bracketed terms of Eq. (4.37), where the coefficient for the K'th irreducible component follows from the Wigner-Eckert theorem as given in the appendix Eq. (C.23a). The total atom-field interaction for a given transition in this representation is the sum over all hyperfine resonances within an excited-state hyperfine-structure manifold, $H_{J',F} = \sum_{F'} H_{J'F'F}$.

4.3.1 Tensor field dynamics

Given the state-dependent tensor polarizability of the atomic sample, one can continuously perform a weak measurement on the atomic spin by monitoring the polarization of a probe laser beam that traverses the sample. For a plane-wave probe propagating in the $\mathbf{e}_k$ direction, the off-resonant interaction couples the atomic spin and field Stokes vector components of the polarization ϵ,

$$S_0 = \left|\epsilon_H\right|^2 + \left|\epsilon_V\right|^2, \tag{4.39}$$

$$S_1 = \left|\epsilon_H\right|^2 - \left|\epsilon_V\right|^2, \tag{4.40}$$

$$S_2 = \epsilon_H^*\epsilon_V + \epsilon_V^*\epsilon_H = \left|\epsilon_{+45^\circ}\right|^2 - \left|\epsilon_{-45^\circ}\right|^2, \tag{4.41}$$

$$S_3 = -i(\epsilon_H^*\epsilon_V - \epsilon_V^*\epsilon_H) = \left|\epsilon_+\right|^2 - \left|\epsilon_-\right|^2, \tag{4.42}$$

where ϵ_H, ϵ_V are components along linear horizontal and vertical directions, $\epsilon_{\pm 45^\circ}$ are the components at $\pm 45^\circ$, and $\epsilon_\pm$ are the components with positive and negative helicity. The Stokes coupling terms in the light-shift potential for a fixed ground-hyperfine manifold F follow from the irreducible tensor decomposition, Eq. (4.37)

$$H_{\text{int}} = A_0 S_0 + A_1 S_1 + A_2 S_2 + A_3 S_3, \tag{4.43}$$

$$A_0 = V^{(0)}_{J'F} - \frac{V^{(2)}_{J'F}}{6}\left(3F_k^2 - F^2\right), \tag{4.44a}$$

$$A_1 = V^{(2)}_{J'F}\frac{F_H^2 - F_V^2}{2}, \tag{4.44b}$$

$$A_2 = V^{(2)}_{J'F}\frac{F_H F_V + F_V F_H}{2}, \tag{4.44c}$$

$$A_3 = V^{(1)}_{J'F} F_k \tag{4.44d}$$

where $V^{(K)}_{J'F} = \sum_{F'} C^{(K)}_{J'F'F} V_{F'F}$ are the effective light-shift coefficients stemming from the irreducible components. Expressed in this way, we explicitly see the effects of the atoms on the dynamics of the field. The polarization-independent index of refraction is set by the S_0 term. The remaining terms generate a rotation of the Stokes vector on the Poincaré sphere about an axis and angle depending on the moments of the atomic spin distribution according to a Hamiltonian of the form $H_{\text{int}} = \mathbf{A} \cdot \mathbf{S}$. Rotation about the 3-axis precesses the Stokes vector in the equatorial plane of the Poincaré sphere by an amount proportional to the atomic magnetization along the propagation direction - the Faraday effect. Rotation about the 1-axis or 2-axis transforms the ellipticity of the probe - birefringence. A polarization measurement subsequent to this interactions will effect a QND measurement of some linear combination of these three atomic observables.

For an ensemble of N atoms in an optically thin sample such that all atoms couple identically to the field, the mean rotation angle is determined by mean moments of the atomic spin variables. Rotation about some axis of the Poincar sphere is given by the difference in the phase shifts of the corresponding two orthogonal polarization

components of the field that define that Stokes axis. To find this angle, note that for a sample of atoms of density n with resonant absorption cross section σ_0 in which a plane wave of intensity I propagates a length L, the phase shift on the field relative to vacuum is $\delta\phi = -\mathrm{OD}_0(V/\hbar\gamma_{s0})$, where $\mathrm{OD}_0 = n\sigma_0 L$ is the optical density on resonance, V is the light shift potential, and $\gamma_{s0} = (I/I_{\mathrm{sat}})\Gamma/2$ is the resonant photon scattering rate (in the low saturation regime). Given a more general Hamiltonian for a tensor polarizability of the form $H = VA\left(\left|\epsilon_{n_+}\right|^2 - \left|\epsilon_{n_-}\right|^2\right)$, where A is an atomic operator, it follows that the phase shifts of the two orthogonal polarization components $\epsilon_{n_\pm}$ are equal and opposite, $\delta\phi_{n_+} - \delta\phi_{n_-} = 2\mathrm{OD}_0(V/\hbar\gamma_{s0})\langle A\rangle$. Using Eq. (4.44a) we determine the angles of rotation about each of the three axes to be,

$$\begin{aligned}\Theta_1 &= \delta\phi_V - \delta\phi_H \\ &= 2\mathrm{OD}_0 \frac{V^{(2)}_{J'F}}{\hbar\gamma_{s0}} \left\langle \frac{F_H^2 - F_V^2}{2} \right\rangle \\ &= \frac{\mathrm{OD}_0}{4} \left(\sum_{F'} \frac{C^{(2)}_{J'F'F}}{\bar{\Delta}_{F'F}} \right) \left\langle \frac{F_H^2 - F_V^2}{2} \right\rangle \end{aligned} \tag{4.45a}$$

$$\begin{aligned}\Theta_2 &= \delta\phi_{-45^\circ} - \delta\phi_{+45^\circ} \\ &= 2\mathrm{OD}_0 \frac{V^{(2)}_{J'F}}{\hbar\gamma_{s0}} \left\langle \frac{F_H F_V + F_V F_H}{2} \right\rangle \\ &= \frac{\mathrm{OD}_0}{4} \left(\sum_{F'} \frac{C^{(2)}_{J'F'F}}{\bar{\Delta}_{F'F}} \right) \left\langle \frac{F_H F_V + F_V F_H}{2} \right\rangle \end{aligned} \tag{4.45b}$$

$$\begin{aligned}\Theta_3 &= \delta\phi_V - \delta\phi_H \\ &= 2\mathrm{OD}_0 \frac{V^{(1)}_{J'F}}{\hbar\gamma_{s0}} \left\langle \frac{F_k}{2} \right\rangle \\ &= \frac{\mathrm{OD}_0}{2} \left(\sum_{F'} \frac{C^{(1)}_{J'F'F}}{\bar{\Delta}_{F'F}} \right) \left\langle \frac{F_k}{2} \right\rangle \end{aligned} \tag{4.45c}$$

In the optically thin limit where $\Theta_i \ll 1$, the fields Stokes vector is transformed according to

$$\mathbf{S}_{\mathrm{out}} \approx \mathbf{S}_{\mathrm{in}} + \boldsymbol{\Theta} \times \mathbf{S}_{\mathrm{in}} \tag{4.46}$$

Maximum sensitivity in the measurement is achieved when the polarimeter analyzes the output along a direction of the Poincaré sphere ($\mathbf{E}_{\text{out}}$) orthogonal to the input. In this case the signal is approximately proportional to

$$\mathbf{e}_{\text{out}} \cdot S_{\text{out}} \approx (\mathbf{S}_{\text{in}} \times \mathbf{e}_{\text{out}}) \cdot \theta. \tag{4.47}$$

For example, taking the input polarization along the $\mathbf{e}_H$-direction, $\mathbf{S}_{\text{in}} \propto \mathbf{e}_1$, and an output analyzer along the linear diagonal $\mathbf{e}_{\pm 45^\circ}$ -directions, $\mathbf{e}_{\text{out}} = \mathbf{e}_2$, performs an ensemble measurement of $\langle F_k \rangle$ via Faraday rotation, $\mathbf{e}_{\text{out}} \cdot \mathbf{S}_{\text{out}} \propto \Theta_3$, whereas an output analyzer in the circular basis, $\mathbf{e}_{\text{out}} = \mathbf{e}_3$, performs a measurement of the second order atomic moment $\langle F_H F_V + F_V F_H \rangle$ due to birefringence in the sample, $\mathbf{e}_{\text{out}} \cdot \mathbf{S}_{\text{out}} \propto \Theta_2$. Such measurements can be used to continuously observe the dynamics of the atomic spin due to the existence of external fields and/or the effects of the probe itself. An example of such continuous measurements will be provided in the next Sec. 4.5.

4.3.2 Tensor spin dynamics

The decomposition of the interaction into its irreducible tensor components (Eq. 4.37) provides a deeper understanding of the atomic dynamics just as it did for the measurement dynamics. The rank-0 component produces an equal energy level shift for all sublevels within a ground hyperfine manifold, depending only on the total intensity of the field . For systems restricted to a single ground state manifold, as the one we consider is, this term does not drive atomic dynamics. The rank-1 component induces a Zeeman-like interaction, $H^{(1)} = \mathbf{B}_{\text{fict}} \cdot \mathbf{F}$, which generates rotations about a fictitious magnetic field $\mathbf{B}_{\text{fict}} \propto -i\,(\epsilon^* \times \epsilon)$, which in turn depends on the ellipticity of the laser polarization. The rank-2 component contains a nonlinear light-shift proportional to $|\epsilon \cdot \mathbf{F}|^2$, generating dynamics beyond SU(2) rotations. Specializing to the case of a linearly polarized field, which we shall consider in the sequel, the

fictitious magnetic field vanishes, so that only the term quadratic in the atomic angular momentum remains (ignoring the scalar piece which does not affect the dynamics),

$$V_{J'F'F} = V_{FF'}\left[C^{(0)}_{J'F'F} + C^{(2)}_{J'F'F}\left(|\epsilon\cdot\mathbf{F}|^2 - \frac{1}{3}\mathbf{F}^2\right)\right]P_F. \tag{4.48}$$

The effective potential governing spin dynamics of an atom probed by a linearly polarized laser and coupled to a magnetic field can be compactly written as

$$V = g_F\mu_g\mathbf{B}(t)\cdot\mathbf{F} + \beta_{\mathrm{NL}}\left|\epsilon_L\cdot\mathbf{F}\right|^2. \tag{4.49}$$

β_{NL} is a constant that hides all of the complications of the hyperfine interaction, and is given by

$$\beta_{NL} = \sum_{F'} V_{FF'}C^{(2)}_{J'F'F}\hbar\gamma_{s0}. \tag{4.50}$$

4.4 Control of Spin Dynamics

What amount of control can be achieved in our example system consisting of an alkali atom probed linearly polarized laser and subject to time dependent magnetic fields? The system consists of a single spin with total angular momentum F, so the most general unitary operation on this system is some element of the group $SU(2F+1)$. How much of this group does the Hamiltonian in Eq. (4.49) allow us to reach? Before answering this question first consider what happens when the laser is off,

$$H \propto \mathbf{B}(t)\cdot\mathbf{F}. \tag{4.51}$$

The most general time evolution operator that can be achieved using and arbitrary time dependent magnetic field is

$$U(t) = e^{\theta(t)\mathbf{n}(t)\cdot\mathbf{F}}, \tag{4.52}$$

which corresponds to an arbitrary rotation, i.e. some element of the group $SU(2)$. An alternative method of deriving this is to look at the algebra generated by the independently controllable terms in the Hamiltonian, along with the drift term if any is present [**?**]. The controllable terms are proportional to F_x, F_y, F_z. The commutation relations among these terms is,.

$$[F_i, F_j] = i\hbar\epsilon_{ijk}F_k. \tag{4.53}$$

We see that the algebra of these operators closes upon itself, and is exactly equal to the algebra $su(2)$. The accessible group of unitaries is then given by the exponentiation of this algebra, giving the group $SU(2)$ as expected. Note that the result would have been the same if we restricted the magnetic field to be solely in the x, y plane and to have fixed amplitude $\mathbf{B} = B_0\left[\sin(\theta(t))\mathbf{e}_x + \cos(\theta(t))\mathbf{e}_y\right]$, as the algebra generated is unchanged under these restrictions. Use of this fact is made in Chap. 5.

Now returning to the full Hamiltonian (Eq. 4.49), we can ask the same question. The independently controllable operators are the same as in the pure magnetic field case, $\{F_x, F_y, F_z\}$, but we now also have a drift term proportional to $F_{\mathbf{k}}^2 = F_x^2$, where we take $\mathbf{k} = \mathbf{e}_x$ without loss of generality. Looking at the commutators of these elements one sees that the algebra does not close on this set, rather one can make new terms such as

$$\left[F_x^2, F_y\right] \propto F_xF_z + F_zF_x \quad \left[F_xF_z + F_zF_x, F_x^2\right] \propto F_x^2F_y + F_yF_x^2 + 2F_xF_yF_x. \tag{4.54}$$

We see in the second example that third order moments of the atomic variables can be generated. By repeated commutations one can generated arbitrarily high order moments of $\mathbf{F}$. In fact by repeated commutations one can make every possible element in the entire $su(2F+1)$ algebra[**?**]. This implies that by a suitable choice of time dependent magnetic fields one can generate any possible unitary.

At this point it is worth noting that the nonlinear term F_x^2 comes at a price. The nonlinearity is induced by an ac Stark shift, which requires at least some excitation

to the excited state. This excitation induces decay of the system. Since the nonlinear term is required to achieve full controllability one cannot generate an arbitrary unitary operation without inducing at least some decoherence in this system. In the far detuned limit one finds that the ratio of the nonlinearity to decoherence becomes independent of detuning [**?**], for example in ^{133}Cs this ratio is 1.20 for the D2 transition. Alternatively near resonance on the D1 transition one can achieve ratios of up to 11.5. The inherent decoherence necessary to allow full control of the system will play a large part in quantum state tomography using continuous measurements as discussed in Chap. 5.

As a simple example of control we consider how to eliminate the nonlinear term in Eq. (4.49) through suitable choice of magnetic fields. One possible way to achieve this can be seen as follows. Choose a strong constant magnetic field in the $x-y$ plane,

$$\mathbf{B}(t) = B_0 \left[\cos(\theta)\mathbf{e}_x + \sin(\theta)\mathbf{e}_y\right], \tag{4.55}$$

This field will cause the atoms to precess at the frequency $\omega_L = g_F \mu_g B_0/\hbar$. Transforming to the rotating frame at this frequency the initial Hamiltonian

$$H = \omega_L \left[\cos(\theta)F_x + \sin(\theta)F_y\right] + \beta_{\mathrm{NL}} F_x^2 \tag{4.56}$$

is transformed to

$$H^{(I)} = \beta_{\mathrm{NL}} \left[\cos(\theta)F_x + \sin(\theta)\cos(\omega_L t)F_z + \sin(\theta)\cos(\omega_L t)F_y\right]^2. \tag{4.57}$$

Assuming that ω_L is much larger than any of the other frequencies in the problem we can make the rotating wave approximation

$$h^{(I)} = \beta_{\mathrm{NL}} \left[\cos^2(\theta)F_x^2 + \frac{\sin^2(\theta)}{2}\left(F_z^2 + F_y^2\right)\right]. \tag{4.58}$$

Then note that $F_x^2 + F_y^2 + F_z^2 = F^2 = F(F+1)$ is a constant. Subtracting $\beta_{\mathrm{NL}} F(F+1)\sin^2\theta$ from the Hamiltonian results in a simpler form,

$$h^{(I)} = \beta_{\mathrm{NL}} F_x^2 \left[\cos^2(\theta) - \frac{1}{2}\sin^2(\theta)\right], \tag{4.59}$$

that maintains the same dynamics. Choosing $\tan(\theta) = \sqrt{2}$ will then magically cancel out the nonlinearity at $\theta \approx 54.7°$. Transforming back to the initial frame the dynamics just exhibit Larmor precession at frequency ω_L. Generally one may tune the nonlinearity anywhere in the range from 100% to -50% of its maximum value. Much more complicated control fields will be explored in Chap. 5.

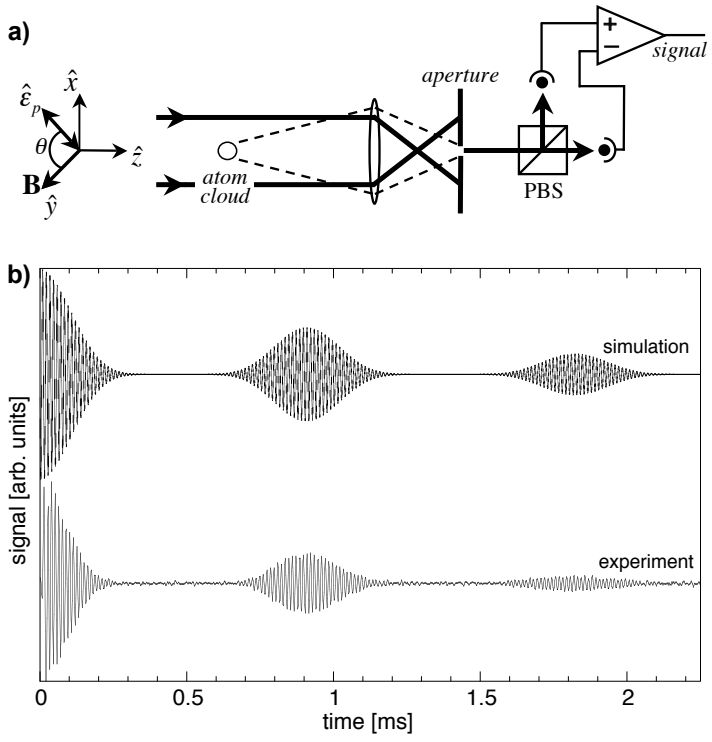

Figure 4.1: a)Diagram of the experimental setup. b)Simulation and experiment depicting nonlinear collapse and revival of the Larmor precession Faraday signal of an ensemble of ^{133}Cs atoms subject to a constant magnetic field and probed by a linearly polarized laser on the D2 transition.[3]

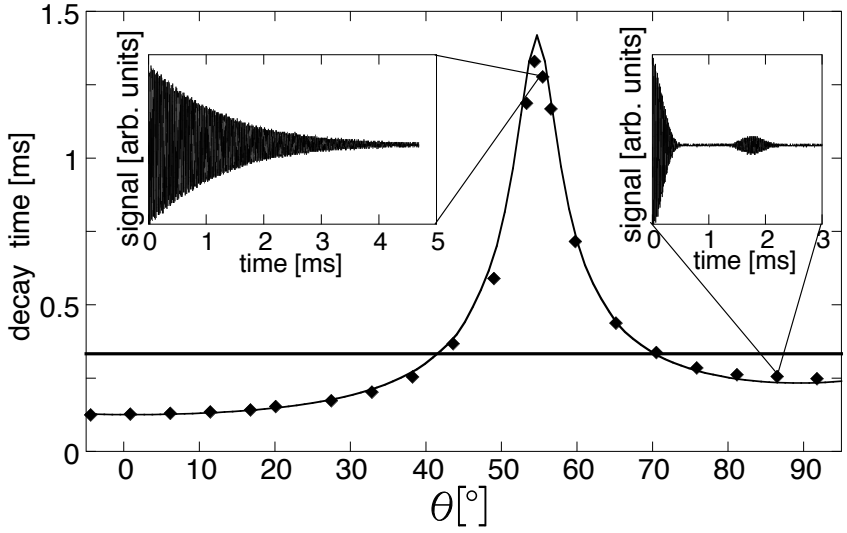

Figure 4.2: Collapse time in milliseconds of the Larmor signal obtained from a large constant magnetic field in the $x-y$ plane versus the angle the field makes with the x-axis. At the magic angle of $\theta \approx 54.7°$ the nonlinear collapse disappears and the measured collapse rate corresponds to the decoherence time due to photon scattering. This is clearly seen by noting the exponential shape of the collapse when $\theta = 54.7°$ compared to the characteristic Gaussian shape of inhomogeneous decay observed in Fig. 4.1.[3]

4.5 Experimental control of a quadratic ac Stark shift

Having delved into the complicated dynamics of a real cesium atom interacting with a laser we now wish to make contact whit actual experimental results. The most natural way to achieve this goal is to exploit the measurement process described in Sec. 4.3.1. To this end consider a situation where all of the cesium atoms are initially prepared in a ground state with total angular momentum F and further as eigenstates of the operator $F_x \left|\psi(0)\right\rangle = F \left|\psi(0)\right\rangle$, i.e. the so called coherent spin states. Then a magnetic field $\mathbf{B} = B_0 \mathbf{e}_y$ is applied to the atoms. On its own, the Zeeman interaction preserves each atom in a spin-coherent state as it precesses in the

x-z plane at the Larmor frequency, $\Omega = \mu_B B_0/\hbar F$. In contrast, the non-linear part of the light shift drives spin dynamics that go beyond simple rotations. The increase in the number of frequencies leads to a gradual collapse of the initial spin-coherent state. The action of the quadratic nonlinearity Eq. (4.49) on the finite dimensional Hilbert space implies that there are only F distinct dynamical eigenfrequencies available to the system, and one therefore expects the initial collapse to be followed by a series of revivals. Fig. 4.1 shows an example of the resulting time variation in the Faraday angle $\Theta_3 \propto \langle F_z \rangle$ corresponding to a measurement of the initial vertically polarized laser in the $\pm 45^\circ$ basis, for a far detuned probe of the D2 transition. Also shown is a master equation simulation of the spin dynamics as generated by the code in Appendix B. which shows good quantitative agreement with the data. The faster decay of the experiment is due to an inhomogeneous spatial intensity and magnetic field, that were not modeled. By rotating the angle of the Larmor precession field in the $x - y$ plane we can alter the strength of the nonlinear terms as discussed in Sec. 4.4. In Fig. 4.2 we see that by choosing the Larmor field along $(\sqrt{2}\mathbf{e}_x + \mathbf{e}_y)/\sqrt{3}$ the nonlinear collapse is completely removed, leaving only Larmor precession and decay.

Even stronger and more numerous revivals can be observed by increasing the strength of the non-linearity relative to the rate of decoherence. Moving near resonance on the $S_{1/2} \rightarrow P_{1/2}$ $D1$ transition of Cs, where the excited state hyperfine splitting is roughly five times larger than for the D2 transition accomplishes this. The strength of the rank-2 tensor coupling is maximized by tuning the probe in-between the $F' = 3, 4$ hyperfine transitions, in which case the nonlinearity to scattering can be increased to as much as 11.5. Fig. 4.3 shows the highly coherent collapse and revival dynamics that can be achieved in this situation, again using a Faraday probe. Note the broadening of the peeks of the later revivals, which does not show up in the basic simulation. This broadening is due to the inhomogeneity of the intensity across the sample. Including a 5% inhomogeneity in the intensity as well as an additional $13ms$ decay constant, presumably due to magnetic field inhomogeneity, one recovers

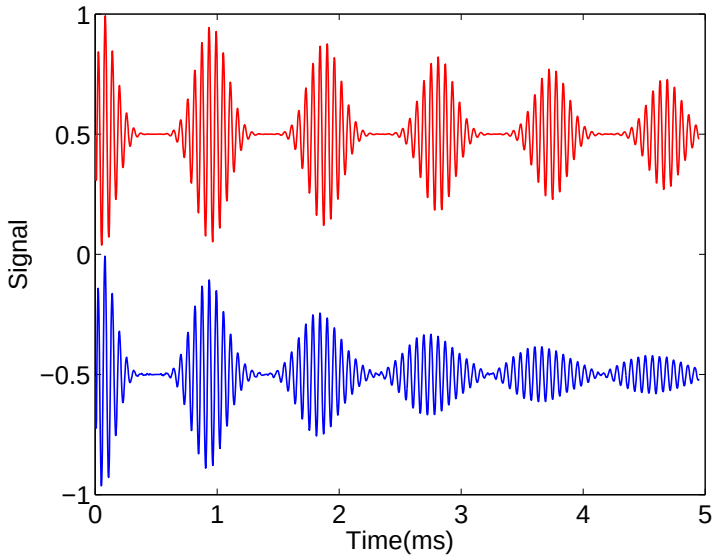

Figure 4.3: At bottom in blue is shown the collapse revival data for a faraday measurement of a laser probing the D1 transition. Many more revivals can be seen using this transition due to the larger hyperfine splitting of the D1 transition relative to the D2 transition depicted in Fig. 4.1. A simulation of the data using the light shift estimated from the initial collapse is shown above in red. Note the revivals all have the same width, while in the actual data the later revivals tend to spread out, and exhibit a extra decay.

the measured signal almost exactly (Fig. 4.4).

Choosing a different measurement basis we can extract information about a different component of the atomic spin. Specifically Fig. 4.5 depicts output measurement along the stokes vector $.19\mathbf{s}_2 - .95\mathbf{s}_3$, corresponding to a measurement primarily in the circular basis $\epsilon_\pm$. Such a measurement couples to the second order atomic moment $\langle F_x F_y + F_y F_x \rangle$. The slight divergence at later times seen in the figure is most likely due to improperly taking account of inhomogeneity in the magnetic field, or to drift in the applied fields.

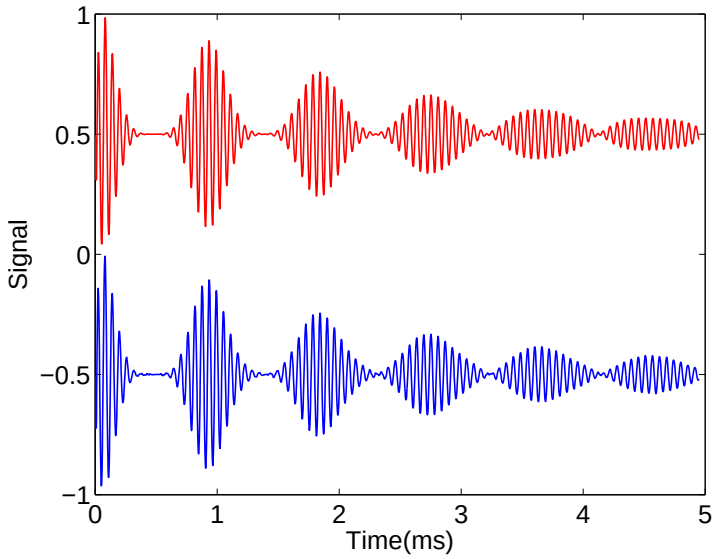

Figure 4.4: Again the collapse-revival data for the D1 line is show at bottom in blue as in Fig. 4.3. Here however the simulation, shown in red, includes an estimated 5% spread in intensity over the sample and an estimate 13ms decay rate due to magnetic field inhomogeneity. For details of the estimation procedures used see Sec. 5.2.2

4.6 Summary

A deep understanding of the interaction between an alkali atom and a linearly polarized laser allows us to exploit the rich dynamics of the alkali ground state. In this chapter we looked at how adiabatic elimination allows us to derive dynamics for a single hyperfine ground state of a cesium atom interacting with a classical light field. The reduced dynamics provide an avenue for performing QND measurement of several atomic observables through the conduit of the light field. The reduced dynamics also clearly demonstrate how a single hyperfine manifold can be controlled by judicious application of magnetic fields and interaction with a linearly polarized laser probe.

Sythesizing the entire treatment we use a simulation based upon the developed

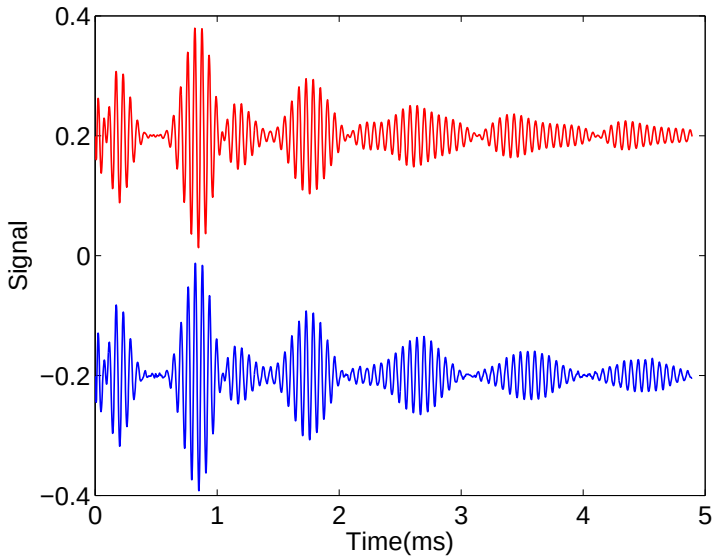

Figure 4.5: Larmor precession data obtained using the experimental birefringence measurement. This measurement has a large component corresponding to a direct measurement of a second order atomic moment $\{F_x, F_y\}$. Actual data is shown in blue on bottom, while simulated data is shown in red on top. Not the slight divergence at later times.

theory to model experiments performed at the University of Arizona by our collaborators. We find that the experiments can reproduce the rudimentary control of the nonlinearity discussed in Sec. 4.4. We also find excellent quantitative agreement between experiment and theory, which agreement is made almost exact, within the limits set by shot noise, when one includes the sources of inhomogeneous decay. Such excellent agreement provides the basis upon which the tomographic procedure discussed in the next chapter is built. In addition it opens the door for many possible future experiments, including some which are currently under way, such as preparation of an arbitrary initial state, and examinations of the quantum to classical transition.

Chapter 5

Quantum state reconstruction with continuous measurements

The control of quantum mechanical systems is finding new applications in information processing tasks such as cryptography and computation [51]. Experimental reconstruction of a quantum state is essential to verify preparation, to detect the presence of errors due to noise and decoherence, and to determine the fidelity of control protocols using process tomography. Moreover, real-time quantum state estimation may allow improvement of precision metrology beyond the standard quantum limit [76], with the possibility of active control through closed-loop feedback protocols [33]. In addition, measurement of the quantum state can provide information about unknown or nontrivial dynamics, such as those arising in the study of quantum chaos. Laboratory demonstrations of state reconstruction are numerous and span a broad range of physical systems, including light fields [26], molecules [25], ions [70], atoms [42], spins [16, 41], and entangled photon pairs [65].

In this chapter we consider a new protocol for quantum state reconstruction based on continuous, weak measurement of a single observable on an ensemble of identically

prepared systems. The ensemble is driven so that each member undergoes an identical, carefully designed dynamical evolution that continually maps new information onto the measured quantity. This contrasts with the standard paradigm for quantum state reconstruction based on strong and therefore destructive measurements, often of a large set of observables performed on many copies of the unknown state. Our weak measurement approach allows for efficient fast and accurate reconstruction of the initial quantum state. The procedure can be tailored to extract the minimal amount of information necessary for reconstruction. This keeps the disturbance of the state to a minimum making it feasible to use the extracted information to control the system under observation. By making the procedure real time one could use the knowledge of the entire state to perform full state based feedback control. This contrasts with the control policies up to now which have used control policies based upon simple functions of the measured observables[**?**], or have employed Gaussian approximations to the actual quantum state [49, 34]. Our procedure is broadly applicable in any systems where continuous weak measurement tools have been developed, but can be particularly useful in systems where noise and decoherence limit the ability to perform strong measurements regardless of the amount of signal averaging such as nuclear magnetic resonance in molecules [16] and polarization spectroscopy in dilute atomic vapors [63].

We concentrate on using the tools developed to measure and control alkali atoms in Chap. 4. Using these tools we demonstrate the first experimental realization of this novel continuous measurement tomography technique using experimental data obtained by our collaborators at the University of Arizona. We begin by outlining the general continuous measurement tomography procedure, including discussion of the numerical techniques used to optimize the measurement performance, and to how semidefinite programming is employed to ensure positivity of the estimated stateSec. 5.1. While the example of an alkali atom is used to illustrate concepts in this section the procedures discussed are broadly applicable to any quantum system. Sec. 5.2

then discusses the details necessary to apply the abstract procedure outlined in Sec. 5.1 to the laboratory. The heart of this section is a discussion of the simulation used to model the experiment, the experimental parameters needed for this simulation, and how these parameters are estimated. Sec. 5.3 presents the experimental results of applying the continuous measurement tomography technique, alongside some simulated benchmarks.

5.1 General procedure

The goal of the reconstruction procedure is to invert a measurement record $M(t)$ to find the initial quantum state ρ_0. We accomplish this goal by using detailed knowledge of the dynamics, $\mathcal{L}$, and measurement processes, $\mathcal{M}$, of the system under study to determine the probability of observing a signal $M(t)$ conditional upon having an initial state ρ_0,

$$P\left(M(t)|\rho_0, \mathcal{M}, \mathcal{L}\right). \tag{5.1}$$

Use of Baye's Rule [**?**] allows us to invert this conditional distribution to find the posterior distribution,

$$P\left(\rho_0|M(t), \mathcal{M}, \mathcal{L}\right) = A\ P\left(M(t)|\rho_0, \mathcal{M}, \mathcal{L}\right) P\left(\rho_0\right), \tag{5.2}$$

representing the probability that $M(t)$ resulted from the given initial state ρ_0. Here A is a normalization and $P\left(\rho_0\right)$ contains all our prior information about the initial state. To estimate the initial state we choose

$$\bar{\rho} = \underset{\rho_0}{\text{argmax}}\ P\left(\rho_0|M(t), \mathcal{M}, \mathcal{L}\right), \tag{5.3}$$

which is the state with the highest probability of having generated the observed measurements, i.e. the maximum likelihood estimate.

The above general procedure can be found in any book on statistical inference, for example [**?**], and is applicable to an arbitrary system, be it classical or quantum or some new as yet unknown type. To apply this to a continuously measured quantum system we need to consider how knowledge of the measurement process $\mathcal{M}$ and of the dynamics $\mathcal{L}$ can be used to generate the conditional distribution Eq. (5.1). This is done in Sec. 5.1.1 alongside some considerations of the possible prior information. Sec. 5.1.2 then discusses how to solve Eq. (5.3) using minimal prior information. Sec. 5.1.3 examines how system dynamics can be tailored to extract the maximum amount of information possible in the minimum amount of time. This requires a complex optimization procedure which is specific to the system under study. We therefore specialize our considerations in this section to the candidate reconstruction of the $F = 3$ hyperfine ground state of ^{133}Cs.

5.1.1 Fundamentals

State estimation in a quantum setting requires many copies of the initially prepared state, as the uncertainty principle guarantees that measurement of any observable O will introduce noise into future measurements of conjugate observables. On a single system of dimension d this backaction noise limits the total information that can be extracted to at most $\log_2 d$ bits. Our protocol thus starts by assuming a single ensemble of systems all prepared in the same initial state ρ_0,

$$\rho_N(0) = \rho_0^{\otimes N}. \tag{5.4}$$

The unmonitored evolution of the system is assumed to be separable such that each atom evolves under the master equation

$$\frac{d}{dt}\rho = \mathcal{L}[t]\left(\rho(t)\right). \tag{5.5}$$

This assumption can be relaxed slightly to allow inhomogeneities in the evolution across the ensemble as discussed is Sec. 5.2.1. Under this assumption the system

state at all times is

$$\rho_N(t) = \rho(t)^{\otimes N} \tag{5.6}$$

The system is then monitored by a probe that measures the sum of the identical observables $\{O\}$ on each member. The central limit theorem ensures that the measurement record of this probe has the form

$$M(t) = \alpha \left[N \left\langle O \right\rangle_t + \Delta M(t) \right], \tag{5.7}$$

where $\left\langle O \right\rangle_t$ is the quantum expectation value at time t, $\Delta M(t)$ is a Gaussian white noise process with variance $\sigma^2 = 1/\kappa\Delta t$ for measurement strength κ and detector averaging time Δt, and α is some proportionality constant given by the specific experimental parameters that convert the quantum observables to units of the meter. In principle a measurement of the collective observable $N \left\langle O \right\rangle_t$ leads to backaction on the collective many-body state and can cause individual members of the ensemble to become correlated [44, 33], conflicting with our assumption of separable dynamics 5.6. Such correlations contaminate the outcome of future measurements and greatly complicate the task of reconstructing the initial state ρ_0. Additionally, the gain from performing such quantum limited measurements is small, as the majority of the information about the state of individual ensemble members has already been extracted by the probe prior to reaching the quantum limited regime. We thus restrict our considerations to cases where the measurement uncertainty, averaged over the total measurement time T, is large compared to the intrinsic quantum uncertainty (projection noise) of the collective observable, $1/\kappa T > N\Delta O^2$, and backaction onto the collective state is insignificant. Experimentally this is also the most common situation. Of course a sufficient measurement signal-to-noise ratio must still be available to reconstruct the state of an individual member of the ensemble. This requires $N >> 1$ so that the quantum backaction associated with information gain is distributed uniformly among the entire ensemble, with negligible disturbance of any single member state.

Since the goal is to invert the measurement history, Eq. (5.7), to determine ρ_0 for all possible initial states, it is most convenient to work in the Heisenberg picture and express

$$\langle O \rangle_t = \mathrm{Tr}\left[O(t)\rho_0\right] = \left(O(t)|\rho_0\right), \tag{5.8}$$

where in the second equality we have written the trace as an inner-product between vectorized operators in the superoperator picture [14]. The superoperator picture simply acknowledges that the set of operators also forms a vector space, and specifically that the expected measurement $\mathrm{i}\langle O \rangle$ is just a linear combination of the elements of the density operator ρ_0. We coarse grain over the detector response time Δt, such that $(O_i| = \int_{t_i}^{t_i+\Delta t} (O(t)|\, dt/\Delta t$, obtaining a discrete measurement history time-series $\{M_i\}$, with

$$M_i = \alpha\left[N\left(O_i|\rho_0\right) + \sigma W\right], \tag{5.9}$$

where now the measurement operators $\{O_i\}$ can be determined in advance from the known dynamics, and where W is a Gaussian random variable with zero mean and unit variance. This equation recasts the reconstruction problem as a stochastic linear estimation problem for the underlying state vector ρ_0.

In order to reconstruct the state from the measurement time-series, the set of measurements operators $\{O_i\}$ must be informationally complete, spanning the space of density operators. This is most easily achieved by introducing an explicit set of control parameters, with a time dependent series of Hamiltonians $\{H_i\}$. If the system is controllable, as in the case of our example system as seen in Sec. 4.4, then the controls can be chosen to explicitly explore the space as any possible Hermitian operator in $su(d)$ can be reach from any base observable O_0. Generally the problem of exploring the space will be complicated by decoherence and inhomogeneity both of which degrade the measurement; how to optimize in the presence of these issues is the subject of Sec. 5.1.3.

The evolving measurement operators can be numerically calculated given an explicit form for the base observable $(O|$ and for the generator of the system evolution $\mathcal{L}(t)$ for any system of reasonable size, $d < 100$. The techniques used to perform the numerical integration necessary in our example system with $d = 7$ are discussed in Sec. 5.2.1, and the code used is presented in Appendix B.

As discussed above a Bayesian filter (Eq. 5.2) determines how our knowledge of the initial state is updated due to a measurement history $\{M_i\}$,

$$P(\rho_0|\{M_i\}) = AP(\{M_i\}|\rho_0)P(\rho_0). \tag{5.10}$$

The normalization constant A drops out of the maximization in Eq. (5.3). The prior distribution $P(\rho_0)$ must include the fact that ρ_0 is a valid density matrix (ie. is Hermitian, has trace one and is positive). Generally it can also include different information about the state. It is common to have some knowledge about the spectrum of the state, for example the initial state could be known to be pure, or to be derived by taking the partial trace of a pure state over some larger system. Through the rest of this paper, and specifically in Sec. 5.1.2, we assume a minimal prior, corresponding to a uniform distribution over all possible physical states, with functional form

$$P(\rho_0) = B\ \delta^{d^2}\left(|\rho_0) - |\rho_0^\dagger)\right)\delta(\mathrm{Tr}\left[\rho_0\right] - 1)\Theta(\rho_0), \tag{5.11}$$

with B a normalization, $\delta^n(x)$ the Kronecker delta function in n dimensions and $\Theta(\rho)$ a generalization of the standard step function for operator arguments such that

$$\Theta(\rho_0) = \begin{cases} 1 & \rho_0 \text{ is positive} \\ 0 & \text{otherwise} \end{cases} \tag{5.12}$$

The conditional distribution, $P(\{M_i\}|\rho_0)$ has a Gaussian form due to the assumed measurement statistics. An individual measurement outcome M_i is specified by its mean $\alpha N\left(O_i|\rho\right)$ and its variance $\alpha\sigma$ which we assume is the same for all

measurements, and thus has probability distribution

$$P(M_i|\rho_0) = Ae^{-(M_i-\alpha N(O_i|\rho))^2/\alpha^2\sigma^2}. \tag{5.13}$$

We obtain the full conditional by multiplying all the individual distributions together to get

$$P(\{M_i\}|\rho_0) = A^N \exp\left[-\frac{N^2}{\sigma^2}\sum_i \left(\frac{M_i}{\alpha N} - (O_i|\rho)\right)^2\right]. \tag{5.14}$$

Which can be put into the form of a single multivariable Gaussian,

$$P(\{M_i\}|\rho_0) \propto \exp\left[-\left(\delta\rho\right|\mathcal{R}\left|\delta\rho\right)\right]. \tag{5.15}$$

with $\delta\rho = \rho_0 - \rho_{\mathrm{OLS}}$. Equating the exponents in Eq. (5.14) and Eq. (5.15) we find that superoperator $\mathcal{R}$ is the covariance matrix for the measurements

$$\mathcal{R} = \frac{N^2}{\sigma^2}\sum_i \left|O_i\right)\left(O_i\right|. \tag{5.16}$$

and ρ_{OLS} is the ordinary least squares estimate of the state given the measurements, which does not include prior information,

$$\left|\rho_{\mathrm{OLS}}\right) = \frac{N^2}{\sigma^2}\sum_i \frac{M_i}{\alpha N}\mathcal{R}^{-1}\left|O_i\right). \tag{5.17}$$

This evolving covariance matrix generalizes the classical update rule discussed in [49]. The conditional probability distribution has entropy

$$S = -\log\mathcal{R} = -\sum_j \log\lambda_j, \tag{5.18}$$

where λ_j are the eigenvalues of the covariance matrix, corresponding to the inverse of the variances of Eq. (5.15) along its primary axes. $\sqrt{\lambda_j}$ is the signal-to-noise-ratio with which we can measure one of the eigen-operators of $\mathcal{R}$. This entropy thus provides a collective measure of the information gained about all parameters,

independent of the initial state and any prior information. Note that while the Gaussian form of the conditional follows from the the Gaussian nature of the underlying continuous measurement statistics such a Gaussian conditional will appear in many measurement schemes. Specifically any measurement scheme which consists of a large number of underlying independent measurements, even if it is a strong projective scheme, will give rise to Gaussian statistics due to the central limit theorem. Then all of the techniques presented in this section and the next two for constructing the Bayesian estimate will still apply, though the specific details related to their application will differ.

5.1.2 Including prior information

Pulling together the results from Sec. 5.1.1 we have an explicit form for the posterior distribution

$$P(\rho|\{M_i\}) = Ce^{-(\delta\rho|\mathcal{R}|\delta\rho)}\delta^{d^2}\left(|\rho_0) - \left|\rho_0^\dagger\right)\right)\delta(\mathrm{Tr}\left[\rho_0\right] - 1)\Theta(\rho_0). \tag{5.19}$$

Given this we now proceed to find the maximum likelihood estimate of the initial state

$$\bar{\rho} = \underset{\rho_0}{\mathrm{argmax}}\ P(\rho|\{M_i\}). \tag{5.20}$$

Due to the minimal form of the assumed prior information and the monotonicity of the exponential function this result of this optimization is exactly equivalent to the solution of the following convex optimization problem

$$\begin{aligned}
&\text{minimize} && (\rho - \rho_{\mathrm{OLS}}|\,\mathcal{R}\,|\rho - \rho_{\mathrm{OLS}}) && \text{(5.21a)}\\
&\text{subject to} && \rho - \rho^\dagger = 0 && \text{(5.21b)}\\
&\text{and} && \mathrm{Tr}\left[\rho\right] = 1 && \text{(5.21c)}\\
&\text{and} && \rho \geq 0. && \text{(5.21d)}
\end{aligned}$$

Throughout this section we employ the convention that operator inequalities are interpreted in terms of positivity so that $A \geq 0$ implies that A is positive. Similarly $A \geq B$ is interpreted as positivity of the operator $A - B$.

Convex optimization problems have a rich structure which can be exploited to help find their solutions [**?**]. In particular the problem stated in Eq. (5.21) is amenable to a specific solution method known as semidefinite programming [**?**] which efficiently solves problems of the form

$$\begin{aligned} &\text{minimize} && \mathbf{b} \cdot \mathbf{x} \\ &\text{subject to} && F_0 + \sum_i x_i F_i \geq 0. \end{aligned} \tag{5.22}$$

Here F_0, F_i can be arbitrary constant Hermitian matrices, while $\mathbf{b}$ is an arbitrary constant vector and $\mathbf{x}$ is a vector of variables to be optimized over.

The equivalence between Eq. (5.21) and Eq. (5.22) can be made manifest by several reduction steps. In the first step we remove the trace constraint (Eq. 5.21c) through use of a pseudo measurement. Then the hermiticity constraint is removed by reparameterization. Finally the introduction of a slack parameters allows us to find an explicit form for F_i and b that makes Eq. (5.22) equivalent to the reduced optimization problem.

The trace constraint from Eq. (5.21c) can be changed from an explicit to an implicit constraint with the inclusion of a pseudo measurement of the trace in the calculation of the conditional distribution. Specifically one considers a measurement of the identity operator I which has mean $(I|\rho_0) = 1$ and variance $\sigma_{\mathrm{I}}^2 \to 0$. That is one extends the measurement record by including a "measurement" that specifies $\mathrm{Tr}\,[\rho] = 1$ with no uncertainty. This transforms Eq. (5.16) and Eq. (5.17) into,

$$\mathcal{R} = \frac{N^2}{\sigma^2} \sum_i |O_i)\,(O_i| + \frac{N^2}{\sigma_{\mathrm{I}}^2} |I)\,(I|\,, \tag{5.23}$$

$$|\rho_{\mathrm{OLS}}) = \frac{N^2}{\sigma^2} \sum_i \frac{M_i}{\alpha N} \mathcal{R}^{-1} |O_i) + \frac{N}{\sigma_{\mathrm{I}}^2} \mathcal{R}^{-1} |I)\,. \tag{5.24}$$

Note that in practice the variance σ_I just needs to be much smaller than the variances associated with the measurements to enforce the trace constraint.

We remove the hermiticity constraint (Eq. 5.21b) by explicitly parameterizing our state such that any antiHermitian part is disallowed. The simplest example of such a parameterization is the generalized Bloch representation [**?**], where a state is represented by its projection onto a basis of Hermitian density operators. Here a we use a related decomposition in terms of the eigenvectors of the covariance matrix from Eq. (5.23). These eigenvectors are Hermitian by virtue of the fact that the covariance matrix is derived from the outer product of the Hermitian measurement operators (Eq. 5.23). Additionally they form a complete basis since they are the eigenvectors of a Hermitian superoperator $\mathcal{R}^\dagger = \mathcal{R}$. Decomposing $\mathcal{R}$ in its eigenbasis

$$\mathcal{R} = \sum_{i=1}^{d^2} \lambda_i \left|v_i\right)\left(v_i\right|, \tag{5.25}$$

we can write the new variables as $x_i = (v_i|\rho_0)$. Expressing the mean of the Gaussian (Eq. 5.24) in this format as well $\bar{x}_i = (v_i|\rho_{\mathrm{OLS}})$ Eq. (5.21) has been reduced to

$$\begin{aligned} &\text{minimize} && \sum_i \lambda_i (x_i - \bar{x}_i)^2 \\ &\text{subject to} && \sum_i x_i v_i \geq 0. \end{aligned} \tag{5.26}$$

At this point it would be convenient if we could also remover the positivity constraint using similar methods. The most obvious way would be to parameterize the state in a way that would force it to be positive, such as requiring $\bar{\rho} = AA^\dagger$. This can be done, however one still requires an explicit search of the new space which space has some redundant parameters, i.e. different choices for A can lead to the same final estimate $\bar{\rho}$. Such redundancy generally makes searching more difficult. Thus at this point it is more convenient to leave the constraint as is and reduce to a semidefinite program which has known solution methods.

To complete the reduction we must put Eq. (5.26) into the form of Eq. (5.22). This can be done using a technique described in [**?**] for eliminating quadratic objectives through the use of augmented constraints. Begin by introducing a slack parameters $x_{d^2+1} = t$. Then choose the constant vector

$$\mathbf{b} = \mathbf{e}_0, \tag{5.27}$$

and the constant matrices

$$F_0 = \begin{pmatrix} 0 & -\bar{\mathbf{x}}^T & 0 \\ -\bar{\mathbf{x}} & I_{d^2} & 0 \\ 0 & 0 & 0 \end{pmatrix} \tag{5.28a}$$

$$F_i = \begin{pmatrix} t & \sqrt{\lambda_i}\mathbf{e}_i^T & 0 \\ \sqrt{\lambda_i}\mathbf{e}_i & 0 & 0 \\ 0 & 0 & v_i \end{pmatrix}, \quad i = 1, \ldots, d^2. \tag{5.28b}$$

$$F_0 = \begin{pmatrix} 1 & 0 & 0 \\ 0 & 0 & 0 \\ 0 & 0 & 0 \end{pmatrix} \tag{5.28c}$$

These choices lead to an objective of the form $\min t$ which minimization is performed subject to the constraint that

$$F_0 + \sum_{i=1}^{d^2+1} x_i F_i = \begin{pmatrix} t & \delta\tilde{\mathbf{x}} & 0 \\ \delta\tilde{\mathbf{x}}^T & 0 & 0 \\ 0 & 0 & \sum_{i=1}^{d^2} i x_i v_i \end{pmatrix} \geq 0, \tag{5.29}$$

where we define $\delta\tilde{x}_i = \sqrt{\lambda_i}(x_i - \bar{x}_i)$. Noting that block diagonal form of $F_0 + \sum_i x_i F_i$ allows us to solve the positivity constraint. Positivity for the lower block ensures that $\sum_i x_i v_i \geq 0$ as required. To solve for positivity of the upper block we calculate its characteristic equation as

$$(\lambda - 1)^{d^2-1}(\lambda - t) - (\lambda - 1)^{d^2-2}\delta\tilde{\mathbf{x}} \cdot \tilde{\mathbf{x}} = 0 \tag{5.30}$$

This equation has two nontrivial eigenvalues

$$\lambda_{\pm} = \frac{(t+1) \pm \sqrt{(t+1)^2 + 4\tilde{\mathbf{x}} \cdot \tilde{\mathbf{x}} - 4t}}{2} \tag{5.31}$$

Setting the smallest of these to be positive we recover

$$t \geq \sum_{i=1}^{d^2} \lambda_i (x_i - \bar{x}_i)^2. \tag{5.32}$$

This is the only constraint on the slack parameter t. This implies that the minimum over t is obtained by saturating this bound

$$t = \sum_{i} \lambda_i (x_i - \bar{x}_i)^2. \tag{5.33}$$

Substituting this equality back into the objective we recover Eq. (5.26), which we previously showed was equivalent to our original problem in Eq. (5.21).

Putting this all together we can find a solution to Eq. (5.21) by solving the semidefinite program with parameters given by Eq. (5.27) and Eq. (5.28), which in turn depend upon the modified covariance matrix in Eq. (5.23) and ordinary least squares estimate in Eq. (5.24). To solve this semidefinite program we employ one of many possible semidefinite program solvers SeDuMi which is available free online. Details of how this program works may be found in [**?**]. If this program converges it will return the vector $x_{i\ \mathrm{opt}}$ which achieves the minimum, from which the maximum likelihood estimate of the initial state can be calculated as

$$\bar{\rho} = \sum_{i} x_{i\ \mathrm{opt}} v_i. \tag{5.34}$$

Of course the semidefinite program may not converge. Specifically if the covariance matrix is too nearly singular the routine used cannot find the optimal value resulting in an incorrectly estimated state. Fig. 5.1 shows a plot of the minimum eigenvalue of the covariance matrix that is used for the experimental reconstruction of our example system exhibited in Sec. 5.3. For times shorter than about $250\mu s$ the minimum

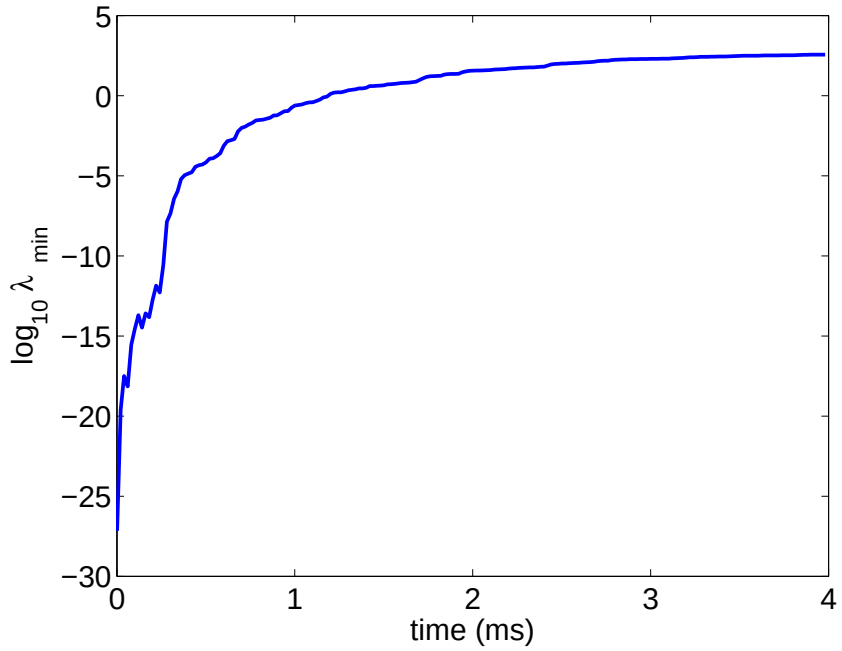

Figure 5.1: The log of the minimum eigenvalue of the covariance matrix for the conditional distribution is plotted as a function of time. For times less than about 250μs the nonlinearity has had insufficient time to evolve the initial measurement to all possible measurements. This results in a small minimum eigenvalue ($< 10^{-5}$) which in turn causes nonconvergence of the estimation procedure.

eigenvalue is too small leading to nonconvergence of the routine and thus nonpositivity of the estimated state. A different algorithm could avoid this problem, either by using more numerical accuracy, or by adding some additional information to help speed convergence.

As noted in Sec. 5.1.1 the prior assumed in this section is not the most general prior possible. One will often have knowledge about the spectrum of the initial state, for example the initial state could be known to be pure, or could be the partial trace of a pure state of a coupled system (Bures metric). Including this knowledge can greatly improve the estimate, however it can also make the optimization more difficult. In

the case of a pure state one has to solve a rank constrained semidefinite program, the solution of which is generally NP-hard[**?**]. It may, nevertheless, be possible to exploit this information using relaxations of the semidefinite programming techniques exploited in this chapter [**?**], which presents an interesting avenue for future research.

5.1.3 Optimal extraction of information

An essential part of any quantum state reconstruction technique is obtaining a sufficiently complete measurement record to accurately estimate the system state. For the continuous measurement technique described in the preceding subsections the completeness of the measurement history is quantified by the eigenvalues of the covariance matrix associated with the conditional distribution. These eigenvalues are independent of the measured state, depending only on the set of measurement operators $\{O_i\}$ which can be obtained from the dynamics and the measurement model.

As an aside one should note that the prior, through the positivity constraint, does depend on the initial state to be estimated. Specifically the action of the positivity constraint can make measurement of some variables superfluous for some initial states, as any perturbations in those variables would lead to nonpositivity of the estimated state. In fact we do see such behavior in the pure state estimates calculated in Sec. 5.3. However determining which measurements are superfluous amounts to determining the shape of the boundary of the set of positive states, which is a notoriously difficult problem. Also, to make use of this information, one must adaptively change the dynamics depending upon the current estimate of the state in a complicated fashion, as the integrated dynamics dictate the measurements performed. For both of these reasons we consider here only open loop control policies for optimizing the measurement procedure, allowing us to precalculate the dynamics along with $\mathcal{R}$.

Optimization of the dynamics to ensure maximal extraction of information of the system under study depends intimately on the systems control algebra and decoherence processes. For example in some systems one can use a Cartan decomposition of the control algebra to find simple expressions for optimal controls [**?**]. Such reductions allow for analytic or nearly analytic solutions for the optimal measurement trajectory. Due to this strong system dependence we now specialize consideration to the example system, corresponding to reconstruction of the $F = 3$ hyperfine ground state of a ^{133}Cs atom probed by a linearly polarized laser and with magnetic field controls. No convenient decomposition is known for the $su(7)$ algebra of this system. As such we attempt to perform optimization using an unstructured search routine.

To reconstruct a total angular momentum $F = 3$, we must measured $(2F+1)^2 - 1 = 48$ total parameters. We assume the linearly polarized probe beam is tuned near the D1 ($6S_{1/2} \rightarrow P_{1/2}$) resonance [63]. Information about the atomic spins is obtained by measuring either the Faraday rotation of the probe polarization $\langle M_0 \rangle = \alpha N \langle F_z \rangle$ or the birefringence of the probe $\langle M_0 \rangle = \alpha N \langle F_x F_y + F_y F_x \rangle$ as discussed in Sec. 4.3.1. Here α encodes the focusing of the laser, the conversion efficiency of the photodetector, the gain on any amplifiers, and any other experimental parameters which convert the basic measurement of atomic variables into measured voltages. Shot noise in the probe polarimeter gives rise to the fluctuations W with variance $\sigma = \sigma_{\text{shot}}/\alpha N$, which limit the measurement strength.

In the regime of strong backaction onto the collective spin state, the faraday rotation measurement has been used to generate spin squeezed states [44, 33], and to perform sub-shot noise magnetometry [33, 49]. In the regime of negligible backaction that is of interest here, Smith *et al.* continuously monitored the Larmor precession of spin in an external magnetic field, and observed a series of dynamical collapse and revivals due to a nonlinear term in the spin Hamiltonian [72], which data was fit by our simulation routines as outlined in Sec. 4.5. While this nonlinear collapse limits

the observation window of a quantum nondemolition measurement, it also allows for full controllability of the atomic spin, as discussed in Sec. 4.4. In principle the control allows one to reconstruct the input quantum state according to the procedure described above. The ac Stark shift required for the nonlinearity also introduces a small but unavoidable amount of decoherence due to photon scattering. Quantum state reconstruction requires a large enough nonlinearity to generate dynamics that cover the entire operator space before decoherence erases information about the initial state. This explains our choice to reconstruct using the D1 transition rather than the D2 transition, as the nonlinearity per unit scattering can be up to five times larger using the former transition.

The full Hamiltonian, including the nonlinear AC Stark shift induced by an x-polarized probe and magnetic control field is Eq. (4.49)

$$H(t) = g_F \mu_B \mathbf{B}(t) \cdot \mathbf{F} + \beta_{\mathrm{NL}} \hbar F_x^2 \tag{5.35}$$

where $\mathbf{B}(t)$ is the control field and β_{NL} is the strength of the ac Stark shift. The ratio of the strength of the nonlinearity to the scattering rate is $\beta_{\mathrm{NL}}/\Gamma \approx 7.67$. The evolution of the ensemble is governed by the master equation

$$\mathcal{L}_t[\rho] = -\frac{i}{\hbar}[H(t), \rho] - \frac{\gamma}{2}\mathcal{D}[\rho], \tag{5.36}$$

where all excited states have been adiabatically eliminated, such that ρ has support only on the ground state of interest. The superoperator $\mathcal{D}[\rho]$ includes both the effects of decoherence due to optical pumping within the $F = 3$ manifold and the effect of loss due to optical pumping into the $F = 4$ manifold. The details of the simulation we use to find the measurements as a function of time for a given set of control fields $\mathbf{B}(t)$ can be found in Sec. 5.2.1. In addition to the measurement history one requires the signal to noise ratio of the experiment, which sets the absolute scale for the covariance matrix, and can be estimated from experimental data as shown in Sec. 5.2.2.

Using the simulated coarse grained measurement vectors $(O_i|$ for a given set of controls one $\mathbf{B}(t)$ one may explicitly construct the covariance matrix $\mathcal{R}$ using Eq. (5.16)

$$\mathcal{R} = \frac{\mathrm{SNR}^2}{F^2} \sum_i |O_i)\,(O_i| \tag{5.37}$$

and find its entropy using Eq. (5.18). Note that we use $SNR = NF/\sigma$ as it is the experimentally relevant parameter. Now we need to find the set of control fields $\mathbf{B}(t)$ that minimizes the entropy of the conditional distribution, and hence corresponds to the most accurate measurement of the system state. Solving the Bellman equation [**?**] analytically would provide such a solution. While in simple cases, such as for total spin $F = 1/2$ this could be accomplished, for our system with $F = 3$ a suitable closed form solution is not known. Lacking an exact solution we attempt to find an acceptable set of fields using a numerical search routine.

Numerical search is made difficult by the fact that every set of fields requires several integrations of the master equation to determine the entropy of the covariance matrix. Such integrations take on the order of minutes to accomplish. Given these constraints we wish to simplify the search routine as much as possible. The first obvious simplification follows from the fact that any two components of the magnetic field are sufficient to generate all rotations as noted in Sec. 4.4. As such we can restrict our fields to be in the $x - y$ plane without any loss of generality. Furthermore, we shall assume the field to have a fixed magnitude with Larmor frequency is $g\gamma_F B_0 =$ 17kHz for the simple reason that this is the largest field easily generated in the experimental setup we consider. The total experiment takes $4ms$ in so that the effects of inhomogeneous magnetic field strength can be ignored. More exactly, the complicated field pattern provides an effective spin echo in the observed signal as any inhomogeneities will tend to average out. The 13ms T_2 time for the inhomogeneous broadening will then negligibly contribute to the 4ms experimental signal. Then

simplified control fields have the form

$$\mathbf{B}(t) = B_0(\cos\theta(t)\mathbf{e}_x + \sin\theta(t)\mathbf{e}_y). \tag{5.38}$$

To further simplify we assume that $\theta(t)$ is frequency limited, with a highest frequency of 12.5 kHz, so that it varies only slightly slower than the carrier frequency of 17kHz. Then over the 4ms interval we only need 50 points to represent a sampled version of $\theta(t)$. These fifty angles form a compact description of the control fields. We interpolate between them using a standard cubic spline to obtain a smooth curve. The resulting waveform is inserted into Eq. (5.38) to obtain the actual control fields needed to drive the experiment.

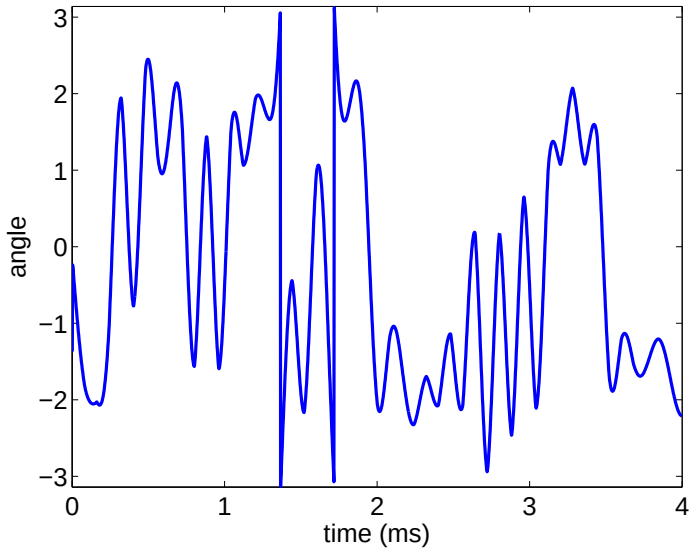

Figure 5.2:]
Angle that the control field make with the x-axis as a function of time for the nominal 4ms experiment. The fields presented are upsampled from 50 equally spaced points through the interval which are optimized using and iterative procedure described in the text.

We optimize the 50 control parameters using a numerical search routine. Initially we attempted a gradient descent algorithm, however the landscape is too rough, caus-

ing the algorithm to converge quickly to a poor local minimum. We also attempted a synthetic annealing algorithm, however the computational costs were prohibitive, due to the long time necessary for even a single function evaluation. We now use an iterative scheme in which a global search is performed upon each of the fifty angle variables sequentially to determine their best values. While a given angle is being optimized all the other angle variables are held fixed. The global search evaluates the entropy at 50 equally spaced angles then chooses coarse grained angle with the smallest entropy. This is done for all 50 angles, then a gradient descent over all 50 angle simultaneously is run to find the local minimum. This entire procedure is then repeated multiple times until the decrease in entropy is negligible. The procedure is seeded with an initial random field pattern; if desired performance is not achieved on can easily rerun the procedure with a different initial condition. The field angle as a function of time obtained from this procedure for the experimental conditions described in Sec. 5.2.2 and Sec. 5.3 is shown in Fig. 5.2.

Two important details have been left out of the above discussion. The first detail is the scattering rate used in the simulations. As noted the experiment is assumed to last for 4ms. This was the time window over which best control of the magnetic fields could be obtained in the experiment, resulting in the best agreement (lowest rms error) between the simulation and the experiment for known states. Using the above procedure we varied the intensity of the laser in the simulation, holding all other parameters fixed including the Larmor frequency and the measurement window. For a 4ms measurement window and an 17kHz Larmor frequency the intensity that corresponded to a scattering time of approximately $\tau = 4/3ms$ was optimal, producing the lowest entropy of the conditional distribution and hence the most accurate measurements. In the actual experiment the intensity of the probe laser was adjusted to achieve this rate.

The second detail is the measurement basis used during the reconstruction. For

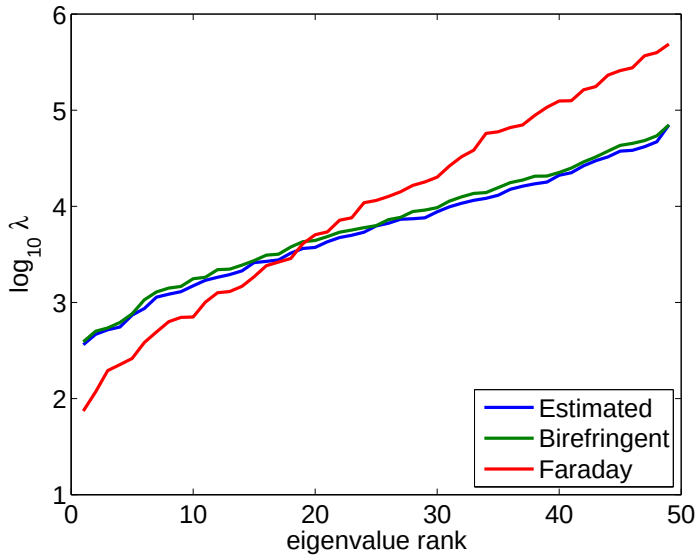

Figure 5.3: Eigenvalues of the covariance matrix for the D1 transition and generated using the control fields in Fig. 5.2 are plotted versus their rank for three distinct initial measurements. Employing a Faraday measurement (red) results in a larger overall signal, however the distribution is uneven, corresponding to worse exploration of the operator space. Using an initial circular measurement (green) produces a more even distribution with a better estimate obtained for the worst measured component. The actual measurement used for reconstruction in Sec. 5.3(blue) closely matches the birefringence measurement for performance.

an initial x polarized laser there are two independent choices. Fig. 5.3 plots the 48 eigenvalues of the covariance matrix obtained using the optimized control fields for both the Faraday measurement and the birefringence measurement. Each eigenvalue is proportional to the inverse of the variance for the measurement of one of the independent components of the initial state $\lambda = \frac{1}{\sigma_i^2}$. The Faraday measurement has a somewhat more uneven eigenvalue distribution corresponding to a less even exploration of the operator space. However over the full 4.0ms interval the performance of the two measurements is about equal, with the extra information due to the larger signal strength of the Faraday measurement making up for its slightly more uneven

coverage of the space. Experimental reconstruction time is limited to 1.5ms due to

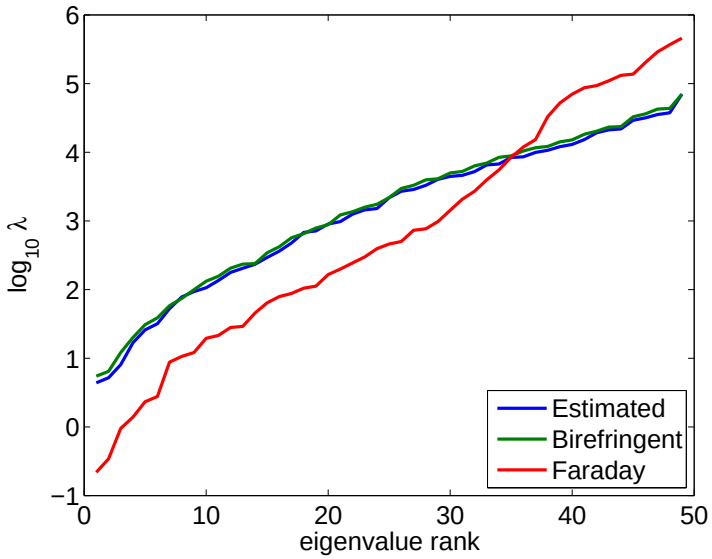

Figure 5.4: Eigenvalues of the covariance matrix for the D1 transition and generated using the first 1.5ms of the control fields in Fig. 5.2 are plotted versus their rank for three distinct initial measurements. This corresponds most closely to the covariance matrix used in the reconstructions presented in Sec. 5.3. Employing a Faraday measurement (red) results again in a larger overall signal, but in this case the distribution is significantly more skewed than over the full interval shown in Fig. 5.3. Here the birefringence measurement (blue) has much better overall performance due to its more even coverage of the operator space. Again the measurement used in the experiment (green) closely tracks the performance of the birefringence measurement.

uncertainty in the evolution parameters. The performance of the measurement over this interval depends strongly on which base measurement is chosen, as shown in Fig. 5.4. Here the better coverage of the operator space provided by the birefringence measurement more than compensates for the slightly stronger signal strength of the Faraday measurement. We see clearly that most of the eigenvectors are better measured using an initial birefringent measurement, and in particular the variance of the worst measured eigenvector is at least and order of magnitude smaller in the birefringent case. The reason for the better performance of the birefringent measure-

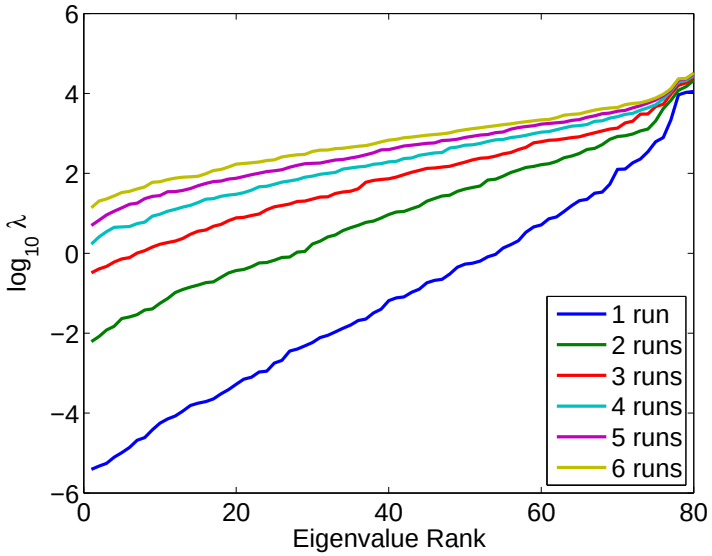

Figure 5.5: Eigenvalues of the covariance matrix generated for the D2 transition using a Faraday measurement are plotted versus their rank. A single run is seen to be clearly insufficient for reconstruction, with the worst measured eigenvalue having a variance orders of magnitude larger than the space of possible density operators. Only by including the results of several measurements using independent trajectories through the space can one hope to reconstruct the initial state.

ment is that we are relying on the nonlinear term in the Hamiltonian F_x^2 to move us around the space and the birefringent measurement $F_xF_y + F_yF_x$ effectively gets a head start over the Faraday measurement F_x as it is already second order in the atomic moments.

What if the nonlinearity had been insufficient to allow measurement of the entire space? An example of this case can be seen by considering reconstruction of the $F = 4$ hyperfine grounds state manifold using the D2 transition of ^{133}Cs in the far off resonant regime. Fig. 5.5 plots the eigenvalues of the covariance matrix associated with a Faraday measurement on this transition, which is the only measurement possible as the hyperfine splitting is insufficiently resolved in this regime to allow a

strong birefringent coupling. As can be seen a single run of this procedure measures some of the elements of the density operator orders of magnitude below what is necessary for reconstruction. In this case one needs to run the procedure using several distinct field patterns to obtain a useful estimate of the state. The iterative procedure described above for optimizing the control fields extends easily to the case of several independent runs. Performing this extension on finds that at least 5 or 6 runs exploring distinct parts of the operator space an required for a full reconstruction of the initial state.

5.2 Experimental considerations

An accurate simulation is essential in order to perform continuous measurement quantum state reconstruction. The goal of this simulation is to produce a measurement operator history $M(t)$ which accurately represents the experimental measurements performed upon the initial state ρ_0. An accurate simulation of our example system has three essential components: an accurate representation of the interaction with the light field, an accurate representation of the atomic evolution due to magnetic fields, and an accurate representation of the measurement. In addition to these requirements we also require an accurate estimate of the initial state of the system ρ_0 to check the accuracy of our procedure. In Sec. 5.2.1 we employ the results derived in Chap. 4 to produce a parameterized simulation that can accurately account for all of these necessary components. Sec. 5.2.2 then explores the various techniques we employ to to determine the simulation parameters that appropriately model the the experimental system under consideration.

5.2.1 Description of the simulation

This section provides a detailed description of the numerical methods used to simulate the dynamics of an alkali atom, and the parameters necessary to uniquely specify such a simulation. Throughout this chapter we work in the superoperator picture as this proves the most convenient method, and corresponds to the methods used in the actual simulation code demonstrated in Appendix B. In this picture our goal is to reproduce the set of measurement vectors $(O_i|$. To do this we first consider what the output signal would be for a given initial state $|\rho_0)$.

The assumption of weak measurements discussed in Sec. 5.1.3 allows us to drastically simplify the evolution that we need to simulated. This assumption implies that the individual atomic systems can be treated as uncorrelated such that each evolves separately. Then the evolution equation for the state of atom n in the superoperator picture can be written as

$$\frac{d}{dt}\left|\rho_n(t)\right) = \mathcal{L}_n(t)\left|\rho_n(t)\right), \tag{5.39}$$

with initial condition $|\rho(0)) = |\rho_{0n})$. The total N atom system state will then be

$$\left|\rho(t)\right) = \bigotimes_{n=1}^{N}\left|\rho_n(t)\right). \tag{5.40}$$

Each atoms contribution to the base measurement can be quantified by some measurement vector $w_n\,(O_n|$, which includes some coupling strength to the laser w_n , as well as any fluctuations in the measurement direction $(M_n|$. Then the simulated output signal will be

$$M(t) = \sum_{n=1}^{N} w_n\left(O_n|\rho_n(t)\right). \tag{5.41}$$

To determine this exact quantity we would need to simulate the evolution of each individual atom. However by making several simplifying assumptions we can approximate this quantity by simulating the expected value of a single measurement

on a single atom prepared in initial state ρ_0. To see what assumptions are necessary we formally solve Eq. (5.39) to give

$$|\rho_n(t)) = \mathcal{S}_n(t)\,|\rho_{0n})\,. \tag{5.42}$$

Then Eq. (5.41) becomes

$$M(t) = \sum_{n=1}^{N} (O_n|\, w_n \mathcal{S}_n(t)\,|\rho_{0n})\,. \tag{5.43}$$

We wish to approximate this equation by a single atom evolution and measurement corresponding to

$$M(t) = (O|\,\mathcal{S}(t)\,|\rho_0)\,. \tag{5.44}$$

Obviously we wish to have some type of average initial state, measurement and dynamic which will represent the mean measurement of the ensemble faithfully. There are several possible choices corresponding to how terms are grouped when averaging. We make the choice,

$$(O| = \sum_n (O_n|\,, \tag{5.45}$$

$$\mathcal{S}(t) = \sum_n w_n \mathcal{S}_n(t), \tag{5.46}$$

$$|\rho_0) = \sum_n |\rho_{0n})\,. \tag{5.47}$$

This ansatz neglects any correlations between the measurement direction of the atoms, the evolution of the atoms and the initial state of the atoms. Note however that we explicitly keep any correlations between the measurement strength and evolution, which is reasonable as both are correlated with the local intensity of the laser that the atoms see. The ignored correlations will most likely be small or nonexistent in the actual experimental apparatus, and to the extent that they are present can be neglected as variations in preparation and measurement basis are themselves expected to have magnitude $< 1\%$.

The averaged evolution $\mathcal{S}(t)$ is constructed by considering the evolution of a single atom then averaging over the observed distribution of atomic dynamics weighted by the probe strength. The procedure we use to determine the appropriate weighting distribution $w(\mathcal{L})$ is explained in Sec. 5.2.2. Single atom dynamics consists of an alkali probed by a polarized laser and subject to time varying magnetic fields as discussed in Chap. 4. The master equation can be broken up as the sum of four generators each with its own time dependent coefficient

$$\frac{d}{dt}|\rho) = [B_x(t)\mathcal{L}_x + B_y(t)\mathcal{L}_y + B_z(t)\mathcal{L}_z + s\mathcal{L}_s]\,|\rho)\,. \tag{5.48}$$

Here

$$\mathcal{L}_{x,y,z}(\rho) = -ig\gamma_F\,[F_{x,y,z},\rho]\,, \tag{5.49}$$

generate the dynamics associated with the appropriate magnetic field, while

$$\mathcal{L}_s(\rho) = \frac{i}{\hbar}\,[H_{\text{atom}} + H_{\text{int}},\rho] + \mathcal{L}_{\text{spont}}(\rho)\,, \tag{5.50}$$

accounts for the dynamics of the atom due to the laser, and is scaled by the saturation parameter,

$$s = \frac{\Omega^2/2}{\Gamma^2/4 + \Delta^2} \approx \frac{\Gamma^2}{4\Delta^2}\frac{I}{I_{\text{sat}}} \tag{5.51}$$

which scales with intensity I and depends upon detuning Δ, and the saturation intensity I_{sat} which is 1mW/cm^2 for cesium. Throughout we assume that each atom sees only a single laser intensity such that s is constant. To calculate the exact form of $\mathcal{L}_s$ we appeal to the results of Chap. 4. Specifically Eq. (4.11) provides the adiabatically eliminated master equation that we require to calculate $\mathcal{L}_s$ based upon the complex tensor polarizablitiy (Eq. 4.12) and the feeding terms (Eq. 4.13). These last two are calculated using the angular momentum algebra from Appendix C for the appropriate ground state and transition. The polarizability and feeding terms also depend upon several parameters, specifically the detuning, laser saturation, and

excited state linewidth. The excited state linewidth is a property of the atom used and can be readily obtained [**?**]. The detuning is experimentally calibrated Sec. 5.2.2, while the saturation parameter, s, is initially calibrated to 1 for a specific transition $gF \rightarrow eF'$, and subsequently fit to the experimental data using techniques described in Sec. 5.2.2. For the example system $F = 3$ while $F' = 4$. One should note that we treat the nonprobed hyperfine ground state, $F = 4$ in the example system, as a loss channel by neglecting any feeding terms that terminate in this manifold.

Given an explicit form for each of the generators in Eq. (5.48) we proceed to determine the single atom evolution superoperator $\mathcal{S}(t)$. This is done by assuming that the time variation of $B_{x,y,z}(t)$ is negligible on some short time scale Δt. For the example system we take $\Delta t = 2\mu s$. Then $\mathbf{B}(t) \approx \mathbf{B}_i$ during the interval $t \in [(i-1)\Delta t, i\Delta t]$. Then master equation (Eq. 5.48) is constant over that same interval and may be solved explicitly as

$$|\rho(i\Delta t)) = e^{\mathcal{L}_i \Delta t} |(i-1)\Delta t) \,. \tag{5.52}$$

This leads directly to a recursion relation for the single atom evolution operator

$$\mathcal{S}(i\Delta t) = e^{\mathcal{L}_i \Delta t} \mathcal{S}\left((i-1)\Delta t\right), \tag{5.53}$$

with initial condition $\mathcal{S}(0) = \mathcal{I}$. This recursion relation is then solved numerically, by explicitly exponentiating the constructed generator (Eq. 5.48) and carrying out the recursion. The averaged superoperator evolution is obtained by calculating the individual atomic evolution over a set of parameters, corresponding to variation in the magnetic fields $\mathbf{B}_i$ and the intensity s, then averaging over the appropriate weighting distribution as discussed in Sec. 5.2.2.

We parameterize the averaged base measurement as some linear combination of three independent possible measurements. To find these three independent measurements we again appeal to the results of Chap. 4. Specifically the we note that the measurement is generated by the same Hamiltonian as the atomic dynamics, except

instead of considering the effect of the field on the atoms we consider the effect of the atoms on the field, which produces a rotation of the stokes vector according to Eq. (4.36) which we reproduce here,

$$H_{\rm int} = -\frac{1}{4}\left[\alpha^{(0)}\left|\mathbf{E}\right|^2 + \overleftrightarrow{\alpha}^{(1)}\cdot\left(\mathbf{E}^*\times\mathbf{E}\right) + \alpha^{(2)}_{ij}\left(E^*_i E_j - \frac{1}{3}|\mathbf{E}|^2\delta_{ij}\right)\right]. \tag{5.54}$$

In the small angle approximation the initial measurement may be expressed as

$$M(t) = \langle\alpha_{ij}\rangle\,\epsilon_{ijk}A_k, \tag{5.55}$$

where ϵ_{ijk} is the Levi-Civita tensor, and A_k is a set of weights that specifies the measurement direction and whose value must be estimated. Again α_{ij} can be determined from Eq. (4.12).

The averaged initial state $|\rho_0)$ is the quantity which is estimated in the reconstruction procedure. Of course to check this procedure we require some independent determination of the value of ρ_0. Optical pumping [**?**] can result in the preparation of some initially well known initial state but this technique only works for a small set of possible states. To get a broader sample we consider allowing the system to evolve under some simple well known dynamic, such as the Larmor precession collapse-revival dynamic discussed in Sec. 4.5. The simulation code is then used to evolve the well known fiducial state using the estimated averaged dynamical map $\mathcal{S}(t)$, discussed above. This then provides a variety of initial states with which to test the procedure. Note that this procedure implicitly assumes that the initial state is uncorrelated with the dynamics, which assumption will break down for long state preparation as the evolution used to generate the state will be highly correlated with he subsequent evolution used to measure it. One minor wrinkle is that the initial state evolution must be run up to the time that estimation starts. Care must be taken to match the evolutions as closely as possible, so that no part of the evolution from fiducial state to the end of the procedure is unaccounted for, or, even worse, multiply counted. This can be done by assuring that the initial state preparation

terminates exactly at the end of a timestep δt, or as is done in the code, including any initial and final fractional evolutions necessary for appropriate boundary matching.

There is one final component to the simulation which consists of filtering the output signal. A digital fourth order Bessel filter with a variable pass band is used to remove excess noise. In the example system a $10-80$kHz filter is used. This filter is applied to both the data and the simulation so is not technically part of simulating the experiment. There is also a $.75-125$kHz prefilter which is used to simulated the actual analog filter present in the experiment, however the subsequent digital filtering to the tighter bandwidth obliterates any sign of this prefilter.

5.2.2 Calibration

In Sec. 5.2.1 we discussed the specifics of how the simulation works and determined several parameters that are needed to match the simulation to the experiment. We require an estimate of the magnetic fields seen by the atoms and their fluctuations, an estimate of the intensity of the laser and its fluctuations, an estimate of the laser detuning, and an estimate of the averaged measurement direction in order for the simulation to run and the reconstruction procedure to work. Additionally we require an estimate of one or more fiducial states in order to test the reconstruction procedure and an estimate of the experimental signal to noise ration (SNR) for use in the estimation procedure.

Some of these parameters can be directly determined using the experimental apparatus. Specifically, the detuning can be determined experimental by locking the laser to a resonant cavity [**?**]. Fiducial initial states are determined using optical pumping followed by a Stern-Gerlach measurement to determine the overall effectiveness of the pumping procedure. This then provides the eigenvalues of the density matrix along the pumping axis, which completely characterizes the initial state.

Other parameters currently must be fit based on post processing of the data. The desired method is to perform several calibration runs close to the time that the reconstruction procedure is being implemented. These calibration runs start with a specific fiducial state, in the example system this would be the stretched state along y such that $F_y |\psi\rangle = F |\psi\rangle$. The evolution consists of some simple dynamic, for our example system the dynamics consist of Larmor oscillation under a static field. The measurement direction of the calibration run would then be chosen based on what is to be calibrated, in our example system we can choose either the Faraday measurement of F_z which is well characterized, or the birefringence measurement $F_x F_y + F_y F_x$. One then fits the calibration runs by tweaking the free simulation parameters.

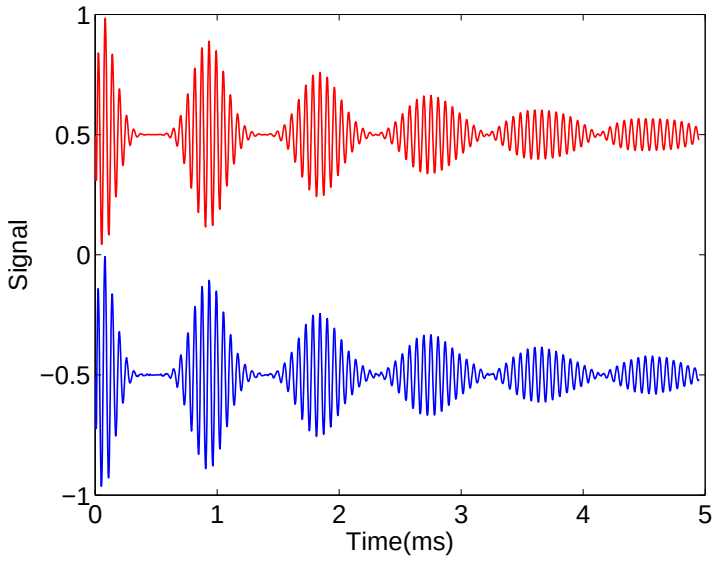

Figure 5.6: At bottom in blue is the data from the experimental calibration run used to fit the intensity distribution. At top in red is a simulation of the calibration run using the estimated fit parameters. The signal is in arbitrary units.

We first attempt to find the intensity distribution corresponding to the number of atoms which see intensity s weighted by their measurement strength, as required

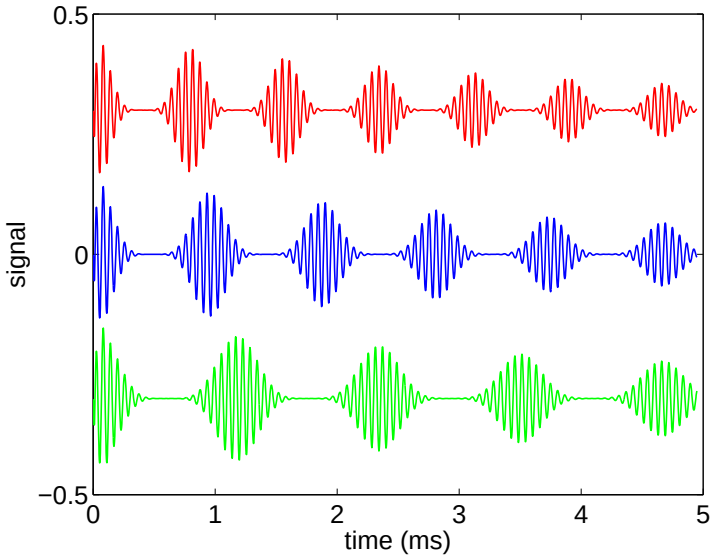

Figure 5.7: Simulations run at three distinct laser intensities, corresponding to 120% of nominal laser intensity (red), 100% of nominal laser intensity (blue), and 80% of nominal laser intensity (green).

for the simulation in Sec. 5.2.1. To do this we consider a calibration run having a constant x magnetic field and measured using a Faraday probe, just as was used in Sec. 4.5. The resulting Larmor precession and nonlinear collapse and revival behavior is shown in Fig. 5.6. A set of 20 simulations using the same parameters is then run with field intensities that vary from 80% to 120% of nominal intensity Fig. 5.7. A local optimization is performed to determine the distribution over these simulations which most closely matches the observed signal Fig. 5.6. When the estimated Larmor field is so far off that the simulation and experiment are 180° out of phase after only one or two milliseconds interference between the two signals artificially amplifies the rms error at this time leading the optimization to compensate by introducing excess inhomogeneity. To combat this problem we fit the Larmor frequency to remove the possibility of interference effects. The intensity distribution is characterized by its first three moments, a mean, a width and a skew. Inclusion of higher

moments just leads the routine to attempt to fit the intensity distribution to any idiosyncrasies in the calibration data wasting time and producing fragile results. One such distribution is depicted in Fig. 5.8. The results of using this distribution to simulate the experiment are depicted in the simulation from Fig. 5.6. In addition to fitting the distribution in intensities we also estimate an overall scaling which provides an estimate of α in Eq. (5.9) and estimate an overall decay constant β such that $M(t) \rightarrow e^{-\beta t} M(t)$. The constant β captures and other decoherence mechanisms, such as magnetic field inhomogeneity or atom loss from the sample. We find an that the additional decoherence time is $1\beta \approx 13$ms, which is substantially longer than the 4ms experiment. Furthermore this decoherence is mainly due to magnetic field inhomogeneity which has a much smaller effect upon the reconstruction runs than on the Larmor precession runs due to the constantly changing magnetic fields in the former which effectively provide a spin echo like effect. Thus we can ignore an additional decoherence in the simulation when considering the reconstruction procedure. The averaged evolution operator $\mathcal{S}(t)$ will then just consist of the evolution calculated in Sec. 5.2.1 summed over the the estimated scaled intensity distribution Fig. 5.6. Note that the estimation procedure naturally weights the distribution to account for the measurement strength on the individual atoms, as we perform the estimate using an actual output signal from the experiment.

One technical point about the measurement scaling has been glossed over. The estimated scaling α has a 1% uncertainty due to fluctuations in the number of atoms in the ensemble. To account for this scaling we estimate the unnormalized state which has $\mathrm{Tr}\left[\rho\right] = \alpha$. This is done exactly according to the procedure outlined in Sec. 5.1.2, except that the zero variance measurement of $\mathrm{Tr}\left[\rho\right] = 1$ is replaced by the actual measurement $\mathrm{Tr}\left[\rho\right] = \langle\alpha\rangle$ with a standard deviation of .01 obtained from the calibration procedure. The effect of this substitution is to allow the positivity constraint to provide additional information about the scaling in conjunction with the other measurement results. We then normalize $\bar{\rho}$ to obtain the actual estimate

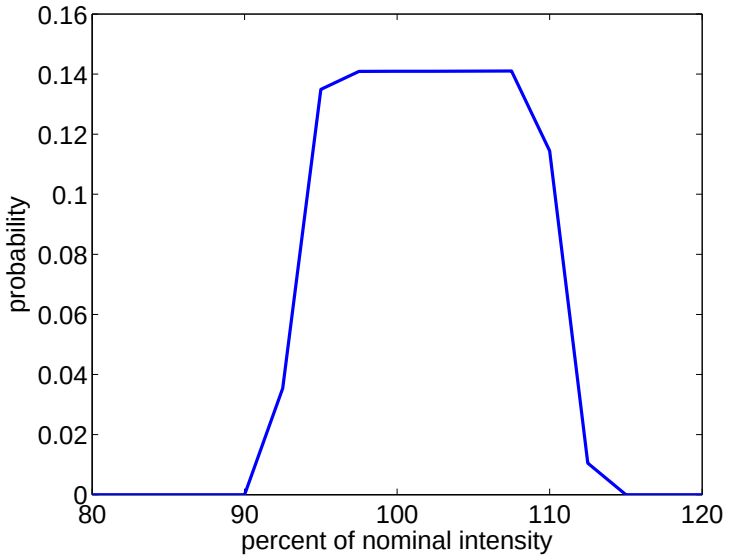

Figure 5.8: One possible intensity distribution estimated from the Larmor calibration run data shown in Fig. 5.6. Note that this distribution is not unique; any compact distribution with the same first three moments would suffice.

of the initial state.

Though we have determined that it is suitable to assume zero variance in the magnetic fields we still have not specified the mean of these fields $\mathbf{B}(t)$ whose specification is necessary to construct $\mathcal{S}(t)$. The magnetic fields are generated by a set of induction coils which are in turn driven by a time varying voltage. We use the time varying voltage, filtered by the experimentally determined coil response function, to estimate the magnetic fields. Additionally some experimentally measured background magnetic fields are added. In order to use the current, of course, we need to synch the driving fields with the output signal. This is done by considering the calibration run used to estimate the intensity inhomogeneity once again. Only the first $500\mu s$ of these runs are considered, and a two parameter fit is performed, matching any offset between the data time stamp and the driving field time stamp at

the same time as estimating the Larmor frequency. These must be performed simultaneously as the estimated offset between driving fields and observed signal depends strongly on the applied Larmor frequency. The estimated Larmor frequency should also allow us to calibrate the amplitude of the magnetic field for a given drive which we term the magnetic field scaling. Unfortunately this scaling varies on a timescale of minutes, making one time estimation problematic. Due to this fast fluctuation, we require an independent estimate of the scalings for both the x and y driving fields for each reconstruction.

We obtain scaling estimates for the magnetic fields by using the actual reconstruction data for calibration. This is possible because miscalibration of the fields by any significant margin results in a waveform that could not have been generated by any initial state. Alternatively the perturbation of the waveform due to field miscalibration is orthogonal to that due to changing of the initial state.

To make use of this observation we generate a grid of waveforms over a set of possible scalings for the x and y fields, from 99% to 101% of its nominal value, with spacing .2%. Then full reconstruction is run using each of these possible scalings, and the rms error of the result is calculated. The reconstruction which reproduces the observed experimental signal with the smallest error is then used to give an estimate of the state and of the fields. It must be emphasized that no outside knowledge of the initial state is used in this procedure. Currently a slightly faster procedure is used in the code reproduced in Appendix B. which uses a gradient search over the grid, rather than the global search described here. Fig. 5.9 graphically demonstrates this procedure for three possible fields, one can clearly see that the signal based upon a reconstruction using the appropriate fields is a much better match for the observed data than the signals based upon inappropriate field scalings. The field scaling estimated from the reconstruction is also used for purposes of calculating the initial state evolution as discussed in Sec. 5.2.1.

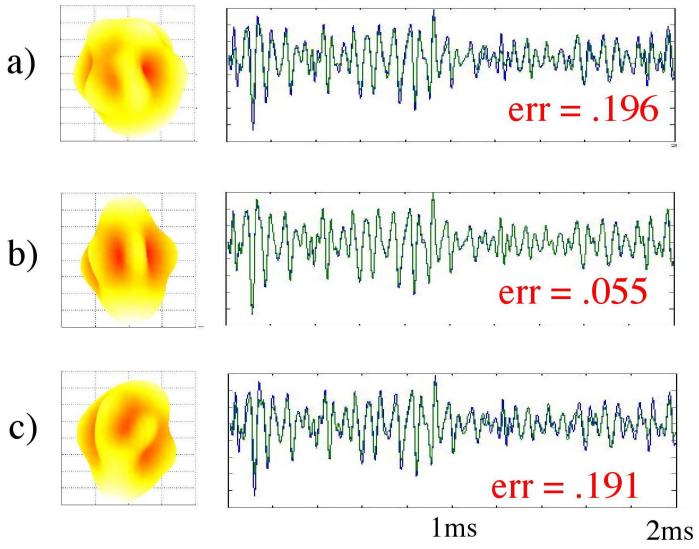

Figure 5.9: Demonstration of errors due to magnetic field miscalibration is shown. At top a state is reconstructed using a simulation with fields that are 1% high, while at bottom a state is reconstructed using a simulation which assumes fields that are 1% low. At center is the reconstructed state using the best estimate of the experimentally applied fields. The spherical Wigner functions (Eq. 5.56) of the reconstructed states at top and bottom are clearly wrong. Furthermore a signal simulated using these misestimated states has a much poorer agreement with the observed data then the the correct signal does.

Now we must form an estimate of the average measurement direction, corresponding to A_k in Eq. (5.55). To obtain this, we employ two additional calibration runs with magnetic fields in the x and z directions. Both start in the same optically pumped initial state $F_z |\psi_0\rangle = F |\psi_0\rangle$, and both are measured in the nominal birefringent basis. These two runs together determine the actual measurement basis of birefringent measurement, which is not purely circular as it contains some small percentage of contamination from the Faraday basis. Comparing the measured signals to a simulation using the known intensity inhomogeneity calculated from the first calibration run allows extraction of the actual measurement basis using a linear fit. While we technically require all three components of A_k, we can immediately

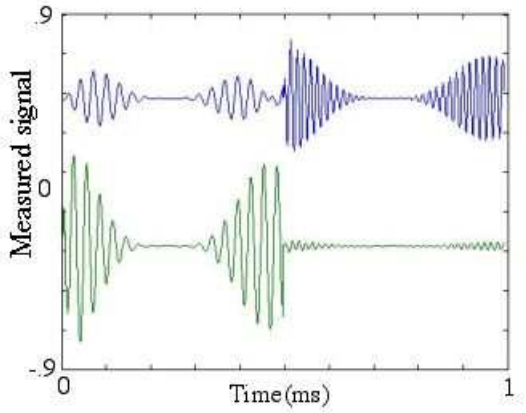

Figure 5.10: Shown are two composite signals corresponding to a pure birefringence measurement (top in blue) and a pure Faraday measurement (bottom in green). The first .5 ms are obtained from a Larmor precession experiment with an x bias field. The second .5 ms are obtained from a Larmor precession experiment with a z bias field.

rule out one due to having a linearly polarized input probe laser, such that we only need estimate the two remaining coefficients corresponding to pure Faraday and pure birefringent measurement. Example data from this fitting procedure is shown in Fig. 5.10 and Fig. 5.11. Fig. 5.10 shows the two basis measurements corresponding to the two linearly independent components of the stokes vector that can be measured. Fig. 5.11 shows the observed experimental signal and the best linear fit to this signal corresponding to the experimental measurement direction, which can have norm less than one indicating that there is some loss due to the waveplate that implements the measurement.

Finally we may extract the signal to noise ratio of the experiment by subtracting the observed experimental signal from the simulated signal for a well characterized evolution. Assuming the model is sufficiently accurate this will result in a white noise process, whose variance is easily measured.

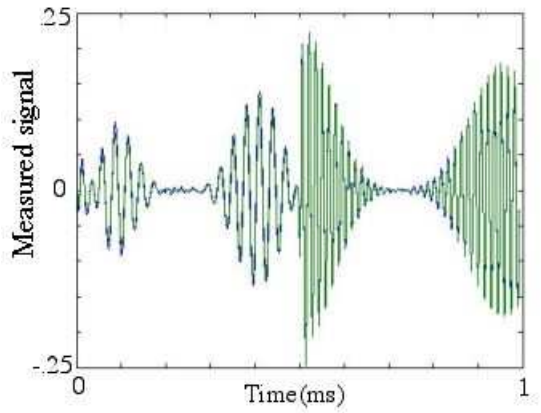

Figure 5.11: In green is shown the experimentally measured composite signal constructed the same ways as described in Fig. 5.10. Overlaid in blue is the simulated signal corresponding to .13(Faraday) + .85(Birefringence) which provides the best linear fit to the observed data. Note that the signal is slightly subnormalized due to losses in the waveplate used to experimentally implement the birefringence measurement.

5.3 Experimental results

This section presents a collection of experimental results using the continuous measurement quantum state reconstruction technique. These results are all for reconstruction of the $F = 3$ ground state hyperfine manifold of ^{133}Cs, using a measurement of an initially linearly polarized laser probe tuned $\Delta = 545$ MHz below the $S_{1/2}F = 3 \rightarrow P_{1/2}F = 4$ transition and measured in the circular basis. In all figures states are represented by their spherical Wigner distributions [24]

$$W(\theta, \phi) = \sum_{l,m} C^*_{l,m} Y^{(l)}_m(\theta, \phi) \quad C_{l,m} = \mathrm{Tr}\left[T^{(l)}_m \rho\right] \tag{5.56}$$

with $T^{(l)}_m$ the standard spherical tensor operators [61]. An example of a spherical Wigner distribution is given in Fig. 5.12. All displayed signals, both experimental and simulated, are filtered using a digital band pass filter with passband 10kHz to 80kHz, additionally the simulated data is prefiltered with a $.8 - 125$ kHz band pass

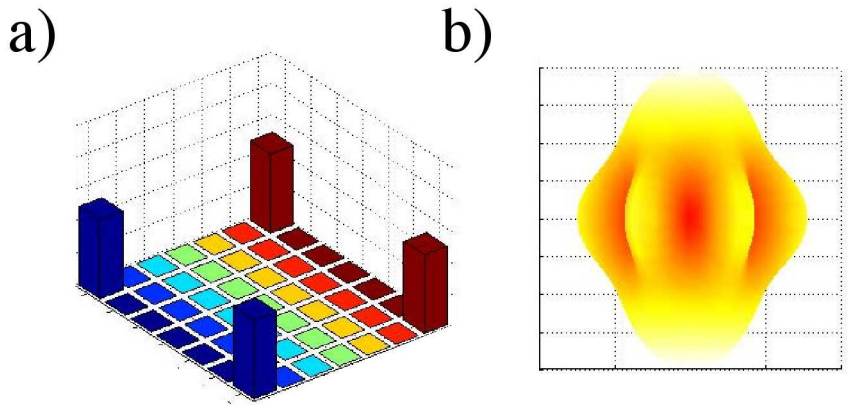

Figure 5.12: Two graphical representations of the spin cat state, which is a coherent superposition of maximal spin up and maximal spin down $|\psi\rangle = (|F = 3, m_F = 3\rangle + |F = 3, m_F = -3\rangle)/\sqrt{2}$, are shown. a) A bar plot of the real part of the density matrix, which shows the characteristic coherences of a cat state. b) A spherical Wigner plot [24], showing the two main peaks at top and bottom and oscillatory interference fringes around the equator. The red portion indicate where the Wigner function is negative. The plot is made as $1 + W(\theta, \phi)$ using the formula for W from Eq. (5.56).

digital Bessel filter, to simulated the analog filter present in the experiment. All reconstruction are performed using these filtered signals, to remove extraneous high and low frequency noise.

The performance of the procedure as a function of time for several initial states is demonstrated in Fig. 5.14, Fig. 5.13, and Fig. 5.15. Specifically Fig. 5.13 shows the fidelity of reconstruction for a coherent spin state $|\psi\rangle = |F = 3, m_F = -3\rangle$, i.e. the state produced by optical pumping of the sample with a y bias field. Fig. 5.14 shows the fidelity of reconstruction for a state which is initially optically pumped and then undergoes Larmor precession which stops midway through the first collapse. This state is closely resembles the spin "cat state" from Fig. 5.12 which is a superposition

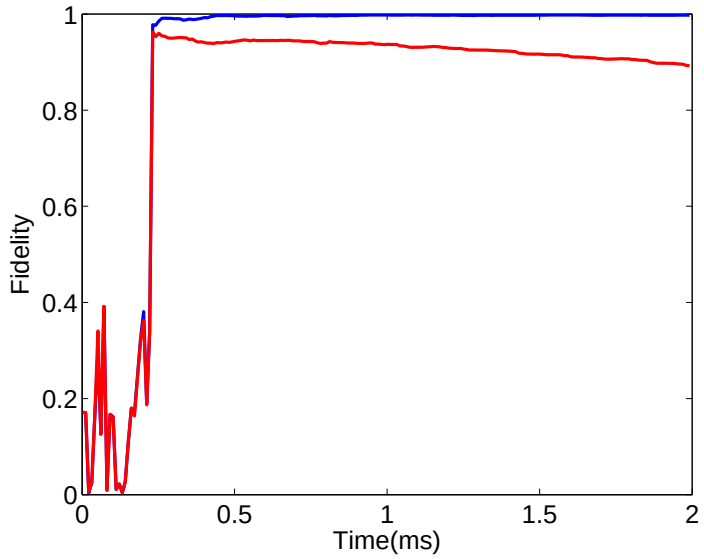

Figure 5.13: The fidelity of the originally optically pumped state $|\psi\rangle \approx |F = 3, m_F = 3\rangle$ with the initially prepared state as estimated by a stern-gerlach apparatus versus time. For a given time the fidelity presented is for the best estimate of the initial state using the data acquired up to and including that time. The initial erratic behavior is due to nonconvergence of the estimation algorithm as discussed in Sec. 5.1.2. The red line indicates the experimentally obtained fidelity while the blue line is the fidelity obtained using a simulation with the same parameters. At the time of estimation,1.5ms, the fidelity is $F = .92$.

of maximal projection of angular momentum along $\pm z$,

$$|\psi\rangle = \frac{1}{\sqrt{2}} \left(|F = 3, m_F = -3\rangle + |F = 3, m_F = 3\rangle \right), \tag{5.57}$$

with fidelity $F = .87$. Fig. 5.15 shows the fidelity for reconstruction of an unpumped atomic ensemble which closely resembles the maximally mixed state $\rho = I/7$. In all three of the reconstructions one clearly sees the transition due to convergence of the semidefinite programming routine at around $250\mu s$.

The spin coherent state Fig. 5.13 and the cat state Fig. 5.14 quickly saturate to their maximum fidelity while the mixed state Fig. 5.15 takes longer to achieve

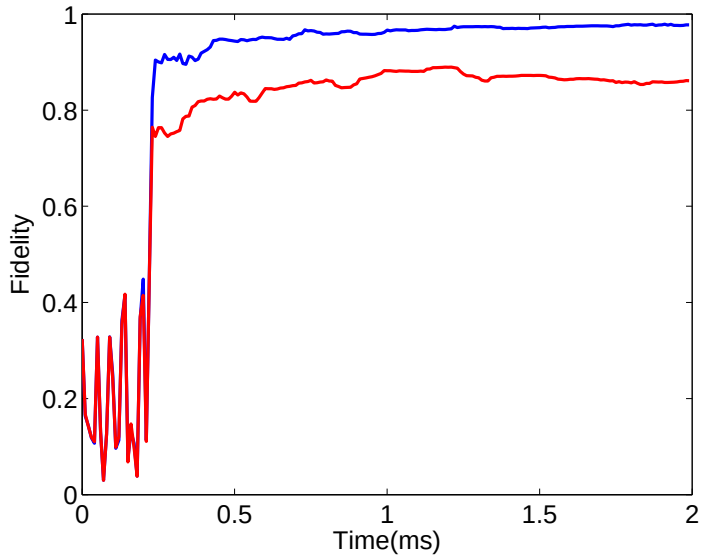

Figure 5.14: Same plot of fidelity vs. time as in Fig. 5.13 except for an initial state $|\psi\rangle \approx (|F=3, m_F=3\rangle + |F=3, m_F=-3\rangle)/\sqrt{2}$. This state was obtained by evolving an initially optically pumped state using Larmor precession to half way through the first collapse. We term this state the cat state as it is a coherent superposition of maximal projections along $\pm\mathbf{e}_z$. The actual state has some decoherence which is accounted for. The red line indicates the experimentally obtained fidelity while the blue line is the fidelity obtained using a simulation with the same parameters. At the time of estimation,1.5ms, the fidelity is $F = .87$.

a good estimate. This is a direct result of the action of the positivity constraint. Perturbing a pure or almost pure state by even a small amount can create negative eigenvalues of the density matrix, implying that such perturbations are ruled out by the positivity constraint as unphysical. Thus for pure states the positivity constraint provides a great deal of useful information which can help reconstruct the state more exactly. On the other hand the maximally mixed state has a ball of positive states around it. This can be proved by noting that the addition of any traceless operator O to the maximally mixed state $\rho = I/7 + O$ will result in a positive state if and only if O has all eigenvalues greater than $-1/7$. A sufficient condition for

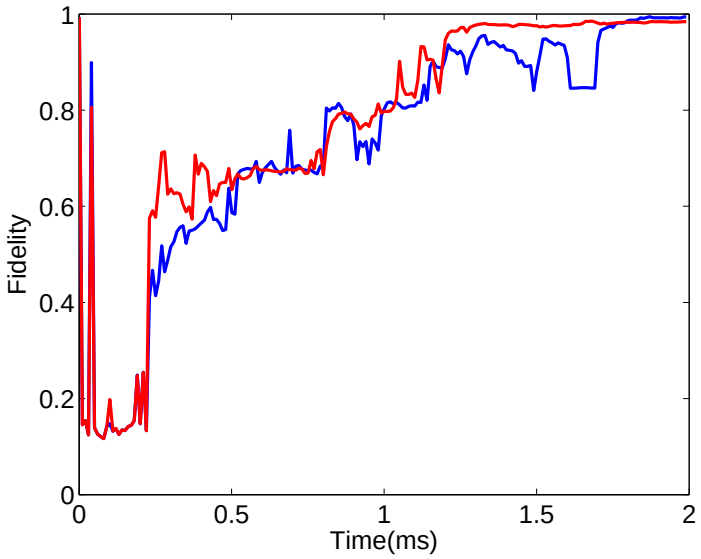

Figure 5.15: Same plot of fidelity vs. time as in Fig. 5.13 except the initial state is prepared without optical pumping, and so approximates the maximally mixed state $\rho \approx I/7$. The red line indicates the experimentally obtained fidelity while the blue line is the fidelity obtained using a simulation with the same parameters. At the time of estimation,1.5ms, the fidelity is $F = .98$.

this is that $\sqrt{\mathrm{Tr}\left[O^2\right]} \leq 1/7$, such that any perturbation with magnitude less than this will result in a positive state. In this case the positivity constraint provides no information which can help in the reconstruction, and one must rely solely upon the measurement history. Thus the mixed state is the most difficult state to reconstruct. Since the initial state is presumed to be unknown the procedure must be run for at least the time necessary to reconstruct the maximally mixed state $\rho = I/7$, which is about 1.5ms for this system.

Theoretically it is always better to run the reconstruction for a longer amount of time, as the increased number of measurements should always produce a more accurate state estimate. This can be seen in the results of a simulated reconstruction Fig. 5.14 of the same cat state which was reconstructed experimentally. One

notes that the fidelity generally increases as a function of time. This is true of all simulations. In the equivalent experimental results the fidelity begins to decrease markedly at later times. This decrease is characteristic of parameter miscalibration, indicating that the observed measurement signal does not correspond to the atomic measurement predicted by the simulation. The measurement thus provides misinformation about the initial state of the system, which misinformation corrupts the state estimate taking it further from the actual initial state. The most likely candidate for the miscalibrated parameters are the magnetic fields. Errors in the simulation will tend to degrade the accuracy of later measurements most, as the exact component of the density matrix measured at time t depends upon the full evolution from the initial time. As such it behooves us to end the reconstruction procedure as soon as possible. The optimal time to stop is when the worst measured state, i.e. the maximally mixed state, has achieved its maximum fidelity of reconstruction. As noted earlier this occurs at about 1.5 ms, where a characteristic fidelity of $90\% \pm 5\%$ is achieved for all initially prepared states.

Plots of some experimentally reconstructed states at this time are shown in Fig. 5.16 along with the corresponding initial states, and both the experimental and simulated measurement signal.

5.4 Summary

We have presented a new protocol for quantum state reconstruction based on continuous measurement of an ensemble of N members and demonstrated our procedure through a simulated reconstruction of a spin F via polarization spectroscopy of a gas of cold atoms. The reconstruction technique is nondestructive and exploits classical estimation theory, providing a starting point for consideration of more complex applications of quantum control tasks such as quantum feedback. An experimental

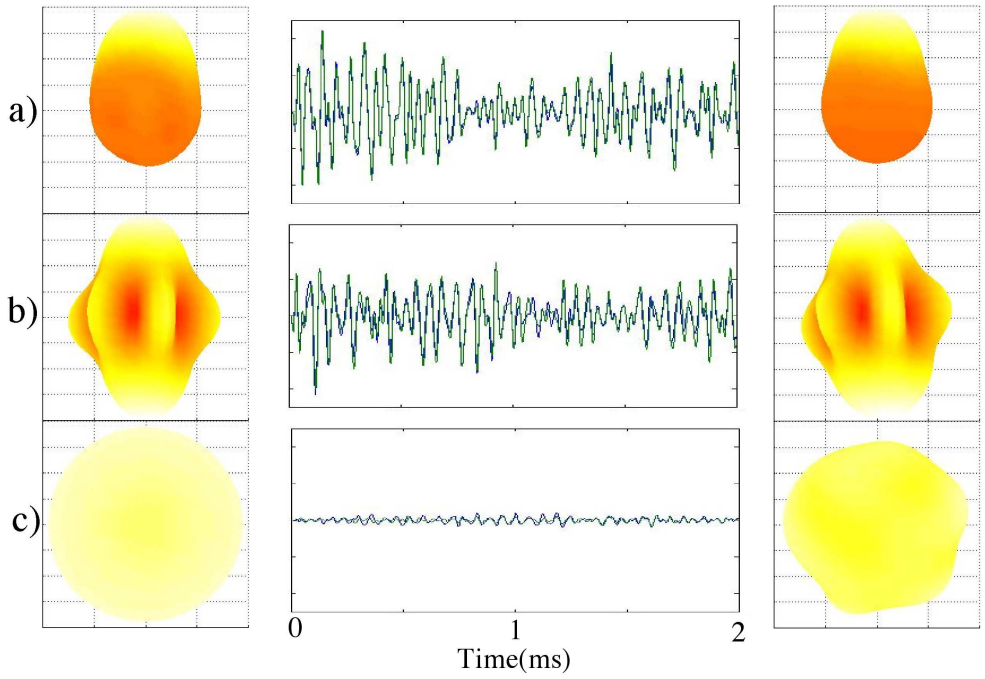

Figure 5.16: Reconstructions of several initial states. On the left is the initial state estimated by Stern-Gerlach, and possibly including some simulated evolution. In the middle is the observed experimental signal in green and the simulated signal using the best fit state in blue. On the right is the best estimate of the initial state at 1.5ms. From top to bottom the initial state are a) the stretched state $|\psi\rangle \approx |F = 3, m_F = 3\rangle$, b)the cat state $|\psi\rangle \approx (|F = 3, m_F = 3\rangle + |F = 3, m_F = -3\rangle)/\sqrt{2}$, and c)the maximally mixed state $\rho \approx I/7$. The fidelities of the reconstructed states are $F = .87, .92, .98$ respectively.

demonstration of the technique performed by our collaborators in Tucson, and employing the simulation code presented in Appendix B was presented. Comparison with theoretical reconstructions demonstrates that the limiting factor is uncertainty in the experimental evolution parameters.

Interesting behavior of the estimate as a function of time was observed due to the interplay of the measured information and the positivity constraint. Exploring this interaction more deeply should provide insight into the general state estimation

problem. One can also consider allowing for additional prior information in the reconstruction procedure. Such additional information should allow ever more accurate state estimation without the need for better control over the experimental parameters, and provides a fruitful avenue for future research. Currently our experimental collaborators in Tucson are considering methods for improving the experiment by either reducing the control magnetic field errors or replacing the magnetic controls with rf controls which are easier to manipulate. Additionally we are looking into the possibility of using microwave fields to generate the nonlinear term in the evolution, so that we can decouple the rate of control from the decoherence rate, allowing for experiments that explore the space much more uniformly.

Chapter 6

Summary and Outlook

This dissertation has attempted to cover the ground from the very basics of the light atom interaction discussed in Chap. 2 to the complicated engineering necessary to perform quantum state tomography using that interaction in Chap. 5. Throughout we have attempted to portray a unified picture of the electromagnetic field carrying information away from the atom, which information is gained through the basic dipole Hamiltonian $H = -\mathbf{E} \cdot \mathbf{d}$ which governs their interaction. Whether this information is ignored or measured, the information and the interaction which generated it have some effect upon the atomic system which must be accounted for.

Ignoring the results of the measurement results in decoherence of the atom. For a perfect resonant laser pulse this decoherence occurs at exactly the same rate as spontaneous emission into the subset of field modes spanned by the laser. For other initial states of the field, one finds that the decoherence changes depending on the initial state of the field and the atom. Specifically for a single photon field state, one finds that rabi flopping is impossible due to the decoherence but that the decoherence rate has no simple form. One can also achieve a variable decoherence rate by considering off resonant excitation of a degenerate ground state, such as is obtained through and

induced dipole interaction. In such a case the rate of decoherence depends upon the power in the laser.

Given these results we considered the possible uses for the information extracted from the atom by the laser probe. Specifically one could ask what is the entanglement that is generated between the atom and the probe, and is it enough to be useful in some of the entanglement based information protocols. In free space we saw that the entanglement generated between the single mode that contains the laser and the atom is small due to decoherence into the other modes. Furthermore, the entanglement between the atom and all modes spanned by the laser could be bounded above and was likewise always small, having a maximum several orders of magnitude below any useful level. This was because paraxial beams couple poorly to the mode into which atoms absorb and emit. In order to attain any appreciable entanglement one must consider a mode which strongly overlaps with the dipole mode that couples to the atomic system.

Alkali atoms provide an testbed system for exploring further interaction with lasers. These atoms contain ground state structure which allows for nontrivial interaction with the laser field, corresponding to the ac-Stark shift. Exploring this interaction we found a tensor decomposition which induces a quadratic level shift in a ground state of the alkali atom with total angular momentum F. This interaction, along with the addition of time dependent fields was seen to allow full control of the spin F subsystem. Furthermore the tensor interaction directly determined the components of the spin which could be observed with a polarimetry measurement of the output field. An example of dynamics observed using one such measurement, the Faraday measurement, exhibited interesting collapse and revival behavior. This behavior could be controlled by altering the angle of the magnetic field used to drive the system, increasing the speed of the initial collapse, or removing the collapses and revivals completely, leaving only Larmor precession and spontaneous emission decay.

Finally we considered how to use the information extracted from an ensemble of atoms all initially prepared in the same state and interacting with the same laser probe, to determine what that initial state was. We saw how an exacting simulation of the atomic dynamics was necessary to implement the resulting continuous measurement tomography procedure. Additionally we showed how to construct such a simulation based upon the theory expounded in Chap. 4 and how to account for inhomogeneities in this simulation. We saw how a Bayesian filter can be used to optimally estimated the state, including both the information gained from the measurement probe and the prior information that the initial state must have been some admissible physical state, represented by a physically allowed density operator. Finally we saw an example of how this procedure functions in practice.

The in depth exploration of the interaction of lasers and alkali atoms in this dissertation forms a starting point for much possible future research. The simulations developed in this thesis for a laser interacting with cesium are currently being employed to examine arbitrary state preparation of a spin $F = 3$ system. Using the same code extensions to the generation of arbitrary unitaries are also possible. The simulations can also play a key role in experimental considerations of quantum chaos. The tensor decomposition of the interaction Hamiltonian in Sec. 4.3 clearly demonstrates both the rotations and twist terms necessary for an experiment on the quantum kicked top, and the 9 levels in the upper hyperfine manifold could allow such an experiment to see remnants of the classical phase space of the kicked top in the quantum dynamics.

Extensions of the simulations presented here to include both ground state manifolds, $F = 3$ and $F = 4$, and new interactions open up another set of interesting possibilities. There are currently plans to explore controllability over the full ground state manifold of cesium. Such work could be greatly enhanced by detailed simulation of the processes involved along the lines of what was performed in Chap. 4.

Furthermore use of microwaves and radio waves for control over the full ground state manifold can allow for more exacting control than is possible with magnetic fields, and can break the tie between the strength of the quadratic term needed for full controllability of a single spin and decoherence. This could allow for much better implementation of any of the procedures discussed in Chap. 4 and Chap. 5 of this dissertation. Explorations of quantum chaos over the full sixteen level cesium ground state would provide an exciting opportunity to explore quantum to classical correspondence. The natural bipartite nature of the space, as a tensor product of atomic an nuclear spin, allows one to explore questions about the connection between entanglement generation in quantum systems and chaos in the corresponding classical system [48].

There is no reason to restrict attention to separable states of the atomic ensemble. Considering correlations among the atoms provides a fruitful area of extension for this work. One can consider squeezed states such as we have repeatedly alluded to through this dissertation. Up till now such squeezing experiments have taken place using standard Faraday measurements. There is no reason, however, that using the techniques discussed in this thesis, that squeezing cannot be performed using a different measurement, such as birefringence, or that it cannot be mapped onto some higher moment of the atomic distribution corresponding to squeezing of some other variable, say a third order moment $\sum_i F_x^3$. One could even conceivably squeeze multiple commuting variables simultaneously, producing interesting states. Placing the atoms in a cavity once could quantize the light field allowing excitations to be exchanged between the quantized stokes vector and the net quantized atomic variables. Such a system would provide a unique opportunity to examine a fully quantum system in the large action limit. Quantum chaos experiments on such a system would provide a complement to the experiments on single atoms discussed earlier, exploring the quantum to classical transition in a mesoscopic regime. Measurement of such a system, either through the probes discussed in this dissertation or otherwise

could produce interesting two mode squeezing between the atomic variables and the quantized field polarization.

One can also consider many body states that are not treated as an ensemble of spins, but rather make use of correlations between generated by backaction between the two hyperfine submanifolds of the cesium ground state. Currently Poul Jessen's lab is exploring squeezing of the clock transition using a birefringence measurement. One could generally consider squeezed states that span both manifolds or even more generally quantum correlated states. One possible use of this would be to use an entangling measurement to project a system of two cesium atoms into a two dimensional subspace with total angular momentum 0. If one uses the subspace formed by the angular momentum zero sums of both upper hyperfine manifolds $4 + 4 = 0$ and both lower manifolds $3 + 3 = 0$, then the resulting states will be split by twice the clock frequency, and will be insensitive to magnetic fields perturbations, making a near perfect clock. Of course with such precise control of the individual atomic spins one could also consider making an atomic computer. For such a computer continuous measurement could help with state preparation, ancilla preparation and error correction.

As measurement and control in quantum systems becomes more precise the possibilities for feedback will abound, allowing one to create ever more complicated states in ever larger systems. The possibilities for control of the many body spin state of an ensemble of atoms are just starting to be explored. Open loop control could allow one to generate highly nontrivial states based upon some combination of measurement backaction and system dynamics, using much the same techniques employed for the continuous measurement reconstruction. Closed loop feedback procedures currently employ simple gaussian approximations. It is possible that one could make more sophisticated approximations, perhaps even a simulation along the lines of that discussed in Chap. 5 that employs from two to a handful of represen-

tative atoms which correctly mimic the collective dynamics of the system. Such a simulation would ideally be able to account for the minimal amount of backaction which is observed in current experiments with the approximations necessary in the current gaussian schemes [76].

The continuous measurement tomography procedure also offers opportunities to implement full state based feedback upon the estimated state. Using the information gained one could attempt to control the initially unknown state transforming it arbitrarily. One could also attempt to use feedback during the state estimation procedure to improve the speed of convergence, or to dynamically adjust for fluctuating parameters.

More generally, the continuous measurement tomography procedure can be extended in several ways. By including information about the spectrum of the state to be estimated one can improve the estimate, at the cost of requiring additional computation. One could try to estimate states that have some small amount of initial correlation, which should be possible as there will still be many copies of that small amount of correlation (alternatively the state should still maintain sufficient symmetry that its form will be restricted). Of course this would require more parameters, and hence a more complex evolution, involving multi atom dynamics, i.e. collisions. One may also generalize the procedure readily to other systems, with the one caveat being that a sufficiently accurate simulation is necessary in those systems for the procedure to function.

Extensions of the work on decoherence from Chap. 2 and of the entanglement calculations made in Chap. 3 could include many avenues of future research. Considerations of how to engineer pulses to better couple to the atoms, and specifically how one could engineer a single photon pulse that would excite the atom with unit probability are possible. Considerations for increasing atomic coupling to specific field modes in free space are also conceivable. For example one could consider plac-

ing the atoms on a lattice, in which case the lattice structure selects specific directions to which an atomic ensemble would couple preferentially, which result classically in Bragg scattering. Many people are attempting to generalize entanglement measures to more systems, with some success, which would allow the work in Chap. 3 to be extended and refined. Finally both measurement strengths and entanglement can be investigated in new an novel systems, where one can ask questions about the decoherence induced by controls in those settings, as well as the possibility for useful entanglement generation.

Appendices

Appendix A

Entanglement code

This is the code used to calculate the entanglement generated between an atom and a laser in free space. Four different types of entanglement are calculated, as described in Chap. 3. The exact entanglement between the symmetric laser mode and the atom is calculated in `sym_tangle.m`. An upper bound to the full entanglement of the atom and all field modes spanned by the laser is calculated in `traj_tangle.m`. Finally a simplified calculation using a closed system model is performed with and without decoherence in `simple_tangle.m` and `dec_tangle.m`.

---

batch_run.m

File where the parameters for the run are set, and which calls the various evolution subroutines. `out, symout,trajout` and `decout`, contain the tangle as a function of overall scattering $D = \Gamma\tau$ and initial state, for the simple, symmetric, full, and simple with decoherence calculations respectively.

```
s = 1./sqrt(2);
%initial conditions, two element state vectors
ic = [0 1
    1 0
    s s
    s -s
    s i*s
    s -i*s];
ic = ic.';
A= 1000; % area of the beam in units of the scattering crossection
f = 0.1; %fraction of a not gate used
N = 1000;%number of timesteps
D = 10.^[-4:.05:1.4];%decoherence D = \gamma \tau, over entire pulse
alpha = f.*pi./2.*sqrt(A./D);
out = zeros(length(D),length(ic));
symout = out;
decout = out;
for ii = 1:length(D)
    [stangle] = simple_tangle(ic,A,f,N,D(ii),2);
    [symtangle] = sym_tangle2(ic,A,f,N,D(ii));
    [dectangle] = dec_tangle(ic,A,f,N,D(ii));
    [trajtangle]= traj_tangle(ic,A,f,N,D(ii),20);
    out(ii,:) = stangle(end,:);
    symout(ii,:) = symtangle(end,:);
    decout(ii,:) = dectangle(end,:);
    trajout(ii,:) = trajtangle(end,:);
end
```

---

simple_tangle.m

Calculates closed system entanglement.

```
function [tangle,entropy] = simple_tangle(initial_cond,A,f,N,D,hdim)
%SIMPLE_TANGLE computes the tangle using without decoherence
%[tangle] = SIMPLE_TANGLE(ic,A,f,N,D,jumps) will compute
% the tangle as a function of time for a single atom in free space
% interacting with a laser of cross sectional area A
% (in units of the on resonance cross section), and using a
% pulse that is a fraction f of a NOT gate.  N is the number
%of atomic widths in the pulse, and D is th decoherence
%over the entire pules D = Gamma * tau.  No actual decoherence
% is used, and it is assumed that the atom only interacts with
% a single field mode. (ala vanEnk and Kimble) ic is the initial
%condition, and is a vector of size 2xN, where N is the number of
%initial conditions, and ic(1,:) is the amplitude for the excited
%state.

if(nargin<6)
    hdim = 2;
end
if(nargin<2)%these are the default values for parameters
    A = 1000;
    f = 1;
```

```
    N = 10.^4;
    D = .1;
end

if(size(initial_cond,1)==1)
    initial_cond = initial_cond.';
end

if any(abs(sum(abs(initial_cond).^2,1)-1)>10.^-8)
    error('Initial conditions must be normalized states.');
end

%calculate constants
a = sqrt(D./A)./N; %g tau/N
alpha = f.*pi./2.*sqrt(A./D);%amplitude
n_ics = size(initial_cond,2);



%create the propagator
H = kron(eye(hdim),[0 alpha;alpha 0]);
for jj = 1:hdim-1
    H(1+2*(jj-1),2*(jj+1)) = sqrt(jj);
    H(2*(jj+1),1+2*(jj-1)) = sqrt(jj);
end
propagator = expm(-i.*a.*H);

%initialize the output
tangle = zeros(N,n_ics);
```

```
if nargout>1
    entropy = zeros(N,n_ics);
end

for jj = 1:n_ics
    %calculat the trajectory
    traj = calc_traj2([initial_cond(:,jj);zeros(2*(hdim-1),1)],...
     propagator,N);

    tangle(:,jj) = squeeze(calc_tangle(traj));
    if(nargout>1)
        entropy(:,jj) = calc_von(traj);
    end
end
return
```

---

sym_tangle2.m

Calculates entanglement with the symmetric laser mode.

```
function [tangle,ent,rhos_out] = sym_tangle2(initial_cond,A,f,N,D)
%SYM_TANGLE2 computes the tangle using mixed trajectory method
%[tangle] = sym_tangle2(ic,A,f,N,D)  will compute
% the tangle as a function of time for a single atom in free space
% interacting with a laser of cross sectional area A
```

```
% (in units of the on resonance cross section), and using a
% pulse that is a fraction f of a NOT gate.  N is the number
%of atomic widths in the pulse, and D is th decoherence
%over the entire pules D = Gamma * tau.  No actual decoherence
% is used, and it is assumed that the atom only interacts with
% a single field mode. (ala vanEnk and Kimble) ic is the initial
%condition, and is a vector of size 2xN, where N is the number of
%initial conditions, and ic(1,:) is the amplitude for the excited
%state.

if(nargin<2)%these are the default values for parameters
    A = 1000;
    f = 1;
    N = 10.^4;
    D = .1;
end

%check for single row vector ic.
if(size(initial_cond,1)==1)
    initial_cond = initial_cond.';
end

%parse initial conditions
if(ndims(initial_cond)==2)
    %initial conditions are state vectors
    n_ics = size(initial_cond,2);
    %convert to density matrices
    initial_cond = permute(initial_cond,[1 3 2]);
```

```
    initial_cond = create_density(initial_cond);
end

n_ics = size(initial_cond,3);



if any(ntrace(initial_cond)-1>10.^-8)
    error('Initial conditions must be normalized states.');
end

%Now create the propagators
propagators = create_props(A,f,N,D);
%create the swap propagator
swap = [eye(2),zeros([2 4]);zeros([2 4]),...
eye(2);zeros(2),eye(2),zeros(2)];
%create the dynamics propagator
prop = zeros(6);
prop(1:4,1:4) = propagators.full;
prop(5:6,5:6) = propagators.field;
prop = prop*swap;
%create the unitary matrix to find the symmetric field mode
symetrizer = create_symetrizer(N);
prop = ntimes(symetrizer,prop);

%First allocate space for the answers



%create the operator that changes from small symetric
```

```
% states to the whole symmetric state
fixer = reshape([1:N],[1 1 N]);
fixer = repmat(sqrt(fixer./N),[2 1 1]);
fixer = cat(1,ones(size(fixer)),fixer);
fixer = create_density(fixer);

%initalize vars/allocate space
rhos= zeros([4 4 N]);
rhos_out = zeros([4 4 n_ics]);
tangle = zeros([N n_ics]);
if nargin>1
    ent = zeros([N n_ics]);
end

%loop over initial conditions
for jj = 1:n_ics
    rho = zeros(6);
    rho(1:2,1:2) = initial_cond(:,:,jj);
    for ii = 1:N
        %apply the propagator
        rho = prop(:,:,ii)*rho*prop(:,:,ii)';
        %find the jump probability
        p_jump = 1-trace(rho);
        %trace out the antysymmetric part
        rho(1:2,1:2) = rho(1:2,1:2)+rho(5:6,5:6);
        rho(5:6,:) = 0;rho(:,5:6) = 0;
        %ensure Hermiticity
        rho = (rho + rho')./2;
```

```
        %put in the jumps
        jump_rho = rho([1 3],[1 3]);
        if trace(jump_rho)>0
            p_jump = p_jump./trace(jump_rho);
        end
        rho([2 4],[2 4]) = rho([2 4],[2 4])+p_jump.*jump_rho;
        %save this iteration (note, initial state is not saved)
        rhos(:,:,ii) = rho(1:4,1:4);
    end
    %fix to cover entire symmetric space.
    rhos = fix_rho(fixer.*rhos,partial_trace(rhos,2));
    %calculate the tangle
    tangle(:,jj) = wtangle(rhos);
    if nargin>1
        ent = calc_von(rhos);
    end
    rhos_out(:,:,jj) = rhos(:,:,end);
end

return
```

---

dec_tangle.m Computes the same quantity as simple_tangle.m except includes decoherence at rate Γ given by the standard Linblad form.

```
function [tangle] = dec_tangle(initial_cond,A,f,N,D)
%DEC_TANGLE bounds full paraxial system entanglement
%[tangle] = SIMPLE_TANGLE(ic,A,f,N,D,jumps)  will compute
% the tangle as a function of time for a single atom in free space
% interacting with a laser of cross sectional area A
% (in units of the on resonance cross section), and using a
% pulse that is a fraction f of a NOT gate.  N is the number
%of atomic widths in the pulse, and D is th decoherence
%over the entire pules D = Gamma * tau.  No actual decoherence
% is used, and it is assumed that the atom only interacts with
% a single field mode. (ala vanEnk and Kimble) ic is the initial
%condition, and is a vector of size 2xN, where N is the number of
%initial conditions, and ic(1,:) is the amplitude for the excited
%state.

if(nargin<2)%these are the default values for parameters
    A = 1000;
    f = 1;
    N = 10.^4;
    D = .1;
end

if(size(initial_cond,1)==1)
    initial_cond = initial_cond.';
end

%parse initial conditions
if(ndims(initial_cond)==2)
```

```
    %initial conditions are state vectors
    n_ics = size(initial_cond,2);
    %convert to density matrices
    initial_cond = permute(initial_cond,[1 3 2]);
    initial_cond = create_density(initial_cond);
end
n_ics = size(initial_cond,3);

if any(ntrace(initial_cond)-1>10.^-8)
    error('Initial conditions must be normalized states.');
end

%calculate constants
a = sqrt(D./A)./N; %g tau/N
alpha = f.*pi./2.*sqrt(A./D);%amplitude

hdim = 2;
%create the propagator
H = kron(eye(hdim),[0 alpha;alpha 0]);
for jj = 1:hdim-1
    H(1+2*(jj-1),2*(jj+1)) = sqrt(jj);
    H(2*(jj+1),1+2*(jj-1)) = sqrt(jj);
end
H(1,1) = -i.*D./(N.*2.*a);H(3,3)=H(1,1);
propagator = expm(-i.*a.*H);

%initialize the output
tangle = zeros(N,n_ics);
```

```
rhos = zeros([4 4 N]);

for jj = 1:n_ics
    %calculat the trajectory
    rho = zeros(4);
    rho(1:2,1:2) = initial_cond(:,:,jj);
    for ii = 1:N
        rho = propagator*rho*propagator';
        p_jump = (1-trace(rho));
        rho_jump = rho([1 3],[1 3]);
        if trace(rho_jump)>0
            p_jump = p_jump./trace(rho_jump);
        end
        rho([2 4],[2 4]) = rho([2 4],[2 4]) + p_jump.*rho_jump;
        rhos(:,:,ii) = rho;
    end
    tangle(:,jj) = wtangle(rhos);
end
return
```

---

traj_tangle.m

Computes an upper bound on the entanglement between the full paraxial subsystem and the atom.

```
function [tangle] = traj_tangle(initial_cond,A,f,N,D,n_jumps)
%TRAJ_TANGLE computes the tangle using quantum trajectories
%[tangle] = traj_tangle(ic,A,f,N,D,jumps)  will compute
% the tangle as a function of time for a single atom in free space
% interacting with a laser of cross sectional area A
% (in units of the on resonance cross section), and using a
% pulse that is a fraction f of a NOT gate.  N is the number
%of atomic widths in the pulse, and D is th decoherence
%over the entire pules D = Gamma * tau.  No actual decoherence
% is used, and it is assumed that the atom only interacts with
% a single field mode. (ala vanEnk and Kimble) ic is the initial
%condition, and is a vector of size 2xN, where N is the number of
%initial conditions, and ic(1,:) is the amplitude for the excited
% state.

%start by cheecking that the inputs are present
if(nargin<6)
    n_jumps = 0;
end
if(nargin<2)%these are the default values for parameters
    A = 1000;
    f = 1;
    N = 10.^4;
    D = .1;
end

if(size(initial_cond,1)==1)
    initial_cond = initial_cond.';
```

```
end

if any(abs(sum(abs(initial_cond).^2,1)-1)>10.^-8)
    error('Initial conditions must be normalized states.');
end

%some useful quantities
n_ics = size(initial_cond,2);

%Now create the propagators
propagators = create_props(A,f,N,D);

%First allocate space for the answers
tangle = zeros([N n_ics]);

for jj = 1:n_ics

    [rhos] = calc_rhos(initial_cond(:,jj),propagators,N);

    %create the post jump trajectory density matrices
    [jump_rhos,jump_rhosc] = calc_rhos([0;1],propagators,N);

    %calculate the probability for jumping
    prob = jump_probs(ntrace(rhos),ntrace(jump_rhos),n_jumps);
    tangle(:,jj) = squeeze(calc_tangle(rhos)+multiconv(prob,...
        calc_tangle(jump_rhos)));
end
```

```
return
```

---

create_props.m

Creates the propagators for the various subsystems based upon the evolution parameters.

```
function [propagators] = create_props(A,f,N,D)
%CREATE_PROPS creates the nonunitary propagators
%A - area of beam in units of on resononce cross section
%f - fraction of a NOT gate implemented
%N - number of atomic widths in pulse
%D - decoherence over the pulse
%propagators - structure contaning the atomic, field
%and atom to field propagators
%propagators.atomic
%propagators.field
%propagators.atof

%a = g tau
a = sqrt(D./A./N);

%b = Gamma - kappa / 2 g
b = a./2 .*(A - 1);
```

```
%alpha is the laser amplitude
alpha = pi .* f ./ 2 ./a ./N;

%The generator for the atom and currently coupled field is
Ga = -a .*[b        i.*alpha    0      i
           i.*alpha    0        0      0
           0           0        b   i.*alpha
           i           0    i.*alpha   0];

%the generator for the uncoupled fields is then
Gf = Ga(1:2,1:2);

%then the propagator for the atom-field is
prop = expm(Ga);

%then we can pick off the parts as
propagators.atomic = prop(1:2,1:2);
propagators.atof = prop(3:4,1:2);
propagators.field = expm(Gf);
propagators.full = prop;

return;
```

---

calc_rhos.m

Propagates the Schrödinger equation.

```
function [rhos,rhosc,field,nonbasis]...
= calc_rhos(ic,props,N,basis,left_fill,scale)
%CALC_RHOS calculates a trajectory
%[tra] = calc_rhos(ic,props,N) calculates a trajectory
%starting with the initial condition ic, using the step
% propagators in props, for N steps.
%traj is a set of reduced density matrices of length N
%This function is works for the flying qubit picture
%basis if provided is a 2x1xN list of two basis vectors
%in the field subspace
%
%see also: calc_traj2
if(nargin<6)
    scale = ones([1 1 N]);
end
if(nargin<5)
    left_fill = zeros([4 1 N]);
end
if(nargin<4)
    basis = symmetric(N);
end

[atom,field] = calc_psi(ic,props,N);

%now create the inverse propagator
prop = powers(inv(props.field),0,1,N-1);
```

```
prop = prop(:,:,end:-1:1);

%create the reduced density matrix on the atomic subsystem
rhos = cumsum(create_density(field),3);
rhos = ntimes(ntimes(prop,rhos),permute(conj(prop),[2 1 3]));
rhos = (rhos + permute(conj(rhos),[2 1 3]))/2;
rhos = rhos + create_density(atom);
if nargout==1 %abort here if we don't want symmetric traj.
    return;
end

%change basis of field states
field = multiconv(permute(conj(basis(:,:,end:-1:2)),[2 1 3]),field);
atom = repmat(atom,[1 2 1]).*repmat(basis(:,:,1)',[2 1 N]);
%now undo any nonunitary evolution
field = ntimes(prop,field);
%sum things up to get the full state vector in the
%reduced subspace at all times N
field = reshape(atom + field,[4 1 N]);
field = field.*repmat(scale,[4 1 1])+left_fill;

%calculate the part of the space left out
%(Probability of projecting outside the subspace)
rhos = rhos - create_density(field(1:2,:,:))...
   - create_density(field(3:4,:,:));
nonbasis = zeros([4 4 N]);
nonbasis(1:2,1:2,:) = rhos;
%create the density matrix on this reduced subspace,
```

```
%remembering to add any probability projected
%outside the space incoherently
rhosc = create_density(field)+nonbasis;
%now again calculate the density reduced onto
%the atomic subspace (should be exactly the same as before)
rhos = rhosc(1:2,1:2,:)+rhosc(3:4,3:4,:);

return
```

---

jump_probs.m

Calculates the jump probabilities in the quantum trajectory method during specific time steps.

```
function [prob] = jump_probs(bprob,iprob,reps)
%JUMP_PROBS calculate probability for jumps
if nargin<3
    reps = 1;
end
if reps<=0
    prob = zeros(size(bprob));
    return
end

if size(bprob,1)==1
```

```
    bprob = bprob(:);
end
N = size(bprob,1);
d = size(bprob,2);

%calculate the probabilities for the insert and base cases
iprob = iprob(:);
bprob = cat(1,zeros([1 d]),1-bprob);
bprob = diff(bprob);
iprob = [0;1-iprob];
iprob = diff(iprob);

%calculate the convolved insert probability
temp = 1;
for ii = 2:reps
    temp = conv(iprob,temp);
    temp = temp(1:N);
    temp(1) = temp(1)+1;
end
iprob = temp;
prob = zeros([N,d]);
for ii = 1:d
    temp = conv(iprob,bprob(:,ii));
    prob(:,ii) = temp(1:N,1);
end
return
```

ntrace.m

Takes the trace of a vector of density matrices.

```
function [tra] = ntrace(in)
%NTRACE take the trace of n matrices
%trace = ntrace(in) with in a dxdxN matrix and
% trace is a 1x1xN matrix of the traces.

S = size(in);
if(ndims(in)<3)
    S(3) = 1;
end
if S(1) ~= S(2)
    error('matrices not square');
end
S2 = [S(1)*S(2) prod(S(3:end))];
in = reshape(in,S2);
tra = sum(in(1:S(1)+1:end,:));
tra = reshape(tra,[S(3:end) 1]);
return
```

---

calc_tangle.m

Calculates the tangle for a bipartite pure state.

```
function [tangle] = calc_tangle(rhos)
%CALC_TANGLE calculates the bipartite tangle
%tangle = calc_tangle(rhos) calculates the
%bipartite tangle, assuming that
%rhos is a set of reduced density matrices obtained
%from a pure state (presumably at different times).
%output is a single column vector

S = size(rhos);
%first make sure that all of the matrices are normalized.
norm = rhos(1,1,:) + rhos(2,2,:);
rhos = rhos./repmat(norm,[2 2 1]);

%square the matrices and take the trace
tangle = rhos(1,1,:).^2 + rhos(2,2,:).^2 ...
+ 2.* rhos(1,2,:).*rhos(2,1,:);

%then complet the formula for the bipartite tangle
tangle = 2.*(1-tangle(:));

tangle = reshape(tangle,[1 1 S(3:end)]).*norm;
return;
```

multiconv.m

Performs a multidimensional convolution.

```
function [b] = multiconv(a,b)
%MULTICONV Does multiple convolutions
%base = multiconv(bprob, base, iprob, insert, reps)
% inserts insert into base reps times, where bprob
% is the probability that no insertion occurs for the
% base, and  iprob is the same for the insertion.

%calculate sizes and reshape, base and insert
%should have the same size
sa = size(a);
sb = size(b);
if(ndims(a)<3)
    a = reshape(a,[1 1 sb(3)]);
    sa = size(a);
elseif ndims(b)<3
    b = reshape(b,[1 1 sb(3)]);
    sb = size(b);
end
s = zeros(1,3);
s = max(sa,sb);
a = repmat(a,s./sa);
b = repmat(b,s./sb);
a = reshape(a,[s(1)*s(2) s(3)]);
b = reshape(b,[s(1)*s(2) s(3)]);
```

```
%add in the insert
for ii = 1:s(1)*s(2)
    temp = conv(b(ii,:),a(ii,:));
    b(ii,:) = temp(:,1:s(3));
end
%reshape back to output size
b = reshape(b,s);
return
```

---

create_density.m

Creates density matrices for a vector of initial pure states.

```
function [rho] = create_density(psi)
%CREATE_DENSITY create a density matrix for a pure state
%rho = create_density(psi) takes in a state vector
% psi and puts out rho=psi'*psi.  It also works if
%for a vector of psi's.  However singleton dimensions
% in the first or second position will be removed.

%remove unwanted singleton dimensions
sp = size(psi);
if sp(1)==1
    sp(1)=[];
```

```
elseif sp(2)==1
    sp(2)=[];
end
%add in a working dimension
sp = [sp(1) 1 sp(2:end)];
psi = reshape(psi,sp);

%now actually create the density matrix
rho = repmat(psi,[1 sp(1) ones(1,length(sp)-2)]);
rho = conj(permute(rho,[2 1 3:length(sp)])).*rho;
return
```

---

wtangle.m

Calculate the tangle using Wooters' formula [94]

```
function [tangle] = wtangle(rhos)
%WTANGLE Compute the wooters tangle
%tangle = wtangle(rhos) with rhos a 4x4xN list of density matrices
%comutes the wooters tangle Nx1

N = size(rhos,3);
tangle = zeros(N,1);

%create sigmay tensor sigmay
```

```
sy = zeros(4);
sy(1,4)=-1;sy(2,3)=1;sy(3,2)=1;sy(4,1)=-1;

rhos = ntimes(rhos,ntimes(ntimes(sy,conj(rhos)),sy));

for ii = 1:N
    E = sort(eig(rhos(:,:,ii)));
    E = sqrt(abs(E));
    tangle(ii) = (max(0,E(4)-E(1)-E(2)-E(3))).^2;
end
return
```

---

calc_traj2.m

Calculates a closed system trajectory.

```
function [traj] = calc_traj2(ic,prop,N)
%CALC_TRAJ2 calculates a trajectory
%[traj] = calc_traj2(ic,prop,N) calculates a trajectory
% starting with the initial condition ic, using the
% step propagator in prop, for N steps.
%traj is a set of reduced density matrices of length N
%This function is works for the single field mode picture.
%
%see also: calc_traj2
```

```
%get info about the initial conditon
ic = ic(:);
d = length(ic);

%allocate space for the answer
traj = zeros([2 2 N]);

psi = ntimes(powers(prop,1,1,N),ic);
traj = partial_trace(create_density(psi),2);
return
%older code for the partial trace.
for jj = 1:d./2
    traj = traj + create_density(psi([2*jj-1 2*jj],:,:));
end
return
```

---

partial_trace.m

Calculates the partial trace for a vector of density matrices.

```
function [reduced] = partial_trace(rho,n)
%PARTIAL_TRACE calculate the partial trace
%rho the input matrix
%n the dimenision of the subsystem not to be traced over
```

```
%assumed to be the least significant one

d=size(rho,1);
if(d~=size(rho,2))
    error('must use square matrices');
end
N = size(rho,3);

reduced = zeros([n n N]);
for ii = 1:n:d
    reduced = reduced + rho(ii:ii+n-1,ii:ii+n-1,:);
end
return
```

---

fix_rho.m

Keeps the dynamical symmetric mode, tracing out nonsymmetric paraxial submodes.

```
function [rho] = fix_rho(rho,reduced)
%FIX_RHO fix the partial trace to be a certain matrix
%reduced final partial trace
%rho initial density operator
%reduced, target reduced matrix
n = size(reduced,1);
temp = zeros(size(rho));
```

```
temp(1:n,1:n,:) = reduced - partial_trace(rho,n);
rho = rho+temp;
return
```

---

create_symetrizer.m

Generates the transformation needed to extract the dynamical symmetric mode.

```
function [sym] = create_symetrizer(N)
%CREATE_SYMETRIZER creates a unitary matrix to symmetrize
%N the total number of matrices to create
%sym is the unitary symetrizing matrix

%create a list of numbers from 1 to N
temp = reshape(1:N,[1 1 N]);
%zero the matrix
sym = zeros([6 6 N]);
%create the identity on the no photon space
sym(1,1,:) = 1;sym(2,2,:) = 1;
%This acts on the newly added mode
a = 1./sqrt(temp);
sym(3,3,:) = a;sym(4,4,:) = a;
sym(5,5,:) = a;sym(6,6,:) = a;
%this acts on the previously symmetric mode.
```

```
b = sqrt((temp-1)./temp);
sym(3,5,:) = b;sym(4,6,:) = b;
sym(5,3,:) = -b;sym(6,4,:) = -b;

return
```

---

powers.m

For calculating all powers of a matrix.

```
function [out] = powers(in,start,skip,stop)
%POWERS raises a matrix to consecutive powers
%out = powers(in,start,skip,end) outputs a list of
% matrices, such that
%out(:,:,i) = in^pow(start + skip*i).
% in must be a square matrix.
%Computed using an eigendecomposition.

%compute dimensions
d = size(in,1);
N = floor(1+ (stop-start)./skip);
so = [d d N];
out = zeros(so);

%exponentiate the eigenvalues
```

```
[V,D] = eig(in);
D = diag(D);
out = repmat(D(:).^skip,[1 1 N]);
out(:,1,1) = D(:).^start;
out = cumprod(out,3);
out = repmat(out,[1 d 1]);

%multiply by the eigenvectors
out = out.*repmat(inv(V),[1 1 N]);
out = ntimes(V,out);
return
```

---

calc_psi.m

Calculates pure state evolutions.

```
function [atom,field] = calc_psi(ic,props,N)
%CALC_PSI calculates a wavefunction
%[atom,field] = calc_psi(ic,props,N) calculates
% a trajectory wave function with the
%initial condition ic, using the step propagators in
%props, for N steps.
%This function is works for the flying qubit picture
%
%see also: calc_traj2
```

```
%get info about the initial conditon
ic = ic(:);
d = size(ic,1);

%propagate the inital conditions through N steps
atom = ntimes(powers(props.atomic,1,1,N),ic);
field = ntimes(props.atof,cat(3,ic,atom(:,:,1:end-1)));
prop = powers(props.field,0,1,N-1);
prop = prop(:,:,end:-1:1);

%Move to a heisenberg like picture to
%simplify things (note prop is not unitary)
field = ntimes(prop,field);

return
```

---

ntimes.m

Multiplies vectors of matrices.

```
function [out] = ntimes(in1,in2)
%NTIMES multiplies many matrices at once
%[out] = ntimes(in1,in2) computes
%out(:,:,i) = in1(:,:,i)*in2(:,:,i) for all i
```

```
%also works for matrices of higher dimension
% than four, or mismatched dimensions.
%The only condition is that size(in1,2) = size(in2,1).

%get the sizes of the input matrices, and pad
s1 = size(in1);
s2 = size(in2);
if length(s1)<length(s2)
    s1 = [s1 ones(1,length(s2)-length(s1))];
else
    s2 = [s2,ones(1,length(s1)-length(s2))];
end
so = max(s1,s2);
so(1:2) = [s1(1) s2(2)];
%allocate space for output matrix
out = zeros(so);

if(s1(2)~=s2(1))
    error('Mismatch in multiplying dimension, cannot multiply');
end

%Now to calculate the replication factors
r1 = so./s1;r2 = so./s2;
r1(1:2) = 1; r2(1:2) = 1;
if(round(r1)~=r1 | round(r2)~=r2)
    error('Arrays must be expanded by nonintegral factor');
end
```

```
%First reshufle the first two dimensions, and fill in all dims
in2 = repmat(in2,[s1(1) ones(1,length(s2)-1)]);
in2 = reshape(in2,[s2(1) s1(1).*s2(2) s2(3:end)]);
in2 = permute(in2,[2 1 3:length(s2)]);
in1 = repmat(in1,[s2(2) r1(1,2:end)]);
in2 = repmat(in2,r2);

%multiply the matrices
out = sum(in1.*in2,2);
out = reshape(out,so);

return
```

Appendix B

Alkali simulation code

This appendix contains the code necessary for calculating the evolution of an alkali atom probed by a polarized laser and manipulated by time dependent magnetic fields as described in Chap. 4 and Chap. 5. The main functions used for the evolution are reproduced here, though some of the minor subroutines are not included. `RunD1new3.m` is the main routine used to specify parameters for the evolution, and call the appropriate routines. `callibration.m` performs the fits necessary to calibrated based on fiducial runs as described in Sec. 5.2.2. `bounded_est.m` uses the time dependent measurement basis, along with experimental data, to find the best fit estimate of the initial state for a given set of magnetic fields, as described in Chap. 5. `fitall.m` finds the best estimate for the state and the field scaling simultaneously as described in Sec. 5.2.2. All files are set up for reconstruction of the $F = 3$ ground state using the birefringent measurement with a laser tuned to the D1 $S_{1/2} \rightarrow P_{1/2}$ transition.

RunD1new3.m

This is the main calling function for the evolution. All of the user selectable pa-

rameters that can change from run to run are specified here. This file is set up to evolve the measurements. The main output is *as* which contains the measurement direction as a function of time. To run the code a `params_fit.mat` file is necessary which is obtained by calling `callibration.m`. Additionally a `params` structure is needed with the following fields

params.run_type = 2 for reconstruction

params.rho: initial system state obtained by calling `calc_initial.m`

params.base_state : index into pop_est from fits

params.mag_x_file : file containing experimental magnetic fields

params.mag_y_file : file containing experimental magnetic fields

params.data_filename : file containing experimental data

params.B : magnetic fields (xscale,yscale,x0,y0,z0)

params.sig_start : reconstruction start time

params.params_filename : fit file obtained from calibration

params.npoints : number of data points to use

```
clear Laser MagneticField InitialState Parameters Repumper;
if exist('params')
    params = load_state_params(params);
else
    params = load_state_params('params.mat');
end
load(params.params_filename);
run_type = params.run_type;
```

```
mag_x_file = params.mag_x_file;
mag_y_file = params.mag_y_file;
data_filename = params.data_filename;
sig_start = params.sig_start;
if isfield(params,'npoints')
    npoints = params.npoints;
end
if ~isfield(params,'rho') || isempty(params.rho)
    InitialState.rho = diag(pop_est(params.base_state,:));
    InitialState.direction = [0 1 0];
else
    InitialState.rho = params.rho;
    InitialState.direction=[0 0 1];
end
if isfield(params,'B')
    mag_fact = params.B(1:2);
    background_offset = params.B(3:5);
end
if ~exist('mag_fact')
    mag_fact = [1 1];
end
if ~exist('background_offset')
    background_offset = [0 0 0 ];
end
background_filename = [folder_name 'background fields.txt'];


%run_type possibilities
```

```
%1 - callibraiton
%2 - reconstruction
%3 - run without data
%5 - initial_state evolution
%6 - full state evolution

%This is the filename for the experimentald data,
% again set to "[]" if no data to input

    if any(run_type == [5 6])
        Parameters.evolve_state = -1;
    else
        Parameters.evolve_state = 0;
    end
    if run_type==5
        run_time = (sig_start-base_time).*1e3;
    end
%This is how much finer the simulation will be than
%the experiment if set to 1 then sim will run at the
% same rate, 2 twice as fast, etc.
    upsample_factor = 1;%amount to upsample by
%this is the initial state


    %undoing everything for a run without data
    %(ie not simulating a specific experiment)
    if run_type ==3
        data_filename = [];
```

```
        background_filename = [];
        mag_x_file = [];
        mag_y_file = [];
    end


%load in the initial field parameters
%Control fields used are loaded here
if exist('best_mar.mat')
    load best_mar;%mat file with the fields
end
    field_span = recon_length;%ms, time over which
          %the fields are active (starting from 0)
%If the trace (max possible signal) for the
% experimental data is known place it here
    fix_trace=1;%1./.3709;%in Volts, set to 0 if unkown

%This parameter indicates the orientation of the probe
% with respect to arbitrary space fixed axes.
    tilt = 0;%6.2667/180.*pi;%tilt up from z axis
    Laser.orientation = [sin(tilt) 0 cos(tilt)];
    Laser.detuning = det;%GHz

%Laser.scattering_time is the scattering time in milliseconds.
%Debye-Waller factors are not included in the
%code, so they should be used to modify the scattering time
    %scale_factor =1.05;
    if run_type==2 | run_type==3 | ~exist('falloff_factor','var')
```

```
        falloff_factor = 1.0;
    end
    if ~exist('mag_fact','var');
        mag_fact = [1 1];
    else
        if length(mag_fact)==1
            mag_fact = mag_fact*[1 1];
        end
    end
    Laser.scattering_time = base_scatter*scale_factor ...
     .*falloff_factor;%ms

%Laser.polarization is the polarization of the lattice
%beams at the position of the atom.  This should be
%the total polarization due to all lattice beams.
%The coordinates are cartesian [x y z], $z$ is along
%the beam axis NOT along space fixed axis
    theta = .011875988984545;
    Laser.stokes = [1 0 0];
    Laser.meas_stokes = [sin(theta) cos(theta) 0];
    Laser.stokes = Laser.stokes./norm(Laser.stokes);
    if isfield(params,'stokes') & ~isempty(params.stokes)
        Laser.meas_stokes(2,:) = params.stokes;
    else
        Laser.meas_stokes(2,:) = ...
            -[-0.10465*sin(theta), -0.10465*cos(theta), 0.994509];
    end
    Laser.meas_stokes(3,:) = [0 0 1];
```

```
    Laser.meas_stokes(4,:) = [0 1 0];

%load inhomogeneity
    decay = 0;decay2 = 0;
        if (any(run_type == [3])|~exist(dist_name,'file')|...
          isempty(dist_name) )
            Laser.probabilities = 1;
            Laser.flucts = 1;
        else
            load(dist_name);
            Laser.probabilities = probs;
            Laser.fluctuations = flucts;
        end
        if run_type ~=1
            decay = 0;decay2 = 0;
        end

%This block includes some calculations
%input the data
if run_type~=1 & exist('recon_offset');
    offset = recon_offset;
end

if ~isempty(data_filename)
    [data,sim_times] = input_data(data_filename,...
     upsample_factor,sig_start.*1e3,-offset);
else
    num_samples = 1000;run_time = field_span;%ms
```

```
    sim_times = [1:num_samples].*run_time./num_samples;
    data = zeros(size(sim_times));
end



if any(run_type==[5 6])
    dt = mean(diff(sim_times));
    sim_times = mod(run_time,dt):dt:run_time;
    sig_start = sig_start-run_time.*1e-3;
    data = zeros(size(sim_times));
elseif ~isempty(npoints)
    data = data(1:npoints);
    sim_times = sim_times(1:npoints);
end

if ~isempty(background_filename)
    background_fields = input_mag_fields(background_filename...
     ,sim_times+1e3.*sig_start);
else
    background_fields = zeros(length(sim_times),3);
end

%parameter setting block do not change *****************
    Parameters.time = max(sim_times); %1.3;%ms
    Parameters.N = length(sim_times);
    Parameters.pad_time = min(sim_times);
    if run_type~=5
        Parameters.bad_data = 4;
```

```
    else
        Parameters.bad_data = 0;
    end
    Parameters.optim_step = 1;
    Parameters.predict = 0;
%end block ******************************************

%this sets up the time dependent magnetic fields by interpolation
if ~isempty(mag_x_file) & ~isempty(mag_y_file)
    MagneticField.static = input_mag_direction(mag_x_file...
     ,mag_y_file,sim_times,sig_start.*1e3);
else
    field_times = sim_times(sim_times<=field_span);
    MagneticField.static = [angle_interp(field_params,...
     field_times,field_span) zeros(length(field_times),1)];
end
if size(MagneticField.static,1) < Parameters.N
    MagneticField.static = cat(1,MagneticField.static,...
     zeros(Parameters.N-length(field_times),3));
else
    MagneticField.static = MagneticField.static(1:Parameters.N,:);
end


%calculating magnetic fields if none given
ang = 0;%radians

if run_type ==4 | (run_type ==1 & isempty(mag_x_file))
```

```
if dir == 1
MagneticField.static = repmat([cos(ang) 0 sin(ang)],...
[size(MagneticField.static,1),1]);
elseif dir == 0
MagneticField.static = repmat([-sin(ang) 0 cos(ang)],...
[size(MagneticField.static,1),1]);
else
MagneticField.static = repmat([0 1 0],...
[size(MagneticField.static,1),1]);
end
mag = base_mag;
else
    mag = 1;
end
if run_type ==1 && ~isfield(params,'B')
mag = mag.*mag_shift;
end
if isfield(params,'zrun') & params.zrun==1
    MagneticField.static(:,3) = -mag_fact(1).*...
     MagneticField.static(:,1).*.575;
    MagneticField.static(:,1) =0;
else
    MagneticField.static(:,1) = -mag_fact(1).*...
     MagneticField.static(:,1);
end
MagneticField.static(:,2) = -mag_fact(2).*...
MagneticField.static(:,2);
MagneticField.static = mag.*MagneticField.static ...
```

```
+ background_fields;
MagneticField.static = MagneticField.static ...
+ repmat(background_offset(:).',...
   [size(background_fields,1) 1]);

if(exist('snr'))
    Parameters.SNR = snr;
else
    Parameters.SNR = 1;
end




    Parameters.nonlinear = 1;%Include the nonlinear light shift
    Parameters.scatter = 1;
    %the hyperfine state we are reconstructing
    Parameters.F = 3;
    %this is the type of filter 'none' for no filter
    % 'bessel' for a bessel filter
    Parameters.filter_name = 'bessel';%'bessel';
    %band of the filter in kHZ
    Parameters.filter_band = filter_band;%kHz band pass filter;
    Parameters.refilter_band = [10 80];%kHz band pass filter;
    %and the order of the filter
    Parameters.filter_order = 4;%fourth order filter;
    if fix_trace==0
```

```
        Parameters.include_trace = 0;
    else
        Parameters.include_trace = 1;
    end
    Parameters.include_trace = 0;

    Parameters.OD = 1;%on resonance optical depth

%deprecated code do not change
Repumper.polarization = 0;%pi polarized
Repumper.rotation = [0 0 1];%point along the quantization axis
Repumper.rabi = 25;%MHz
Repumper.on = 0;

[as,MagneticField,Z,rho0,Zsmall,gammas,as_full] = ...
lattice_cov_D1(Laser...
,MagneticField...
,Repumper...
,Parameters...
,InitialState);

%postfiltering
if length(as_full)~=1
if ~isempty(findstr(data_filename,'- lin'));
    as = as_full(:,:,1);
else
    as = as_full(:,:,2);
end
```

```
end
Zsmall = real(as.'*rho0(:));
data = data((Parameters.bad_data+1):end);
data0 = data;Z0 = Z;gammas0 = gammas;as0 = as;Zsmall0=Zsmall;
Hd = create_filter(Parameters.filter_name...
,Parameters.filter_order...
,Parameters.refilter_band...
,Parameters.N...
,Parameters.time);
data = filter(Hd,data);
Z = filter(Hd,Z);
Zsmall = filter(Hd,Zsmall);
gammas = filter(Hd,gammas);
as = filter(Hd,as.').';
for pol_num = 1:size(as_full,3);
    as_full(:,:,pol_num) = filter(Hd,as_full(:,:,pol_num).').';
end
if Parameters.bad_data>0
nums = [1:length(Zsmall)]./length(Zsmall)...
.*(sim_times(end)-sim_times(Parameters.bad_data));
else
nums = [1:length(Zsmall)]./length(Zsmall).*sim_times(end);
end

Zsmall = Zsmall.*exp(-nums.*decay-nums.^2.*decay2).';
%add in extra paramaters offset and extra decay
val = rms_res(Zsmall,data);
return
```

---

angle_interp.m

Upsampling routine used to interpolate the 50 angles used to optimize the covariance matrix and turn them into a full set of magnetic fields for each simulation step as described in Sec. 5.1.3.

```
function [out] = angle_interp(in,N,sN)
%in the vector to be interpolated
%N the number of points in the output
%sN the start size, up interpolation is by floor(N./sN)
mags = sqrt(sum(abs(in).^2,2));
angs = unwrap(atan2(in(:,2),in(:,1)));
if length(N)==1
if nargin<3
    sN = size(in,1);
end
factor = N./sN;
if factor ==1
    out = in;
    return;
end
    angs = interp(angs,factor);
else
    sN = [0:size(in,1)-1]./size(in,1).*sN;
    angs = spline(sN.',angs,N.');
```

```
end
%mags = interp(mags,factor);
out(:,1) = mags(1).*cos(angs);
out(:,2) = mags(1).*sin(angs);
return
```

---

bounded_est.m

Estimates the best fit state $\bar{\rho}$ given data and measurement operators, as, as a function of time.

```
function [rho,res,R,rho0] =...
bounded_est(data,as,SNR,trace_uncertainty)
data = data(:);
if nargin<3
    trace_uncertainty = .01;
end
sigma = 1./(SNR./sqrt(max(sum(abs(as).^2,1))));
[R,rho0] = unbound_est(data,conj(as),sigma,trace_uncertainty);
[rho] = cov2sdp(R,rho0);
rho = .5.*(rho+rho');
rho = rho./trace(rho);
res = sqrt(sum(abs(data-real(as.'*rho(:))).^2)/length(data));
rho0 = (rho0+rho0')./2;
rho0 = positive(rho0);
```

```
return
```

---

calc_initial.m

Calculates the initial state given system parameters described in `params` based on the initial Stern-Gerlach measurements and evolution before reconstruction begins.

```
function [state] = calc_initial(params)
%calculates the initial state for input state
%whose parameters are specified in params
load(params.params_filename);
if (params.sig_start == base_time)
   state = diag(pop_est(params.base_state,:));
   state = point_op(state,[0 1 0]);
   return
end
params.run_type = 5;
if isfield(params,'rho')
    params = rmfield(params,'rho');
end
RunD1new3;

state = reshape(as0(:,end),[7 7]);
state = (state+state')./2.0;
state = state./trace(state);
```

```
return
```

---

callibration.m

Performs calibrations as described in Sec. 5.2.2. Top of the file is a list of parameters that are determined from the experiment with comments before them to indicate their purpose.

```
%here is where you input the basic parameters
%in addition to these parameters you'll need to
%update initial_state_prep, and construct fnames,
%to point to the correct files
stokes_base = [];
params.stokes= stokes_base;
mag_shift = 1.0;
%Set close to experimental scattering rate for
%unit oscilator strength on 3-4' transition
% will subsequently be fit
base_scatter = 1.368;
offset = 0;
recon_length = 4.0;
%tweak to get scattering rate closer for a more
%robust fit
scale_factor = 1.01;
%Folder where experimental files are kept
```

```
folder_name = 'data/October 8 - final recon2/';
%subfolder for data
data_name = [folder_name 'raw data/'];
%subfolder for fields
wave_name = [folder_name 'waveforms/filtered originals/'];
%filename for conditional to be output
cond_name = [folder_name 'cond.mat'];
dist_name = [];
%filename for where to store parameters (output)
parameter_file = [folder_name 'params_fit.mat'];
params.params_filename = parameter_file;
mag_fact = [1 1];
%experimental filter band
filter_band = [.8 125];
%Stern-Gerlach results
pop_est(1,:) = [0, 0, 0, 0,0,.01,.98];
pop_est(2,:) = [0,.0078748,.0249074,.928515,.0286101,.0100929,0];
%Magnetic field magnitude in kHz
base_mag = 17;
%Detuning from 3-p' in GHz
det = 0.5450752;
snr = 1;
signal = 1;
%data points at start of run to ignore
bad_data = 7;
npoints = [];
%Larmor calibration files
params.mag_x_file = 'Larmorx-x.txt';
```

```
params.mag_y_file = 'Larmorx-y.txt';
params.data_filename = 'Larmorx - lin - start';
%recon calibration files
reconx='recon0p48-x.txt';
recony='recon0p48-y.txt';
recondata='recon0p48 - 128x1';
params.base_state = 1;
%time at which Stern-Gerlach is valid
base_time = .00274892;
params.sig_start = base_time;
recon_offset = 0;
params.run_type = 1;
%stop input of parameters
%do not change this block unless additional parameters are added
param_names = {'mag_shift','base_scatter','base_time',...
    'offset','recon_length','scale_factor','folder_name',...
    'data_name','wave_name','dist_name','recon_offset',...
    'filter_band','base_mag','pop_est','det',...
    'cond_name','snr','signal','bad_data','npoints'};
%stop block
save(parameter_file,param_names{:});
save('params.mat','params');
%computation for x magnetic field callibration
saves = param_names;
save(parameter_file,saves{:});
[mag_pos,offset] = fit_mag(-1);
mag_shift = mag_pos;
save(parameter_file,saves{:});
```

```
mag_fact = [1 1];
saves = param_names;
save(parameter_file,saves{:});
dist_name = [folder_name 'dist.mat'];
match_intensity(dist_name);
load(dist_name);
mean_light_cal = flucts*probs./sum(probs)
rms_light_cal = sqrt((flucts-mean_light_cal).^2*probs./sum(probs))
decay_time = 1./decay

saves = remove_names(param_names,'offset','npoints','mag_shift');
dir = 1;
save(parameter_file,saves{:});
[offset,mag_shift] = quad_offset(offset,mag_shift,500);
npoints = 500;
saves = remove_names(param_names,'mag_shift');
save(parameter_file,saves{:});
RunD1new3
figure(1);clf;plot([data,Zsmall]);
title('Offset fit');
ax = axis;
xlabel('blue = data,green = sim, check the offset and freq: ...
chnage initial guess offset and mag\_shift before line 96');

npoints = 500;
saves = remove_names(param_names,'mag_shift');
save(parameter_file,saves{:});
```

```
params.data_filename = 'Larmorx - circ - start';
params.sig_start = base_time;
params.run_type = 1;
params.stokes = stokes_base;
params.rho = [];
save params.mat params;
mag_shift = fit_mag2(1.0);
RunD1new3;
d = data;
g = gammas(:,2:3);
params.data_filename = 'Larmorz - circ - start';
params.mag_x_file = 'Larmorx-x.txt';
params.mag_y_file = 'Larmorx-y.txt';
params.zrun = 1;
save params params;
ox = offset;
saves = remove_names(param_names,'mag_shift','offset');
save(parameter_file,saves{:});
[mag_shift,offset] = fit_mag2(1.724,offset);
oz = offset;mz = mag_shift;
RunD1new3;
offset = ox;
params = rmfield(params,'zrun');
d = [d;data];
g =[g;gammas(:,2:3)];
a = find_measurement(d,g);
signal = max(d);
params.stokes = [0 -a(2) a(1)]
```

```
figure(2);clf;plot([d,g*a]);
title('Measurement Basis fit (x/z Larmor)');
xlabel('blue = data,green = sim, check agreement, ...
check meas basis (params.stokes),...
 change fit\_mag2 line 120 (offsets,mag\_shifts)');



%Reconstruction
params.run_type = 2;
params.mag_x_file = reconx;
params.mag_y_file = recony;
params.data_filename = recondata;
params.sig_start= base_time+0.00048;
saves = remove_names(param_names,'recon_offset','offset','npoints');
save(parameter_file,saves{:});
save('params.mat','params');
recon_offset = offset;
npoints = 1000;
saves = param_names;
params_base = params;
save(parameter_file,saves{:},'params_base');
params.rho = calc_initial(params);
RunD1new3;
snr = 30;
figure(3);
plot([Zsmall,data])
[rho] = bounded_est(data,as,snr,.01);
fid = fidelity(rho,rho0)
```

```
[ass,Bs] = setup_conditional(cond_name,[.986:.002:1.02],0,0);
```

---

create_generators_D1.m

This creates the generators for the evolution described in Chap. 4. It is based off the polarizability tensor which is calculated in `tensorD1full.m`.

`generator.measurement` contains the three basis measurements for future use.

`generators.hamiltonian` contains the hamiltonian part of the evolution.

`generators.super` is the nonhermitian part of the evolution including jumps due to spontaneous emission.

```
function [generators] = create_generators_D1(atom,lasers,repumper)

%for simplicity
excited_det = atom.deltadets;%GHz Measured from F=4
det = lasers.detuning;
pol = lasers.polarization;
g = atom.Gamma;
a2 = 1./(g./2 - i.*det);
a1 = 1./(g./2 - i.*det - i.*excited_det);
b1 = (a1+conj(a1))./2;
b2 = (a2 + conj(a2))./2;
b3 = g./(g - i.*excited_det).*(a1+conj(a2))./2;
```

```
%create the operators which jump to F=4
j4 = tensorD1full(atom.hyperfine);
j4p = j4;
j4(:,:,1,:,:) = -a1.*j4(:,:,1,:,:);
j4(:,:,2,:,:) = -a2.*j4(:,:,2,:,:);
j4 = squeeze(sum(j4,3));
generators.measurement = base_measurement(imag(j4));
generators.hamiltonian = sum(sum(j4.*fillin(conj(pol)...
,size(j4),3).*fillin(pol,size(j4),4),3),4);

j4 = j4p;
j4 = j4.*fillin(pol,size(j4),5);
j4 = sum(j4,5);
super = b1.*superop(j4(:,:,1,:));
super = super + superop(b3.*j4(:,:,1,:),j4(:,:,2,:));
super = super + b2.*superop(j4(:,:,2,:));

generators.super = super;
return
```

---

find_measurement.m

Performs a linear fit to measurement basis.

```
function [out] = find_measurement(data,states)
```

```
data  = data(:);
if size(states,1)==3
    states = states.';
end

out = states\data;
return
```

---

fitall.m

Uses `bounded_est.m` to estimate best fit state for all magnetic field scalings and offsets used in calculating `setup_conditional.m`. The state whose output signal matches the experimental data most closely is then chosen as the actual estimate ρ, with B being the fields that generated that state.

```
function [rho,B,rho0,res,traces,rhos,stats] = fitall(params,np);
if nargin<2
    np = [];
end
params = load_state_params(params);
a = load(params.params_filename);
bad_data = a.bad_data;
offset = a.recon_offset;
snr = a.snr;
upsample_factor = 1;
```

```
load(a.cond_name);

[data,sim_times] = input_data(params.data_filename...
,upsample_factor,params.sig_start.*1e3,-offset);
data = data((1+bad_data):end);

Hd = create_filter(Parameters.filter_name,Parameters.filter_order...
,Parameters.refilter_band,Parameters.N...
,Parameters.time);
data = filter(Hd,data);
l = min(length(data),size(ass,2));
if ~isempty(np)&l>np
    l = np;
end
if(size(ass,2) >l)
    ass= ass(:,1:l,:);
end
if length(data)>l
    data = data(1:l);
end
fast_search = 1;
if fast_search
    scales = Bs(2,1):Bs(2,2)-Bs(2,1):max(Bs(2,:));
    ls = length(scales);
    lr = size(Bs,2)/ls/ls;
    grid = zeros(ls,ls);
    grid(:) = [1:prod(size(grid))].';
    grid = grid.';
```

```
checked =[];



coarse_scale = 4;
coarse_grid = 1:coarse_scale:ls;

outer_res = inf;
outer_ind = 0;
for ii = [1:lr]

    best_x = 0;
    best_y = 0;
    minres = inf;
    for jj = coarse_grid
        for kk = coarse_grid
            [jj,kk]
            [rho,res] = bounded_est(data...
             ,ass(:,:,grid(jj,kk)),snr,.01);
            res
            checked = [checked grid(jj,kk)];
            if res<minres
                minres = res;
                best_x = jj;
                best_y = kk;
                best_rho = rho;
            end
        end
```

```
        end
        done = 0;
        while ~done
            old_x = best_x;
            old_y = best_y;
            for jj = [max([old_x-1 1]):1:min([old_x+1 ls])]
                for kk = [max([old_y-1 1]):1:min([old_y+1 ls])]
                    [jj,kk]
                    if all(grid(jj,kk)~=checked)
                        checked = [checked grid(jj,kk)];
                        [rho,res] = bounded_est(data...
                         ,ass(:,:,grid(jj,kk)),snr,.01);
                        res
                        if res<minres
                            minres = res;
                            best_x = jj;
                            best_y = kk;
                            best_rho = rho;
                        end
                    end
                end
            end
            if best_x==old_x & best_y == old_y
                done = 1;
            end
            if minres<outer_res
                outer_res = minres;
                best_field = grid(best_x,best_y);
```

```
                outer_rho = best_rho;
            end
        end
        grid = grid+ls.^2;
    end
    res = minres;
    rhos = 0;
    best_rho = outer_rho;

else
    minres = inf;
    best_field = 0;
    best_rho = 0;
    for ii = [1:size(Bs,2)]
        [rhos(:,:,ii),res(ii)] = bounded_est(data...
         ,ass(:,:,ii),snr,.01);
        if res(ii)<minres
            minres = res(ii);
            best_field = ii;
            best_rho = rhos(:,:,ii);
        end
    end
end
B = Bs(:,best_field);
params.B = B;
rho0 = calc_initial(params);
rho = best_rho;
if nargout>4
```

```
    traces = real([data(:),ass(:,:,best_field).'*rho(:)...
     ,ass(:,:,best_field).'*rho0(:)]);
    traces = [sim_times(end-length(data)+1:end).' traces];
end
if nargout>6
    stats.as = ass(:,:,best_field);
    stats.SNR = a.signal./rms_res(traces(:,2),traces(:,4));
    stats.fitSNR = a.signal./minres;
end
return
```

---

input_data.m

Inputs experimental data from a tab delimited file. Processes the timestamp on the data, to account for the estimated offset.

```
function [data,sample_times] = input_data(filename...
,upsample_factor,start_time,offset,max_time)
if nargin<3
    start_time = 0;
end
if nargin<4
    offset = 0;
end
if nargin<5
```

```
    max_time = [];
end
if ~iscell(filename)
    filename = {filename};
end
sample_times = [];
for ii = 1:length(filename)

fid = fopen(filename{ii});
if fid == -1
    error('invalid filename');
end
a = fgetl(fid);
M = fscanf(fid,'%f',inf);
fclose(fid);

d = 2;
l = length(M);
M = reshape(M,[d l./d]);
times = M(1,:).*1e3-start_time;%convert to miliseconds
times = times + mean(diff(times)).*offset;
out = M(2,:);
if isempty(max_time)
    mask = times>=0;
else
    mask = times>=0 & times<max_time;
end
times = times(mask);
```

```
%times = times-min(times);
out = out(mask);

base_step = mean(diff(times));
time_step = base_step./upsample_factor;
start_time = min(times);
end_time = max(times)+base_step-time_step;
times = start_time:time_step:end_time;
if upsample_factor ~= 1
out = resample(out.',upsample_factor,1);
end
if isempty(sample_times)
    sample_times = times;
    data = out.';
else
    data(ii,:) = out.';
end
end
if size(data,1)==1
    data = data.';
end
return
```

---

input_mag_fields.m

Inputs the experimentally generated magnetic fields, resampling them at the simulation rate.

```
function [out] = input_mag_fields(filename,start_time...
,timestep,stop_time)
fid = fopen(filename);
a = fgetl(fid);
M = fscanf(fid,'%f',inf);
fclose(fid);
%step = M(4)-M(1);
%start = find(abs(M - M(1) - step.*30)<1e-10);
%stop = find(abs(M - M(end-2)+ step.*30) <1e-10);
%M = M(start:stop-1);
l = length(M);
num_fields = 4;
M = reshape(M,[num_fields l./num_fields]);
out = M;
times = M(1,:);
step = times(2)-times(1);
out = M(2:end,:);

if nargin == 1
    out_times = times;
elseif nargin ==2
    if length(start_time)~=1
        out_times = start_time;
    else
        out_times = start_time:step:times(end);
```

```
    end
elseif nargin==3
    out_times = start_time:timestep:times(end);
else
    out_times = start_time:timestep:stop_time;
end
out_times = out_times(:).';
prev = sum(out_times<min(times));
post = sum(out_times>max(times));
out_times = out_times(prev+1:end-post);
out = spline(times,out,out_times).';
d = size(out,2);
out = cat(1,zeros(prev,d),out,zeros(post,d));

return
```

---

itermax.m

Performs a local minimization over all 50 field parameters to find the optimal set of angles.

```
function [field_params] = itermax(field_params)

N = size(field_params,1);
for ii = 1:N
```

```
    t = atan2(field_params(ii,2),field_params(ii,1));
    freq = sqrt(sum(field_params(ii,:).^2,2));
    [t,fval] = fminsearch('RunD1f',t...
     ,optimset('MaxIter',100),field_params,ii);
    display(fval);
    field_params(ii,:) = freq.*[cos(t) sin(t)];
    save best.mat field_params;
end

return
```

---

itermax2.m

Performs a coarse grained global optimization over all 50 angle variables sequentially. That is each variable is varied while the others are held constant. Makes use of `RunD1f.m` which is just a functional form of `RunD1new3` that outputs the entropy of the generated covariance matrix based on the measurement operator history.

```
function [field_params] = itermax(field_params,fluct)
if nargin<2
fluct = .05;
end
siz = 50; %number of iterations at each point
N = size(field_params,1);
for ii = 1:N
    t = atan2(field_params(ii,2),field_params(ii,1));
```

```
    freq = sqrt(sum(field_params(ii,:).^2,2));
    tmin = t;
    valmin = RunD1f(t,field_params,ii,fluct);
    for jj = 1:siz
        val = RunD1f(2.*pi.*jj./siz,field_params,ii,fluct);
        if val<valmin
            tmin = 2.*pi.*jj./siz;
            valmin=val;
        end
    end
    disp(['iteration ' num2str(ii) '=' num2str(valmin)]);
    field_params(ii,:) = freq.*[cos(tmin) sin(tmin)];
    if fluct>0
    save best2.mat field_params;
else
    save best3.mat field_params;
end
end

return
```

---

lattice_cov_D1.m

Main function called, which matches parameters from `RunD1new3.m` with generators from `create_generators_D1` and elsewhere. Then feeds the parameterized generators to `multistep3.m` to perform actual evolution.

```
function [as,magnetic_fields,Z,rho0,Zsmall,...
                gammas,as_full,measure] ...
                      = lattice_cov_D1(lasers,magnetic_fields...
                            ,repumper,run_params,initial_state)
Z = [];
%insert dummy initial state
d = 2.*run_params.F+1;
if nargin<5
    initial_state.rho = eye(d);
end

[lasers,magnetic_fields,initial_state,repumper,run_params,atom] ...
            = check_parameters(lasers,magnetic_fields...
              ,initial_state,repumper,run_params);


%use parameters for the D1 line
atom.Gamma = atom.GammaD1;
atom.deltadets = atom.deltadetD1;


[generators] = create_generators_D1(atom,lasers,repumper);


%calculate some needed parameters
s = 2./(lasers.scattering_time.*atom.Gamma);%normalized saturation
```

```
delta = lasers.detuning;
dt = run_params.dt;%timestep
fudge = (delta.^2 + atom.Gamma.^2./4); %to remove the
%dependence on the excited state level (inculded in generators)

%calculate the full evolution operators
%no jump includes the hamiltonian and decay terms
nojump = s./2.*dt.*fudge.*generators.hamiltonian;
if ~run_params.scatter
    nojump = i.*imag(nojump);
end
%test code, remove for actual run
%nojump = 1.*i.*imag(nojump)+real(nojump)

%add magnetic field detuning term
nojump_mag(:,:,1) = rot([1 0 0],dt,atom.hyperfine);
nojump_mag(:,:,2) = rot([0 1 0],dt,atom.hyperfine);
nojump_mag(:,:,3) = rot([0 0 1],dt,atom.hyperfine);



%jump includes the feeding terms only
jump = s.*fudge.*dt.*generators.super;%normalized
jump = jump.*run_params.scatter;%only include if scattering used
%now create the full Liouvillian superoperator
L_s = superop(nojump,eye(size(nojump))) + jump;%saturation dependent
for kk = 1:3
    magnetic_fields.L(:,:,kk) = superop(nojump_mag(:,:,kk)...
     ,eye(size(nojump)));%saturation independent
```

```
end
%create the superoperator which implements field fluctuations
fluct_ham = rot(magnetic_fields.orient,dt,atom.hyperfine);
L_fluct = superop(fluct_ham,eye(size(fluct_ham)));

%create space for answers

siz = size(generators.measurement);
if length(siz)<3
    measure = generators.measurement(:);
else
    measure = reshape(generators.measurement...
     ,[siz(1).*siz(2),siz(3)]);
end
%measure = i*rot([0 0 1],1,3);
measure = measure.';
if run_params.evolve_state==-1
    as = zeros([length(initial_state.rho(:)) run_params.N]);
elseif run_params.evolve_state ==0
    as = zeros([size(measure) run_params.N]);
else
    as = zeros([size(L_s)...
      floor(run_params.N./run_params.evolve_state)]);
end

gen_zero = L_fluct.*magnetic_fields.fluctuations(1) ...
        +L_s.*lasers.fluctuations(1);
%calculate evolution in rotating frame
```

```
lasers.scale_factor = sum(lasers.probabilities);
if ~run_params.scatter
    lasers.probabilities = lasers.scale_factor;
    lasers.fluctuations = 1;
    magnetic_fields.probabilities = 1;
    magnetic_fields.fluctuations = [0; 0 ;0];
end
%calculate evolution in rotating frame
for magnum = 1:length(magnetic_fields.probabilities)
for lasnum = 1:length(lasers.probabilities)
    %this is the full evolution superoperator
    gen_zero = sum(magnetic_fields.L...
     .*repmat(permute(magnetic_fields.fluctuations(:,magnum)...
,[3 2 1]),[d.^2 d.^2 1]),3) ...
        +L_s.*lasers.fluctuations(lasnum);

    %evolve using the exponentiated superoperator
    %and incoherently add all of the density matrices
    %for the different fluctuating alignments
    if run_params.evolve_state==0
    as = as + magnetic_fields.probabilities(magnum)...
     .*lasers.probabilities(lasnum)...
        .*multistep3(measure,gen_zero,magnetic_fields,run_params);
    elseif run_params.evolve_state == -1
        as = as + magnetic_fields.probabilities(magnum)...
         .*lasers.probabilities(lasnum)...
         .*multistep3(initial_state.rho(:)...
,gen_zero,magnetic_fields,run_params);
```

```
    else
        as = as + magnetic_fields.probabilities(magnum)...
         .*lasers.probabilities(lasnum)...
         .*multistep3(run_params.evolve_state...
,gen_zero,magnetic_fields,run_params);
    end
end
end

if run_params.evolve_state==0
    gammas = squeeze(real(sum(as...
     .*fillin(initial_state.rho(:),size(as),2),2)));
    for kk = 1:size(lasers.meas_pol,1)
        as_full(:,:,kk) = squeeze(sum(as...
         .*fillin(lasers.meas_pol(kk,:).',size(as),1),1));
    end
    l = size(gammas,2);
    for ii = 1:l
        Z(ii) = lasers.meas_stokes(1,:)...
         *cart_rotate(lasers.stokes,gammas(:,ii)...
,run_params.OD.*atom.Gamma...
.*2./3./lasers.scale_factor);
    end
    Z = Z.*lasers.scale_factor;
    gammas0 = real(measure*initial_state.rho(:));
    pad = lasers.meas_stokes(1,:)...
     *cart_rotate(lasers.stokes,gammas0...
,run_params.OD.*atom.Gamma.*2./3);
```

```
    Z = [repmat(pad,size(Z)) Z];
    Z = filter(run_params.filter,Z.');
    Z = Z(l+1:end);
    gammas = [repmat(gammas0,[1 l]) gammas];
    gammas = filter(run_params.filter,gammas.');
    %throw out padding and bad data
    gammas = gammas(l+1+run_params.bad_data:end,:);
    as_full = cat(2,repmat(permute(lasers.meas_pol*measure...
     ,[2 3 1]),[1 l 1]), as_full);
    as_full = permute(as_full,[2 1 3]);
    s0 = size(as_full);
    s1 = [s0(1) s0(2)*s0(3)];
    as_full = reshape(filter(run_params.filter...
     ,reshape(as_full,s1)),[s0]);
   %throw out prepadding and bad data
    as_full = permute(as_full(l+1+run_params.bad_data:end,:,:)...
     ,[2 1 3]);
    as = as_full(:,:,1);
else
    gammas = 0;
    as_full = 0;
end
R = 0; ahat = 0;
magnetic_fields.static = magnetic_fields.static./(2.*pi.*10^-6);
magnetic_fields.freq = magnetic_fields.freq./(2.*pi.*10^-6);
if run_params.evolve_state==0
    Zsmall = real(as'*initial_state.rho(:));
```

```
elseif run_params.evolve_state == -1
    Zsmall = real(measure(2,:)*conj(as));
    Zsmall = filter(run_params.filter,Zsmall);
else
    Zsmall = 0;
end

if isempty(Z)
    Z = Zsmall;
end
rho0 = point_op(initial_state.rho,lasers.orientation,[0 0 1]);
return
```

---

match_intensity.m

Performs the search over intensity distributions to best match observed intensity mean spread an skew as described in Sec. 5.2.2.

```
function [p,decay] = match_intensity(filename...
,intensities,base,restart)
%intensities sets the range of intensities over
% which to search, try to get the mean to zero
%before running this routine to avoid boundary issues
int0 = [1.2:-.025:.8];
set_base = 0;
```

```
restart = 0;
if nargin==1
    intensities = int0;
    set_base =1;
end
if nargin ==2
    if length(intensities) == 1
        restart = intensities;
        intensities = int0;
    else
        restart = 0;
    end
    set_base = 1;
end



%here we perform a run at each intensity and save the simulation
if restart==0
for ii = 1:length(intensities)
    falloff_factor = 1./intensities(ii);
    RunD1new3;
    if ii == 1
        Zs = Zsmall;
        gamma_set = gammas;
    else
        Zs(:,ii) = Zsmall(:);
        gamma_set(:,:,ii) = gammas;
    end
```

```
end
save intensity.mat;
else
    a =load('intensity.mat');
    gamma_set = a.gamma_set;
    Zs = a.Zs;
    intensities = a.intensities;
    data = a.data;
end
if set_base
    base = [1.05    0   max(data)...
     ./max(Zs(:,ceil(length(intensities)./2)))  .04 0];
end
%base tells the search routine where to stare
%base(1) is the mean
%base(2) is the assymetry
%base(3) is the scaling between data and sim
%base(4) is the width of the distribution
%base(5) is the decay

%performs the search
x = fminsearch('compare_int2',base,[],Zs,data(:),intensities);
%calculates the distribution and saves to filename,
%filename is the file that you will load in RunD1new3
%subsequently
p = tri_dist(x(1:4),intensities);
time_fac = length(sim_times)./(sim_times(end)-sim_times(bad_data));
decay = x(5).*time_fac;
```

```
if length(x)==6
    decay2 = x(6).*time_fac.^2;
else
    decay2 = 0;
end
probs = p(p>0);
flucts = intensities(p>0);
save(filename,'probs','flucts','decay','decay2');
return
```

---

multistep3.m

Performs evolution of the master equation in the superoperator picture. Output can be state or measurement as a function of time depending on `run_params`

```
function [out] = multistep3(measure,base_gen,mag,run_params)
%Applies the evolution matrix <op> <steps> times to the
% initial vector <start>, saving all of the intermediate
% results.

steps = run_params.N;

gens{1}=base_gen;
for ii=2:4
    gens{ii} = mag.L(:,:,ii-1);
```

```
end
weights = [ones(1,steps);mag.static.'];
if all(size(measure) == [1 1])
    measure_run = -1;
    d = size(base_gen,1);
    out = zeros([size(base_gen) floor(steps./measure)]);
elseif size(measure,2) > size(measure,1)
    measure_run = 1;
    d = size(measure,2);
    out = zeros([size(measure,1), size(measure,2),steps]);
else
    measure_run = 0;
    d = size(measure,1);
    out = zeros([size(measure,1), size(measure,2),steps]);
end
for ii = 1:steps
    gen = gens{1}+gens{2}*weights(2,ii)+gens{3}*weights(3,ii)...
        +gens{4}*weights(4,ii);
    if ii==1
        S = expm(gen.*run_params.pad_time);
    else
        S = expm(gen)*S;
    end
    if measure_run==-1
        if mod(ii,measure)==0
            out(:,:,ii./measure) = S;
        end
    elseif measure_run ==1
```

```
        out(:,:,ii) = measure*S;
    else
        out(:,:,ii) = (S*measure).';
    end
end
out = squeeze(out);
return
```

---

quad_offset.m

Fits offset and magnetic fields scalings simultaneously, used for calibration.

```
function [offset,mag_shift] = quad_offset(start,mag_start,npoints)
if nargin<2
    npoints = [];
end
while(1)
x = [start-1 start start+1];
y(1) = offset_test([x(1) mag_start],npoints);
y(2) = offset_test([x(2) mag_start],npoints);
y(3) = offset_test([x(3) mag_start],npoints);
pp = polyfit(x,y,2);
start = -pp(2)./2./pp(1);
if start>x(3)
   x = [x(3) x(3)+1 x(3)+2];
```

```
elseif start<x(1)
    x = [x(1)-2 x(1)-1 x(1)];
else
    break;
end
end
x
o = optimset('Display','iter');
[offset] = fminsearch('offset_test',[start mag_start],o,npoints);
mag_shift = offset(2);
offset = offset(1);
return
```

---

setup_conditional.m

Run once during calibration calculates a vector of measurement operator histories, with one for each possible field configuration. Used later by `fitall.m` to jointly estimate state and fields. Can include x and y scalings as well as an arbitrary fixed background field.

```
function [ass,Bs] = setup_conditional(filename,scale,bkgnd,bkgnd2)
if nargin<3
    bkgnd = 0;
end
if nargin<4
```

```
    bkgnd2 = bkgnd;
end
load params;
load(params.params_filename,'base_mag');
scale = scale(:).';
s1 = length(scale);
bkgnd = bkgnd(:).'.*base_mag;
s2 = length(bkgnd);
bkgnd2 = bkgnd2(:).'.*base_mag;
s3 = length(bkgnd2);

Bs(1,:) = kron(scale,ones(1,s1*s2*s2*s3));
Bs(2,:) = kron(ones(1,s1),kron(scale,ones(1,s2*s2*s3)));
Bs(3,:) = kron(ones(1,s1*s1),kron(bkgnd,ones(1,s2*s3)));
Bs(4,:) = kron(ones(1,s1*s1*s2),kron(bkgnd,ones(1,s3)));
Bs(5,:) = kron(ones(1,s1*s1*s2*s2),bkgnd2);
h = waitbar(0,'Computing...');
for jj = [1:size(Bs,2)]
    params.B = Bs(:,jj);
    RunD1new3;
    ass(:,:,jj) = as;
    waitbar(jj/size(Bs,2),h);
end
close(h);
save(filename,'ass','Parameters','Bs');
return
```

tensorD1full.m

```
function [alpha] = tensorD1full(F,pol,pol2)
%Creates a matrix of polarizability tensors.

d = 2*F+1;
alpha = zeros([d d 2 3 3]);
strength = [1/2 -sqrt(7/3)/2 -sqrt(3)/2 sqrt(5/3)/2 ];

for m1n = [1:d]
    m1 = m1n-F-1;
    for m2n = [1:d]
        m2 = m2n-F-1;
        for exn = 1:2
            ex = exn + 2;
            for q1n = 1:3
                q1 = q1n-2;
                for q2n = 1:3
                    q2 = q2n - 2;
                    alpha(m1n,m2n,exn,q1n,q2n) = ...
                        clebsch(F,1,ex,m2,q2,m2+q2)...
                        .*clebsch(F,1,ex,m1,q1,m1+q1)...
                        .*(m1+q1==m2+q2)...
                        .*strength(2*(F-3)+exn).^2;
```

```
                end
            end
        end
    end
end
if nargin>1
alpha = alpha.*fillin(pol,size(alpha),5);
alpha = sum(alpha,5);
if nargin>2
    alpha = alpha.*fillin(conj(pol2),size(alpha),4);
    alpha = sum(alpha,4);
end
end
return
```

---

tri_dist.m

Four parameter function that is used for the intensity distribution.

```
function [probs] = tri_dist(x,points)
mean_value = x(1);
assym = x(2);
scale = x(3);
width = x(4);
```

```
skip = mean(diff(points));
probs = zeros(size(points));
A = 1./width./(1-assym./2);
x0 = mean_value - width./2.*(1-assym./3)./(1-assym./2);
f = x(3).*A.*[1-assym - x0*assym./width , assym./width];
probs = sample(f,points,[x0+width,x0]);

return
```

---

unbound_est.m

Performs ordinary least squares fit to the data given measurement operator history.

```
function [R,rho0] = unbound_est(data,as,sigma,trace_uncertainty)
data = data(:);
if nargin<4
    trace_uncertainty = .01;
end
if nargin<3
    sigma = 1;
end
    if trace_uncertainty ==0
        tr_weight = 1e10;
    else
        tr_weight = 1./trace_uncertainty.^2;
```

```
    end
    tr = eye(7);
    R = as*as'./sigma.^2 + tr_weight.*tr(:)*tr(:)';
    ahat = inv(R)*as./sigma.^2;
    ahat = [ahat inv(R)*tr(:).*tr_weight];
    recon1 = ahat*[data; 1.0];

recon = reshape(recon1,[sqrt(length(recon1)),sqrt(length(recon1))]);
recon = (recon+recon')./2;
rho0 = recon;

a = sqrtm(rho0)*positive(recon)*sqrtm(rho0);
a = (a + a')./2;
fidelity = real(trace(sqrtm(a)));
return
```

Appendix C

Full tensor decomposition of the light shift

This appendix has been graciously provided by Prof. Ivan Deutsch. In this appendix we express the light-shift operator in terms of its irreducible tensor components. The potential, Eq. (4.36), is a contraction of two tensors, the atomic polarizability for the ground state manifold $\alpha_{ij} = -\sum_e d_i^{ge} d_j^{eg}$ and the field tensor $-E_i^* E_j/4$. We will restrict our attention to the alkali elements driven near the $S_{1/2} \rightarrow P_{J'}$ optical transition where $J' = 1/2, 3/2$ for the D1, D2 transitions respectively. The ground and excited state manifolds have resolvable hyperfine levels with total angular momentum quantum numbers F, F' . Expressing the laser field in terms of its complex amplitude and polarization, $\mathbf{E} = E_0 \epsilon$, and the atomic dipole operator in terms of its irreducible matrix element $d_i^{J'F'F} = \langle P_{J'} F' \| \, d \, \| S_{1/2} F \rangle \, D_i$, we write the light shift as in characteristic units,

$$V = \sum_{F'} V_{J'F'F} v_{FF'} \tag{C.1}$$

where $V_{J'F'F} = \left|\langle P_{J'}F' \| \, d \, \| S_{1/2}F\rangle\right|^2 E_0^2/4\hbar\Delta_{FF'}$ and

$$v_{F'F} = \sum_{ij} \Pi_{ij} A_{ij}, \quad \text{where } \Pi_{ij} = \epsilon_i^* \epsilon_j \text{ and } A_{ij} = D_i^\dagger D_j \tag{C.2}$$

is the dimensionless light shift operator. For future reference, the reduced matrix elements with fine-structure multiplet have relative strength,

$$\left|\langle P_{J'}F' \| \, d \, \| S_{1/2}F\rangle\right|^2 = f_{J'F'F} \left|\langle P \| \, d \, \| S\rangle\right|^2, \tag{C.3}$$

$$\text{where} f_{J'F'F} = (2J'+1)(2F+1) \left| \begin{Bmatrix} F' & I & J' \\ 1/2 & 1 & F \end{Bmatrix} \right|^2 \tag{C.4}$$

determine the branching ratios for spontaneous emission staring in J', F' and ending in $J = 1/2, F$ for nuclear spin I. The contraction can be written in terms of the irreducible spherical tensor components,

$$v_{F'F} = \sum_{K=0}^{2} \sum_{Q=-K}^{K} (-1)^Q \Pi_{-Q}^{(K)} A_Q^{(K)}. \tag{C.5}$$

The tensors Π_{ij} and A_{ij} are each reducible outer products of two vectors. For a generic tensor $T_{ij} = U_i V_j$,

$$T_Q^{(K)} = \sum_q \langle KQ|1 \; Q-q, 1 \; q\rangle \, U_{Q-q} V_q. \tag{C.6}$$

The scalar and vector components of the field polarization tensor then have simple form,

$$\Pi_0^{(0)} = -\frac{1}{\sqrt{3}} \left|\epsilon\right|^2, \Pi_q^{(1)} = \frac{i}{\sqrt{2}} \left(\epsilon^* \times \epsilon\right) \tag{C.7}$$

The rank-2 irreducible components are more complicated. For example,

$$\Pi_0^{(2)} = \frac{1}{\sqrt{6}} \left[3\left|\epsilon_z\right|^2 - \left|\epsilon\right|^2\right], \tag{C.8}$$

as related to the familiar second order Legendre polynomial. The atomic polarizability operator acts solely on the ground state defined by angular momentum F. As

such the irreducible spherical components are proportional to the solid harmonics. Defining

$$\mathcal{Y}_Q^{(K)}(x,y,z) = (-1)^Q \sqrt{\frac{(K-Q)!}{(K+Q)!}} r^K P_K^Q(\cos\theta) e^{iK\phi}, \tag{C.9}$$

where (r,θ,ϕ) are the spherical coordinates associated with (x,y,z),

$$\mathcal{Y}_0^{(0)}(x,y,z) = 1, \mathcal{Y}_q^{(1)}(x,y,z) = x_q, \tag{C.10a}$$

$$\mathcal{Y}_0^{(2)}(x,y,z) = \frac{3}{2}\left(z^2 - \frac{1}{3}r^2\right), \tag{C.10b}$$

$$\mathcal{Y}_{\pm1}^{(2)}(x,y,z) = \sqrt{3} x_{\pm1} z, \tag{C.10c}$$

$$\mathcal{Y}_{\pm2}^{(2)}(x,y,z) = \sqrt{\frac{3}{2}} x_{\pm2}^2 \tag{C.10d}$$

we have,

$$A_Q^{(K)} = a_K \mathcal{Y}_Q^{(K)}(F_x, F_y, F_z) \tag{C.11}$$

The coefficients a_K follow from the Wigner-Ekert theorem as shown below. Combining Eq. (C.2) and Eq. (C.7) and Eq. (C.8), the dimensionless light-shift operator is

$$v = a^{(0)} \frac{-|\epsilon_L|^2}{\sqrt{3}} + a^{(1)} \frac{i}{\sqrt{2}} (\epsilon_L^* \times \epsilon_L) \cdot \mathbf{F} + a^{(2)} \frac{1}{\sqrt{6}} \left(3 |\epsilon_L \cdot \mathbf{F}|^2 - \mathbf{F}^2 |\epsilon_L|^2\right) \tag{C.12}$$

According to the Wigner-Ekert theorem,

$$a^{(K)} = \frac{\langle F \| A^{(K)} \| F \rangle}{\langle F \| \mathcal{Y}^{(K)}(\mathbf{F}) \| F \rangle}. \tag{C.13}$$

The reduced matrix element associated with the atomic polarizability is related to that of the dipole operators through the $6J$ symbol,

$$\langle F \| A^{(K)} \| F \rangle = \langle F \| \left(D^\dagger D\right)^{(K)} \| F \rangle \tag{C.14}$$

$$= (-1)^{K+2F} \sqrt{(2F'+1)(2K+1)} \begin{Bmatrix} F & 1 & F' \\ 1 & F & K \end{Bmatrix} \times \tag{C.15}$$

$$\langle F \| D^\dagger \| F' \rangle \langle F' \| D \| F \rangle . \tag{C.16}$$

By definition, $\langle F' \| D \| F \rangle = 1$, and taking the Conden-Shortley convention

$$\langle F \| D^\dagger \| F' \rangle = (-1)^{F-F'} \sqrt{\frac{2F'+1}{2F+1}} \langle F' \| D \| F \rangle . \tag{C.17}$$

To determine the reduced matrix element associated with the solid harmonic,

$$\langle F, F | \mathcal{Y}_0^{(K)}(F_x, F_y, F_z) | F, F \rangle = \langle F, F | J^K P_K \left(F_z F^{-1} \right) | F, F \rangle \tag{C.18}$$

$$= [F(F+1)]^{K/2} P_K \left(\sqrt{F/(F+1)} \right) \tag{C.19}$$

$$= \langle F \| \mathcal{Y}^{(K)}(\mathbf{F}) \| F \rangle \langle F, F | K, 0, F, F \rangle . \tag{C.20}$$

Combining Eq. (C.13) and Eq. (C.20), the coefficients

$$a_{F'F}^{(K)} = (-1)^{K+3^-F'} \sqrt{\frac{(2K+1)(2F'+1)^2}{(2F+1)(F(F+1))^K}} \begin{Bmatrix} F & 1 & F' \\ 1 & F & K \end{Bmatrix} \frac{\langle F, F | K,), F, F \rangle}{P_K \left(\sqrt{F/(F+1}} \right), \tag{C.21}$$

leading to a final, basis independent, form of the light shift,

$$V(S_{1/2}, F \to P_{J'}, F') = V_{F'F} \left[C_{J'F'F}^{(0)} |\epsilon_L|^2 + C_{J'F'F}^{(1)} \left(\frac{\epsilon_L^* \times \epsilon_L}{i} \right) \cdot \mathbf{F} \right.$$
$$\left. + C_{J'F'F}^{(2)} \left(|\epsilon_L \cdot \mathbf{F}|^2 - \frac{1}{3} \mathbf{F}^2 |\epsilon_L|^2 \right) \right] , \tag{C.22}$$

where,

$$C_{J'F'F}^{(0)} = -\frac{1}{\sqrt{3}} a_{F'F}^{(0)} f_{J'F'F}, \tag{C.23a}$$

$$C_{J'F'F}^{(1)} = -\frac{1}{\sqrt{2}} a_{F'F}^{(1)} f_{J'F'F}, \tag{C.23b}$$

$$C_{J'F'F}^{(2)} = \sqrt{\frac{3}{2}} a_{F'F}^{(2)} f_{J'F'F}, \tag{C.23c}$$

and

$$V_{F'F} = \frac{|\langle P \| d \| S \rangle|^2 E_0^2}{4\hbar\Delta_{F'F}} = \left(\frac{\hbar\Gamma^2}{8\Delta_{F'F}} \right) \frac{I}{I_{\text{sat}}} \tag{C.24}$$

is the light shift associated with a unit oscillator strength with saturation intensity I_{sat} and detuning $\Delta_{F'F}$ from a hyperfine resonance.

References

[1]

[2] Ph.D. thesis.

[3] These figures are used with the gracious permission of Greg Smith.

[4] C. Ahn, A. C. Doherty, and A. J. Landahl, Phys. Rev. A **65** (2002), 042301.

[5] S. E. Ahnert and M. C. Payne, Phys. Rev. A **71** (2005), 012330.

[6] D. Bacon, A. M. Childs, and W. van Dam, (2005).

[7] V. Belavkin, Rep. Math. Phys. **43** (1999), 405.

[8] P. Berman (ed.), *Cavity quantum electrodynamics*, Academic Press, San Diego, 1994.

[9] T. Bhattacharya, S. Habib, and K. Jacobs, Phys. Rev. Lett. **85** (2000), 4852.

[10] J. D. Bjorken and S. D. Drell, *Relativistic quantum fields*, McGraw-Hill, New York, 1965.

[11] L. Bouten, R. von Handel, and M. James, (2006).

[12] T. A. Brun, Am. J. Phys. **59** (1991), 834.

[13] H. J. Carmichael, *An open systems approach to quantum optics*, Springer-Verlag, Berline, 1993.

[14] C. M. Caves, J. Supercond. **12** (1999), 707.

[15] K. W. Chan, C. K. Law, and J. H. Eberly, Phys. Rev. Lett. **88** (2002), 100402.

[16] I. L. Chuang, N. Gershenfeld, , and M. Kubinec, Phys. Rev. Lett. **80** (1998), 3408.

[17] J. Dalibard and C. Cohen-Tannoudji, J. O. S. A. B **2** (1985), 1707.

[18] R. Derka, V. Buzek, and A. K. Ekert, Phys. Rev. Lett. **80** (1998), 1571.

[19] I. H. Deutsch, Am. J. Phys. **59** (1991), 834.

[20] I. H. Deutsch and J. C. Garrison, Phys. Rev. A **43** (1991), 2498.

[21] I. H. Deutsch and P. S. Jessen, Phys. Rev. A **57** (1998), 1972.

[22] M. H. Devoret and R. J. Schoelkopf, Nature **406** (2000), 1039.

[23] A. C. Doherty and K. Jacobs, Phys. Rev. A **60** (1999), 2700.

[24] J. P. Dowling, G. S. Agarwal, and W. P. Schleich, Phys. Rev. A **49** (1994), 4101.

[25] T. J. Dunn, I. A. Walmsley, and S. Mukamel, Phys. Rev. Lett. **74** (1995), 884.

[26] D. T. Smithey *et al.*, Phys. Rev. Lett. **70** (1993), 1244.

[27] C. W. Gardiner and M. J. Collett, Phys. Rev. A **31** (1985), 3761.

[28] C. W. Gardiner and P. Zoller, *Quantum noise*, second edition ed., Springer-Verlag,, Berlin, 2000.

[29] J. Gea-Banacloche, Phys. Rev. Lett. **89** (2002), 217901.

[30] J. Gea-Banacloche, Phys. Rev. A **68** (2003), 046303.

[31] JM Geremia.

[32] JM Geremia.

[33] JM Geremia, J. K. Stockton, and H. Mabuchi, Science **304** (2004), 270.

[34] JM Geremia, J. K. Stockton, and H. Mabuchi, Phys. Rev. Lett. **94** (2005), 203002.

[35] W. Happer and B. S. Mathur, Phys. Rev. **163** (1967), 12.

[36] M. Horodecki, P. Horodecki, and R. Horodecki, Phys. Lett. A **223** (1996), 1.

[37] W. M. Itano, Phys. Rev. A **68** (2003), 046301.

[38] B. Julsgaard, A. Kozhekin, and E. Polzik, Nature **413** (2001), 400.

[39] H. J. Kimble, Physica Scripta. **176** (1998), 127.

[40] D. E. Kirk, *Optimal control theory: An introduction*, Dover Publications, Inc., Mineola, N.Y., 2004.

[41] G. Klose, G. Smith, and P. S. Jessen, Phys. Rev. Lett. **86** (2001), 4721.

[42] C. Kurtsiefer, T. Pfau, and J. Mlynek, Nature **386** (1997), 150.

[43] A. Kuzmich, N. P. Bigelow, and L. Mandel, Europhys. Lett. **42** (1998), 481.

[44] A. Kuzmich, L. Mandel, and N. P. Bigelow, Phys. Rev. Lett. **85** (2000), 1594.

[45] H. Mabuchi, J. Ye, and H. J. Kimble, Appl. Phys. B. **68** (1999), 1095.

[46] Y. Makhlin, G. Schön, and A. Shnirman, Rev. Mod. Phys. **73** (2001), 357.

[47] G. J. Milburn, K. Jacobs, and D. F. Walls, Phys. Rev. A **50** (1994), 5256.

[48] P. A. Miller and S. Sarkar, Phys. Rev. E **60** (1999), 1542.

[49] K. Mølmer and L. B. Madsen, Phys. Rev. A **70** (2004), 052102.

[50] N. V. Morrow, S. K. Dutta, and G. Raithel, Phys. Rev. Lett. **88** (2002), 093003.

[51] M. A. Nielsen and I. L. Chuang, *Quantum computation and quantum information*, Cambridge University Press, Cambridge, 2000.

[52] T. J. Osborne, Phys. Rev. A **72** (2005), 022309.

[53] K. Osbourne and J. Martinis, (2004).

[54] W. Pauli, *Handbuch der physik*, vol. 24(1), Springer, Berline, 1933.

[55] A. Peres, Phys. Rev. Lett. **77** (1996), 1413.

[56] J. Preskill, *Lecture notes for physics 219: Quantum information and computation*, Available from http://www.theory.caltech.edu/people/preskill/ph219, 2001.

[57] H. Rabitz, Science **299** (2003), 525, (see also references within).

[58] P. Rungta and C. M. Caves, Phys. Rev. A **67** (2003), 012307.

[59] V. I. Rupasov and V. I. Yudson, Sov. Phys. JETP **60** (1984), 927.

[60] R. Ruskov, K. Schwab, and A. N. Korotkov, IEEE Trans. Nanotech. **4** (2005), 132.

[61] J. J. Sakurai, *Modern quantum mechanics*, Addison-Wesley, Reading, MA, 1994.

[62] M. O. Scully and M. S. Zubairy, *Quantum optics*, Cambridge Press, Cambridge, 1997.

[63] G. A. Smith, S. Chaudhury, and P. S. Jessen, J. Opt. B **5** (2003), 323.

[64] Y. Takahashi, Phys. Rev. A **60** (1999), 4947.

[65] A. G. White *et al.*, Phys. Rev. Lett. **83** (1999), 3103.

[66] A. Hopkins *et al.*, Phys. Rev. B **68** (2003), 235328.

[67] C. H. Bennett *et al.*, Journal of Cryptology **5** (1992), 3.

[68] D. Budker *et al.*, Rev. Mod. Phys. **74** (2002), 1153.

[69] D. J. Wineland *et al.*, Fort. Phys. **46** (1998), 363.

[70] D. Leibfried *et al.*, Phys. Rev. Lett. **77** (1996), 4281.

[71] D. Leibfried *et al.*, J. Phys. B **36** (2003), 599–612.

[72] G. A. Smith *et al.*, Phys. Rev. Lett. **93** (2004), 163602.

[73] G. T. Foster *et al.*, Phys. Rev. Lett. **85** (2000), 3149.

[74] J. E. Reiner *et al.*, J. Opt. Sci. Am. B. **18** (2001), 1911.

[75] J. K. Stockton *et al.*, Phys. Rev. A **69** (2004), 032109.

[76] JM Geremia *et al.*, Phys. Rev. Lett. **91** (2003), 250801.

[77] L. P. Kouwenhoven *et al.*, *Mesoscopic electron transport*, vol. 345, Kluwer Academic, Dordecht, 1997.

[78] P. Rungta *et al.*, Phys. Rev. A **64** (2001), 042315.

[79] S. Chaudhury *et al.*

[80] W. M. Itano *et al.*, Phys. Rev. A **47** (1993), 3554.

[81] L. K. Thomsen and H. M.Wiseman, Phys. Rev. A **65** (2002), 063607.

[82] U. M. Titulaer and R. J. Glauber, Phys. Rev. **140** (1965), B676.

[83] U. M. Titulaer and R. J. Glauber, Phys. Rev. **145** (1966), 1041.

[84] A. Uhlmann, Open Sys. Information. Dyn. **5** (1998), 209.

[85] S. J. van Enk and C. A. Fuchs, Quant. Inf. and Comp. **2** (2002), 151.

[86] S. J. van Enk and H. J. Kimble, Quant. Inf. and Comp. **2** (2001), 1.

[87] S. J. van Enk and H. J. Kimble, Phys. Rev. Lett. **63** (2001), 023809.

[88] L. Vandenberghe and S. Boyd, SIAM Review **38** (1996), 49.

[89] S. J. vanEnk and H. J. Kimble, Phys. Rev. A **68** (2003), 046302.

[90] K. G. H. Vollbrecht and R. F. Werner, Phys. Rev. A **64** (2001), 062307.

[91] J. von Neumann, *Mathematical foundation of quantum mechanics*, Princeton University Press, Princeton, N.J., 1955.

[92] *et al.* W. P. Smith, Phys. Rev. Lett. **89** (2002), 133601.

[93] H. M. Wiseman, Phys. Rev. A **49** (1994), 2133.

[94] W. K. Wooters, Phys. Rev. Lett. **80** (1998), 2245.